Spring 2017

AIRBORNE LIDAR BATHYMETRY BEAM DIAGNOSTICS USING AN UNDERWATER OPTICAL DETECTOR ARRAY

Matthew Birkebak
University of New Hampshire, Durham

AIRBORNE LIDAR BATHYMETRY BEAM DIAGNOSTICS USING AN UNDERWATER OPTICAL DETECTOR ARRAY

BY

MATTHEW BIRKEBAK

BSME, University of New Hampshire, 2015

THESIS

Submitted to the University of New Hampshire
in Partial Fulfillment of
the Requirements for the Degree of

Master of Science
in
Ocean Engineering: Ocean Mapping

May, 2017

This thesis has been examined and approved in partial fulfillment of the requirements for the degree of Masters of Science in Ocean Engineering: Ocean Mapping by:

Thesis Director, Dr. Shachak Pe'eri, Research Associate Professor, Center for Coastal and Ocean Mapping

Dr. Firat Eren, Research Scientist, Center for Coastal and Ocean Mapping

Dr. Neil Weston, Technical Director, National Oceanic and Atmospheric Administration, Office of Coast Survey

On April 6th, 2017

Original approval signatures are on file with the University of New Hampshire Graduate School.

ACKNOWLEDGEMENTS

This work was possible through the help of many of my advisors and mentors. I would like to thank professors Shachak Pe'eri, Firat Eren and Neil Weston who dedicated time and effort into this project. Also very special thanks to Paul Lavoie for his enormous help in the construction of the detector array and waterproof housings. I would also like to thank Dr. Yuri Rzhanov for his help with the image processing, Carlo Lanzoni for his help producing the detector array circuitry and Sean Kelley for his work on the data collection and analysis.

Finally I thank the National Oceanic and Atmospheric Administration for their support and funding that made this research possible.

Joint Hydrographic Center / Center for Coastal and Ocean Mapping (NOAA Ref. No: NA15NOS4000200)

TABLE OF CONTENTS

LIST OF FIGURES

LIST OF TABLES

ABSTRACT

AIRBORNE LIDAR BATHYMETRY BEAM DIAGNOSTICS USING AN UNDERWATER OPTICAL DETECTOR ARRAY

by

Matthew Birkebak

University of New Hampshire, May, 2017

The surface geometry of air-water interface is considered as an important factor affecting the performance of Airborne Lidar Bathymetry (ALB), and laser optical communication through the water surface. ALB is a remote sensing technique that utilizes a pulsed green (532 nm) laser mounted to an airborne platform in order to measure water depth. The water surface (i.e., air-water interface) can distort the light beam's ray-path geometry and add uncertainty to range calculation measurements. Previous studies on light refracting through a complex water surface are heavily dependent on theoretical models and simulations. In addition, only very limited work has been conducted to validate these theoretical models using experiments under well-controlled laboratory conditions.

The goal of the study is to establish a clear relationship between water-surface conditions and the uncertainty of ALB measurement. This relationship will be determined by conducting more extensive empirical measurements to characterize the changes in beam slant path associated with a variety of short wavelength wind ripples, typically seen in ALB survey conditions. This study

will focus on the effects of capillary and gravity-capillary waves with surface wavelengths smaller than the diameter of the laser beam on the water surface. Simulations using Monte-Carlo techniques of the ALB beam footprints and the environmental conditions were used to analyze the ray-path geometries. Based on the simulation results, laboratory experiments were then designed to test key parameters that have the greatest contribution on beam path and direction through the water. The laser beam dispersion experiments were conducted in well-controlled laboratory setting at the University of New Hampshire's Wave and Tow tank.

The spatial elevations of the water surface were independently measured using a high resolution wave staff. The refracted laser beam footprint was measured using an underwater optical detector consisting of a 6x6 array of photodiodes. Image processing techniques were used to estimate the laser's incidence angle intercepted by the detector array. Beam patterns that resulted from intersection between the laser beam light field underwater and the detector array were modeled and used to calculate changes in position and orientation for water surface conditions containing wavelengths less than 0.1m. Finally, a total horizontal uncertainty (THU) model was estimated, which can be implemented in total propagated uncertainty (TPU) models for reporting as a measure of the quality of each measurement. The wave refraction error for various sea states and beam characteristics was successfully quantified using both experimental and analytical techniques.

1. INTRODUCTION

Airborne Lidar Bathymetry (ALB) is a coastal survey system that measures water depth using a pulsed scanning laser mounted to an airborne platform. Common ALB laser pulses are transmitted at a green wavelength that is generated by frequency doubling of the fundamental wavelength Nd:YAG laser from 1064 nm to 532 nm (Guenther et al., 1994; Penny, et al., 1986). The choice of a green wavelength is because of the ocean's optical characteristics, in which the minimum spectral absorption for most waters is at green wavelengths (Jerlov, 1968). The interactions of the laser pulse with the environment is typically logged over time as a waveform (Figure 1.1). Water depth is calculated using the Time of Flight (TOF) between the laser pulse interactions with the water surface (surface return) and seafloor (bottom return). In order to calculate the position of the laser beam on the seafloor for depth and position reporting, it is important that the refracted beam path of the laser is known including aircraft attitude and motion corrections (Guenther, 1985).

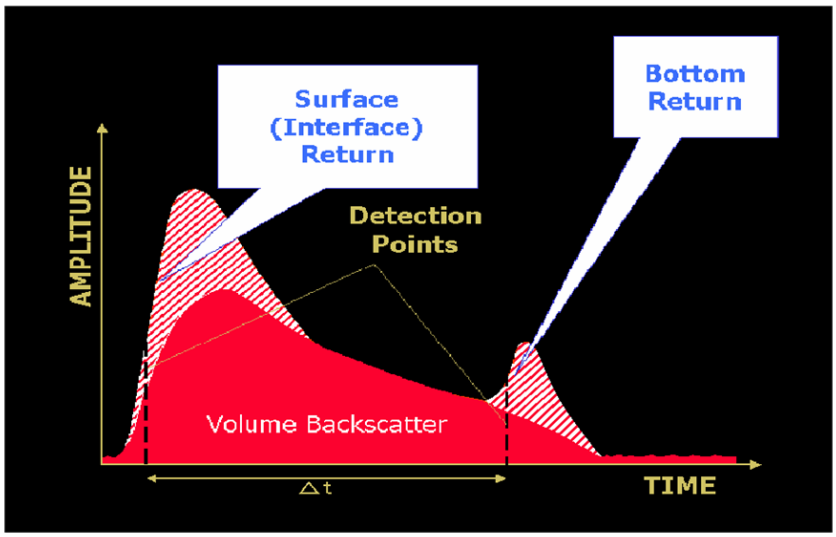

Figure 1.1: Example ALB waveform consists of three parts: the surface reflection, volume backscatter, and the bottom reflection. Image from Guenther (2007).

Standard operating conditions for commercial ALB data collection are typically at altitudes ranging from 300 to 600 m above the water surface. Although various ALB systems may vary in hardware specifications (Table 1.1), the ray-path geometry of the laser beam in all systems is the same. The ALB's ray-path geometry includes a transmission of a laser beam with a typical solid angle of 5 to 45 mrad. The laser beam propagates through the atmosphere then interacts with the water surface. A small part of the laser energy is scattered at the water surface and reflects back to ALB detector, while most of the laser energy propagates down the water column. Within the water column, the laser beam may interact with suspended and dissolved material (i.e., additional scattering) until it intersects with the bottom. The reflection pattern of the laser beam back up the water column will depend on seafloor characteristics including slope and roughness. It is assumed that the returning ray-path of the laser beam is near identical to the transmit path following Green's reciprocity principle (Guenther, 1985). The returning laser energy is collected by a photodetector (avalanche photodiode or a photomultiplier tube) to generate the waveform.

	Fugro LADS MK3	Optech CZMIL	AHAB HawkEye III	AHAB Chiroptera II	Reigl VQ-820-G	Reigl VQ-880-G	USGS EAARL-B
Origin	Australia	Canada	Sweden	Sweden	Austria	Austria	USA
Release Year	2011	2011	2013	2013	2011	2015	2012
Scan Shape	Rectilinear	Circular	Elliptical	Elliptical	Elliptical Arc	Elliptical	Elliptical Arc
Scan direction and angle from nadir	Fwd up to 8°	Fwd to 20°	Fwd and aft 14°, sideways 20°	Fwd and aft 14°, sideways 20°	Fwd and aft 20°	Fwd and aft 20°	Fwd and aft 20°
Scan Method	Oscillating Mirror	Palmer Scanner	Oblique Scanner	Oblique Scanner	Rotating Mirror	Palmer Scanner	Oscillating Mirror
Typical Depth (Secchi)	2.5-3	2.5	1.5-3	1.5	1	1.5	1.5-2.5
Beam Divergence (mrad)	7.5	6	7.5	3.7	1.5	1.2	0.6

Table 1.1: ALB system specifications according to manufacturers (Quadros N. , 2013).

The amplitude and shape of the surface return in the ALB waveform is combination of reflection of the laser from the water surface superimposed on volume backscatter from the top layers of the water column (Figure 1.1). In this study, I assume that the amplitude and shape of the surface return depends on surface wave conditions and the angle of incidence of the ALB beam. The amplitude of the volume backscatter depends on scattering, absorption and other Inherent Optical Parameters (IOP's) of the water column. The rest of the transmitted laser energy will continue down to the bottom with an exponential decay as a function of depth. The representation of the volume backscatter in the ALB waveform also depends on the receiver's field-of-view (Feygels et al., 2003) and the amplification used by the photodetector (i.e., linear or logarithmic). It is also assumed that the shape and amplitude of the bottom return depends on a large range of environmental factors that include the seafloor reflectance, seafloor slope, and deformation of the beam footprint due to surface waves (Wang & Philpot, 2007). A variety of algorithms are currently used in commercial ALB software to estimate water depth using the TOF approach (i.e., the time separation between the surface and seafloor returns) that include: a peak distance, a full-width half max distance (i.e., 3dB method) and Gaussian deconvolution (Guenther, 1985; Collin et al., 2011). However, the water surface, water column and bottom environmental factors affect the ALB waveform and are a source of error in the TOF calculations.

As mentioned above, the water surface geometry is one of the primary sources of uncertainty in an ALB system (Guenther, 1985). The geometry of the water surface is mainly derived by wind conditions and includes capillary waves (i.e., waves that dissipated by surface tension and their wavelengths is less than 0.017m) and gravity waves (i.e., larger swells that are dissipated by gravity) (Dean & Dalrymple, 1984). ALB surveys are typically conducted in Beaufort Sea State conditions lower than the value 3 (wind speed less than 5 m/s (10 knots)) to avoid the presence

of white capping, and higher turbidity in the water column. ALB systems perform best in light breezes, where small capillary waves produce sufficient laser light backscatter for surface detection. ALB surveys that are conducted with no wind (i.e., smooth glassy water surface), may not detect the water surface due to off nadir specular reflections.

It is difficult to model the water surface that an ALB beam interacts with, especially near the shoreline where the waves break (Mobley, 1994). ALB systems treat the water surface as a smooth level plane (still water assumption) or filter the water surface returns to approximate a smooth surface in order to simplify ray path calculations. However, the water surface is a spatially and temporally dynamic boundary consisting of surface waves. The wind-generated water surface geometry during an ALB survey will non-uniformly refract and reflect the laser energy and will introduce horizontal and vertical uncertainty in bathymetric measurements by altering the slant path of be beam below the water surface (i.e. wave refraction error). The ability to quantify refraction uncertainties due to surface waves would aid in accurate reporting using supplemental total propagated uncertainty (TPU) calculations with the bathymetry measurements (IHO, 2008).

Although research on the dependence of the expected wave periods and heights due to wind parameters (such as speed, duration, and fetch) has been investigated for more than half a century (e.g., Cox and Munk, 1954; Mobley, 2004), only a few studies investigated the contribution of a given sea state on the ALB measurements (e.g., Tulldahl and Steinvall, 2004; Karlsson, 2011). A wind-driven water surface contains slopes that alter the laser beam's incidence angle on the water surface, which changes the refracted and reflected ray-path geometries from that of an ideal flat water surface. In some cases, the true surface return is not reflected back towards the ALB receiver and the system may misinterpret volume backscatter as

the surface return, thus miscalculate the water depth (Guenther 1985*)*. In other cases, the laser beam may be refracted in an direction not predicted by the system due to wave slopes and will follow a different slant path to the bottom inducing error in the depth and position calculation.

Steinvall et al. (1994) suggested that the associated waves at wind speeds 10-12 m/s will cause a horizontal error is around 5-10% of the depth while the vertical error may be 1-2% of the depth. A similar conclusion was suggested by Wang and Philpot (2007) that studied the ability of an ALB system to perform bottom reflectivity classifications using a SHOALS-1000 ALB dataset collected over Egmont Key, Florida. They observed that the bottom return signal after radiometric correction had an increased variance and magnitude because of the surface wave conditions and the contribution from other environmental factors (such as, water clarity or bottom slope) was secondary. Their findings indicated that ALB performance could be predicted from environmental conditions, such as water surface geometry and water-column properties.

Tulldahl and Steinvall (2004) conducted Monte Carlo simulations in order to evaluate the possibility to detect a $1m^3$ target using ALB over a range of depths and wind speeds in order to evaluate the contribution from the water column and the surface geometry, respectively. Using a two-step gridded method that simulated water surface (i.e., gravity and capillary waves), it was found that the probability of detection of the target was reduced as depth or wind speed was increased. Karlsson (2011) utilized computer simulation and individual ray tracing to estimate the effects of capillary and gravity surface waves on the ray-path geometry of the laser beam footprint. The intention of the models was to predict the variation in the refracted angle of the beam. The simulation results indicate a horizontal uncertainty of ALB systems is linked to wind speeds over the water surface and the projected laser beam diameter at the water surface. Higher wind speeds produce greater uncertainty in horizontal component of the measurement. Karlsson

(2011) also observed that larger ALB beam diameters on the water surface had lower variability and standard deviation than small diameter beams when subjected to the same sea state. It is important to note that Karlsson (2011) conducted empirical experiments using only a single sea-state condition and one beam diameter (i.e., the laser beam was only intersected at only one location). In order to confirm the Tulldahl and Steinvall (2004) and Karlsson (2011) computer models, comprehensive empirical results over multiple survey conditions (i.e. different sea states) are needed to properly analyze the laser beam ray-path geometry passing from air to water (down-welling) as well as from water to air (upwelling).

The goal of the study is to establish a clear relationship between water-surface conditions and the uncertainty of ALB refraction angle. This relationship will be determined by conducting more extensive empirical measurements to characterize the changes in beam slant path associated with a variety of short wavelength wind ripples, typically seen in ALB survey conditions. This study will focus on the effects of capillary and gravity-capillary waves with surface wavelengths smaller than the diameter of the laser beam on the water surface. These types of waves are caused by wind speeds below 5 m/s (as low as 1-2 m/s) and will start to develop with fetches less than 1 m (Zhang, 1995). The experiments of the wave refraction error were conducted in well-controlled laboratory setting at the University of New Hampshire's Wave and Tow tank. The spatial elevations of the water surface were independently measured using a high resolution wave staff. The refracted laser beam footprint was measured using an underwater optical detector array. Image processing techniques were used to estimate the laser's incidence angle intercepted by the detector array.

Computer ray-trace simulations using Monte-Carlo techniques were used to identify key hardware and environmental parameters that will be further investigated in empirical

experiments. The key hardware and environmental parameters used to simulate ALB beams and statistically analyze the ray-path results include: fetch, wind speed, laser beam incidence angle, and beam footprint diameter. The main objectives for conducting empirical experiments in well-controlled laboratory settings were to evaluate and quantify the contribution of each key parameter to the ALB ray-path geometry estimate the wave refraction error. Finally, a total horizontal uncertainty (THU) model was estimated by calculating directly the key hardware and environmental uncertainties and indirectly by calculating the ray-path geometry without taking into account to the water surface condition (i.e., flat surface assumption).

2. RAY-PATH GEOMETRY

As mentioned in the Introduction Chapter, the ALB ray-path geometry is affected by the hardware and the environment. In an ideal environment with a flat-water surface (Figure 2.1), the ray-path geometry includes (Guenther, 1985):

- Transmission of a laser beam from the laser on the aircraft;
- Atmospheric interactions including absorption and scattering:
- Refraction and reflection at the water surface;
- Propagation through the water column including absorption and scattering;
- Reflection from the seafloor;
- Return along a near identical path back to the ALB receiver on the aircraft.

In this chapter, the radiometry and geometry an ALB laser beam with idealized water-surface conditions will be described.

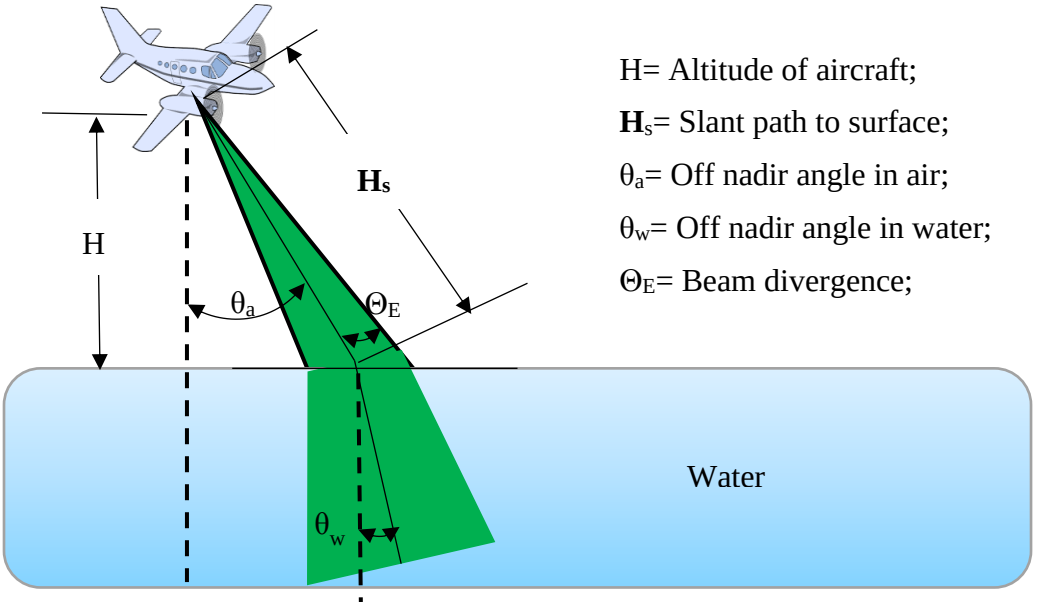

Figure 2.1: Basic ray path geometry of ALB beam refracting into water.

2.1 Transmission from the ALB System

In this study, I assume that the green (532nm) ALB laser beam transmitted from an aerial platform through the atmosphere onto the water surface can be approximated as a point source with a beam divergence Θ_E. It is possible to track the path and length of the laser beam in air $\boldsymbol{H}_s$ using ray tracing, where the off-nadir angle in air, θ_a, and the aircraft altitude, H:

$$\boldsymbol{H_s} = \frac{H}{\cos(\theta_a)} \tag{2.1}$$

Once a simplified ALB beam-path geometry from the aircraft to the water surface has been determined, the beam itself is described using the beam divergence angle, Θ_E. This angle determines the full width half max (FWHM) beam diameter on a plane perpendicular to $\boldsymbol{H_s}$. Similar to the transmitting unit (i.e., the laser), the ALB receiver has also a field of view, Θ_R, that collects the return laser beam energy. The beam divergence produces a conical beam with beam front that would typically be modeled by a spherical cap. However, if the beam divergence angle, Θ_E, is sufficiently small (i.e. less than 100 mrad as found in ALB systems), then the beam front can be approximated by a plane perpendicular to path length vector, $\boldsymbol{H_s}$, according to the small-angle theorem. This assumption allows the beam diameter, d_{surf} just before interacting the water surface to be approximated as (Figure 2.2)

$$d_{surf} = \boldsymbol{H_s} * \Theta_E \ . \tag{2.2}$$

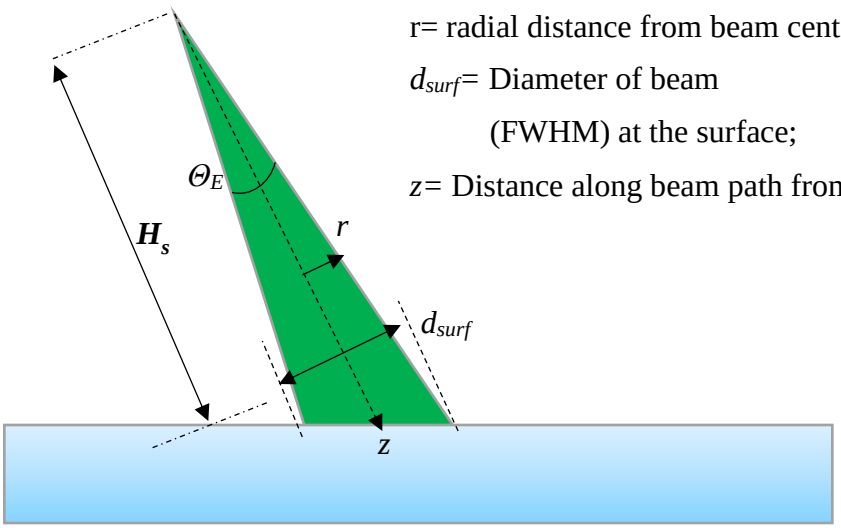

Figure 2.2: Beam properties near water surface.

The most common model of intensity for a laser beam cross section (in the plane perpendicular to the transmit vector $\boldsymbol{H_s}$) is a Gaussian distribution or transverse electric mode (TEM) 00 (Measures, 1992). As the beam diverges, the laser energy across the beam cross section is not distributed uniformly. Instead, higher intensity is near the center of the beam and decreases toward the edges (Figure 2.3). The distribution intensity within the beam cross section may be modeled as follows (Coastal Engineering Manual, 2017):

$$I(r,z) = I_0 \left(\frac{d_0}{d(z)}\right)^2 \exp\left(-\frac{2r^2}{d(z)^2}\right) \tag{2.3}$$

Where I_o is the intensity at the aperture of the beam, d_o is the diameter of the beam at the aperture, r is the radial distance from the center of the beam, and $d(z)$ is the diameter of the beam at the distance z along the beam path (i.e., range along the vector $\boldsymbol{H_s}$). Using equation 2.3, it is possible to substitute z for $\boldsymbol{H_s}$ in order to model the Gaussian beam footprint in three dimensions.

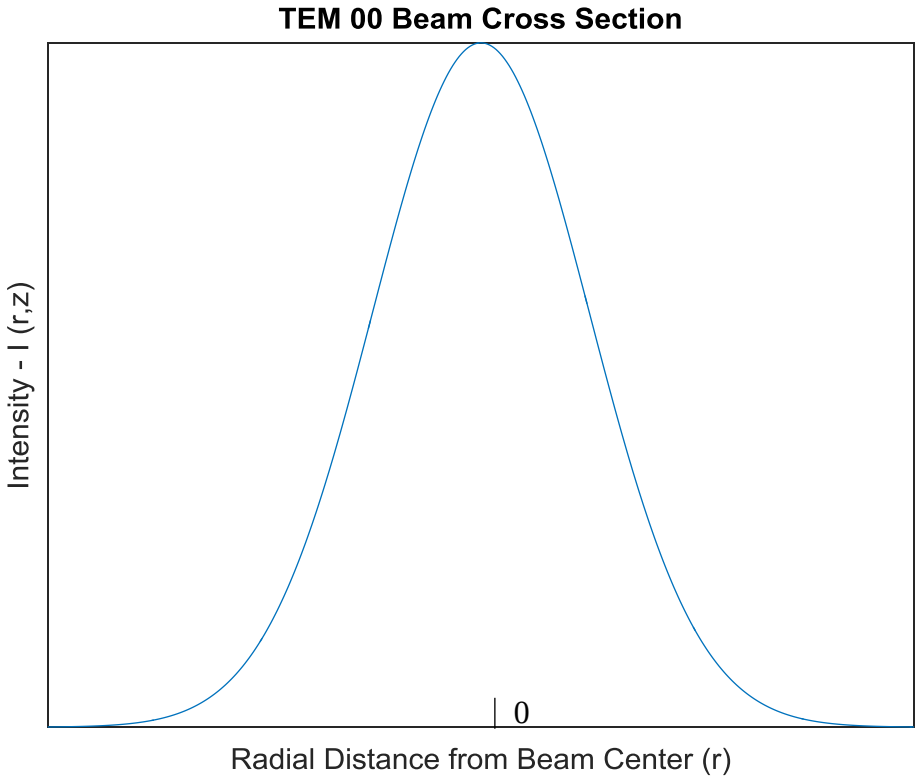

Figure 2.3: Example of a Gaussian (TEM 00) beam intensity distribution.

2.2 Interaction of the ALB Beam with the Water Surface

The interaction of the ALB beam with the water surface is the first significant signal observed in the ALB waveform. After propagating through the air, the ALB beam reaches the water surface. The difference in the speed of light between the air and water causes the rays to refract following Snell's Law:

$$\frac{\sin\theta_a}{\sin\theta_w} = \frac{n_w}{n_a} \ . \tag{2.4}$$

Where, θ_a is the angle of incidence above the water surface and θ_w is the angle of refraction after the ray is passed into the water. The dimensionless refractive index of air, η_a, and water, η_w, are approximately 1 and 1.33, respectively (Mobley, 1994). Snell's law describes the change in path of a light ray when it passes through the air water interface (Figure 2.4).

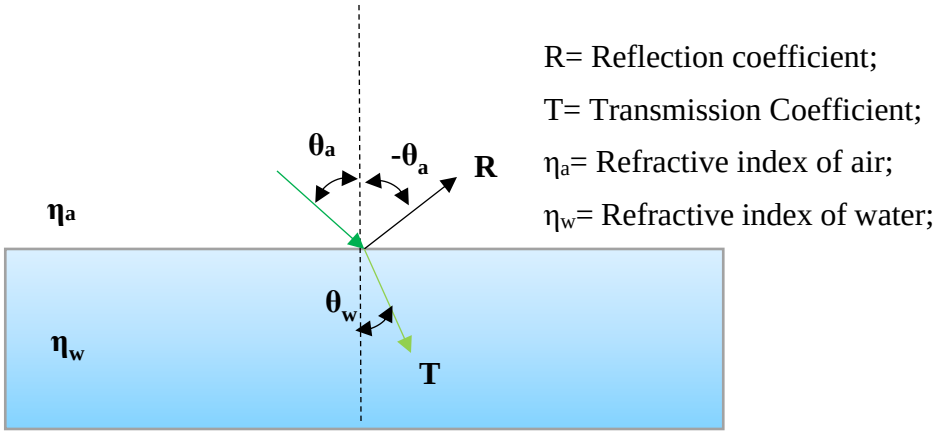

Figure 2.4: Snell's Law

Depending on the organic content, as well as other scattering particles in the water, around 2% or less of the laser beam energy does not penetrate the water and is reflected back to the ALB system along the same path (Bunkin &Voliak, 2001). Fresnel's law describes the laser energy that is reflected off of the water surface when it interacts with a medium of different refractive index, such as the transition from air to water. The portion of light reflected (R) and refracted (T) can be modeled with Fresnel's equations as follows:

$$R = \left|\frac{n_a \cos(\theta_w) - n_w \cos(\theta_a)}{n_a \cos(\theta_w) + n_w \cos(\theta_a)}\right|^2 \quad (2.5)$$

$$T = 1 - R \quad (2.6).$$

The refracted light propagates along the path described by θ_w in equation 2.4, while the reflected light continues along a path described by $-\theta_a$ (Figure 2.4). In flat water surface conditions, the laser light would only be reflected back to the receiver when θ_a is at nadir. Surface detection using green (532nm) laser light assumes that strong backscattering occurs in the first several millimeters of the water column and is typically caused from capillary reflections (Guenther, 1985).

Due to the off nadir angle of the laser beam, the full wave front of the beam does not intersect the water surface at the same instant in time, but rather different sections of the beam reach the surface at different times. The resulting beam diameter on the water surface can be modeled as an elliptical cross section described by the intersection of a plane with a cone. This effect causes the transmitted laser pulse width to broaden and is known as "geometric stretch" or "temporal stretch (Figure 2.5). The time when the center of the pulse reaches the surface is defined as t_{sf} (i.e., $t_{sf} = H_s/c$), where t_1 and t_2 are the times when each edge of the pulse reach the surface just before ($t_{sf} - \Delta t_{sf}/2$) the pulse center reaches the surface and after ($t_2 = t_{sf} + \Delta t_{sf}/2$) the pulse center reaches the surface, respectively. The temporal stretch of the pulse in units of time is defined as:

$$\Delta t_{sf} = \frac{2 d_{sf} \tan(\theta_a)}{c} . \tag{2.7}$$

Where, d_{sf} is the diameter of the beam just before it encounters the water surface, and c is the speed of light in air (2.998×10^8m/s).

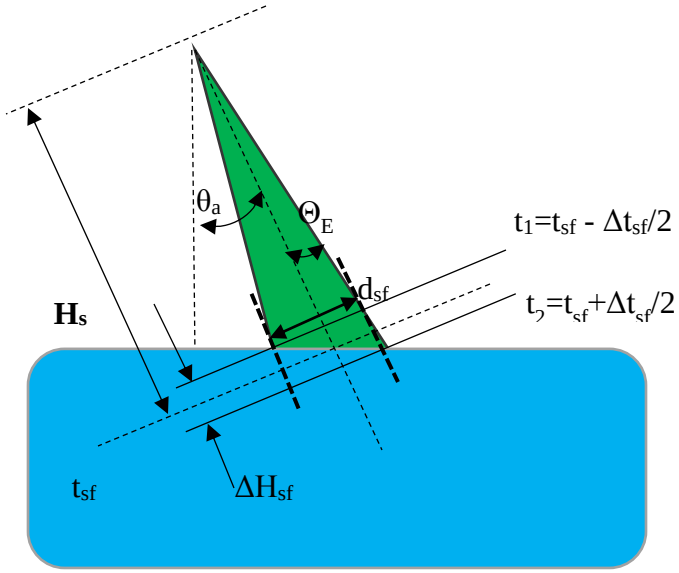

Figure 2.5: Geometric stretch of laser beam on the water surface.

2.3 Total Propagated Uncertainty (TPU) of ALB Depth Measurements

For each transmitted pulse that is received back by the ALB system, the water depth is determined by analyzing the signals contained in a time record of the logged energy (i.e., waveform). The shape of the obtained waveform is dependent on ALB's system parameters (e.g., laser beam divergence, transmitted laser pulse length, receiver field of view, bandwidth and sampling rate of the ALB detector and digitizers) and environmental factors (e.g., water surface conditions, water column scattering, and bottom composition) (Thomas & Guenther, 1984). Waveforms are typically binned up to 1 ns resolution, which is equivalent to a depth resolution of 0.1125 m underwater based on a two-way travel time and the speed of light in water (0.225 m/ns). The temporal width of the surface return will depend on two factors: duration of the transmitted laser pulse and the geometric stretch of the laser beam caused by the off-nadir reflection from the water surface (the whole wave front does not reflect at the same instant in

time). The bottom return will be further effected by water column scattering and seafloor characteristics including slope and roughness. The depth is calculated by accounting for the slant path of the beam through the water and performing TOF calculations. The depth will be reported for each successful waveform that is recorded.

It is common practice to provide an uncertainty value for each ALB depth measurement in order to report the quality of the ALB survey and to allow efficient post-processing procedures to edit and clean the data (IHO, 2008). In addition to the radiometric uncertainties related to the ALB's hardware and the environmental factor, the ALB measurement contains geometric uncertainties related to the positioning (i.e., GPS), attitude (i.e., IMU) systems and the alignment of the ALB transmitter and receiver units mounted with respect to the reference system of the aircraft (Pe'eri, 2017). In this study, I will focus only on the depth measurement errors related to the optical uncertainties, as the geometric uncertainties have been investigated in many studies in the past (White et al., 2011; Baltavias, 1999). In addition, I assume that the geometric uncertainties are typically reported by the manufacturer or determined by performing a boresight calibration. Environmental uncertainties resulting from the laser beam interaction with the water surface, water column and the seafloor are much more difficult to predict and account for. This study examines the contribution of short-wavelength surface waves (wavelength less than 0.1m) on the Total Horizontal Uncertainty (THU) and Total Vertical Uncertainty (TVU) of ALB measurements. The error caused by the waves can be measured though changes in the sub surface slant path (wave refraction error).

If the water surface causes a deviation in the beam slant path that is different than the still water assumption then some horizontal and subsequently vertical error is introduced into the measurement. Figure 2.6 illustrates the effect of a change in the sub surface slant path. In 2D

space, the horizontal error (*ΔX*) is the difference between the assumed location of the beam center over flat water conditions and the actual beam center over a water surface containing waves that cause additional $\Delta\theta$ refraction angle deviation (from the still water assumption) in the ray-path geometry. As a result of the new slant path, error is introduced into the TOF water depth calculation causing a change in slant path length (*ΔSP)* and a resulting vertical error (*ΔZ*). The horizontal and vertical errors due to the deviation from a flat water surface are as follows:

$$\Delta X = \boldsymbol{SP_2} * \sin(\theta_w + \Delta\theta) - \boldsymbol{SP_1} * \sin(\theta_w) \tag{2.8}$$

$$\Delta Z = \Delta SP * \cos(\theta_w) \tag{2.9}$$

Where, SP_1 is the flat water slant path length, SP_2 is the actual slant path length and θ_s is the off-nadir beam angle.

Due to the fact that $\Delta\theta$ and ΔSP are unknown, the measurement error is reported as an uncertainty. Following IHO S-44 standards, the uncertainty of ALB measurements is reported as the 2-sigma standard deviation (~95% confidence interval) about the measurement (IHO, 2008). This study will provide uncertainty values caused by surface waves, an effect that will be referred to as wave refraction angle error ($\Delta\theta$).

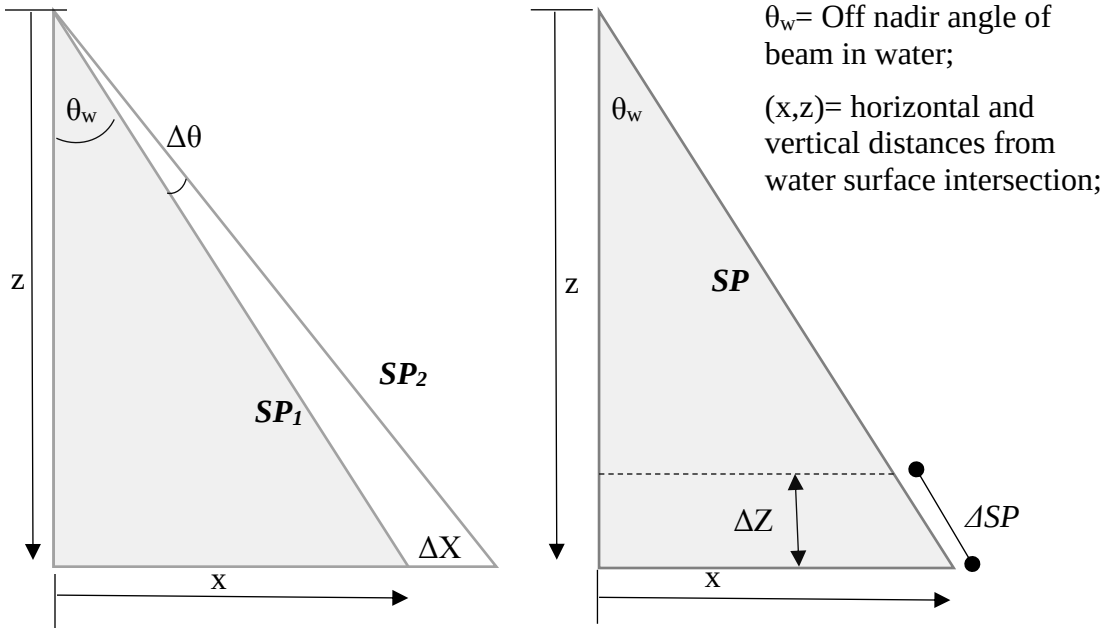

Figure 2.6: An illustration of the effect of slant path error as depicted by Karlsson, 2011. The error in refraction angle causes a horizontal error (ΔX) and a vertical error (ΔZ).

3. WATER SURFACE CHARACTERISTICS

In real-world survey conditions, the water surface is rarely smooth and level although commercial ALB processing software typically treat it as such. The air-water interface (i.e., water surface in natural conditions) is a dynamic non-uniform boundary constantly undergoing deformation by surface waves that propagate along and across the boundary (Dean and Dalrymple, 1984). Natural forces (such as, wind, currents and depth) and man-made factors (such as, vessels in motion and coastal structures) are responsible for generating these surface waves near the coastline. Gravity waves propagate along the water surface and are defined by wavelengths greater than 0.1 m with gravity being the primary restorative force (Lighthill, 1978). Capillary waves and gravity-capillary waves have much smaller wavelengths (i.e., centimeter or millimeter level) and the primary restorative force acting on these waves is surface tension of the fluid. Linear wave theory is sufficient for describing both of these types of waves and will be used for modeling different surface wave scenarios. The Beaufort scale (Figure 3.1) is a qualitative visual scale widely used by mariners and surveyors to describe the wind and wave conditions. ALB surveys are typically conducted at conditions below a Beaufort level 3 (i.e., winds 4-5 m/s or 7-10 knots) to avoid the presence of white caps and spray that reduces system performance. As such, this study focuses on waves in the capillary and capillary-gravity wave regime (wavelength < 0.1 m) that commonly rise from the interaction of wind (1-5 m/s) over the water surface.

Beaufort number	Description	Wind speed		Sea conditions
		kts	m/s	
0	Calm	< 1	<1	Flat.
1	Light air	1 – 2	1	Ripples without crests.
2	Light breeze	3 – 6	2-3	Small wavelets. Crests of glassy appearance, not breaking
3	Gentle breeze	7 – 10	4-5	Large wavelets. Crests begin to break; scattered whitecaps
4	Moderate breeze	11 – 15	6-7	Small waves with breaking crests. Fairly frequent white horses.
5	Fresh breeze	16 – 20	8-10	Moderate waves of some length. Many white horses. Small amounts of spray.
6	Strong breeze	21 – 26	11-13	Long waves begin to form. White foam crests are very frequent. Some airborne spray is present.
7	High wind, Moderate gale, Near gale	27 – 33	14-17	Sea heaps up. Some foam from breaking waves is blown into streaks along wind direction. Moderate amounts of airborne spray.

Figure 3.1: The Beaufort wind scale. ALB surveys are limited to conditions less than Beaufort scale 3. Encyclopedia Britannica (2009).

There is inherently a great deal of randomness associated with wind-driven surface waves, therefore statistics is the best method to describe this complex boundary. The radiative transfer theory of the water surface is strongly related to the development wave mechanics theory and statistics (Mobley, 2004). Surface reflection of sun glint was used to describe wave action and relate it to wind and bathymetry (Cox and Munk, 1954; Cox and Munk, 1956). The same wave mechanics theory was used to describe the solar light field underwater (Preisendorfer and Mobley, 1985; Preisendorfer and Mobley, 1986; Mobley and Preisendorfer, 1988; Mobley, 1994). These principles of light interaction with the water surface have been used to generate theoretical models of an ALB beam interacting with a water surface disturbed by wind (e.g., Tulldahl and Steinvall, 2004; Karlsson, 2011).

3.1 Linear Wave Theory

Linear wave theory (also known as Airy wave theory) describes the complex water surface as the superposition of many monochromatic waves (Dean and Dalrymple, 1984). In classical wave mechanics theory, a monochromatic surface wave (sinusoidal) can be described by its wavelength, *L*, amplitude, *H*, and the depth of water it is propagating over, *d* (Figure 3.2). In natural conditions, the surface waves are dispersive (i.e. celerity depends on wavelength) and their formation is inherently random. As a result, the surface waves alter both elevation and slope of the water surface over time and space (Kumar et al, 2006), making it challenging to calculate the exact incidence angle of an ALB beam on the water surface for any given pulse.

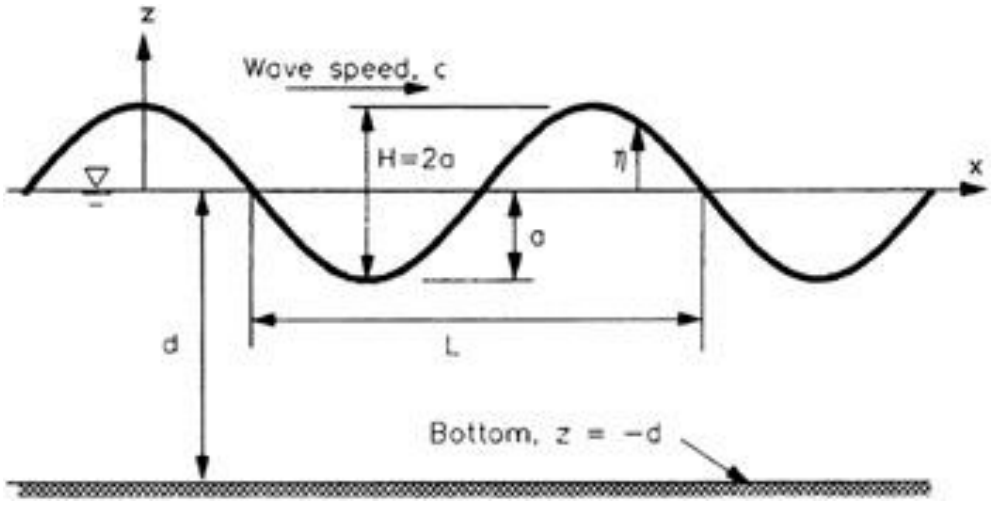

Figure 3.2: A progressive wave modeled by Airy wave theory. Image from Dean and Dalrymple (1984).

Wind-driven waves can vary in wavelength from centimeter scale up to hundreds of meters depending on the force of the wind as well as fetch and duration (Dean and Dalrymple, 1984). Linear wave theory provides a method to describe a complex water surface if the individual monochromatic waves can be characterized (Krogstad, 2000). The linear wave theory assumes that the natural water surface is a superposition of many single-frequency waves that have an

elevation η with respect to the Mean Sea Level (MSL) for a given horizontal position *x* (i.e., the horizontal distance from an arbitrary origin) at time *t,* following the wave equation:

$$\eta(x,t) = a * cos(kx - \omega t), \tag{3.1}$$

Where, *a* is the half peak-to-peak amplitude of the wave, *k* is the angular wave number, and ω is the angular frequency. This model considers wave motion to be circular in time with sinusoidal propagation through space. Although the physical wave interactions are highly non-linear in nature and require hydrodynamics calculations, the linear wave theory is considered a reasonable approximation for water surface representation as long as waves do not have interaction with the bottom (depth dependence) and are far enough from the surf zone with no presence of breaking waves break (Krogstad, 2000). Lighthill (1978) has shown that this circular wave motion is true for deep-water gravity waves, as well as for smaller capillary waves. Waves are considered deep-water waves when the water depth is at least half the wavelength of the water surface waves:

$$d \geq L/2. \tag{3.2}$$

Thus, any given water surface can be separated into many monochromatic waves (Equation 3.1) using superposition concept, where the wavelength of largest waves needs to meet the deep-water criterion (Equation 3.2). An example of linear wave theory and super position is presented in Figure 3.3, where the random surface can be decomposed into its monochromatic elements.

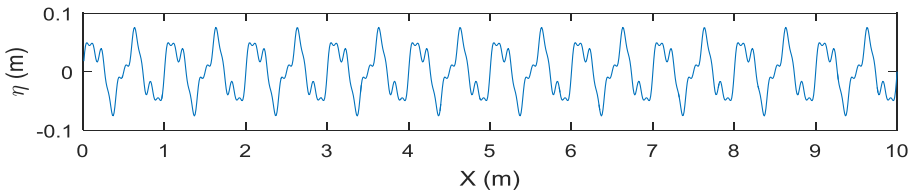

a)

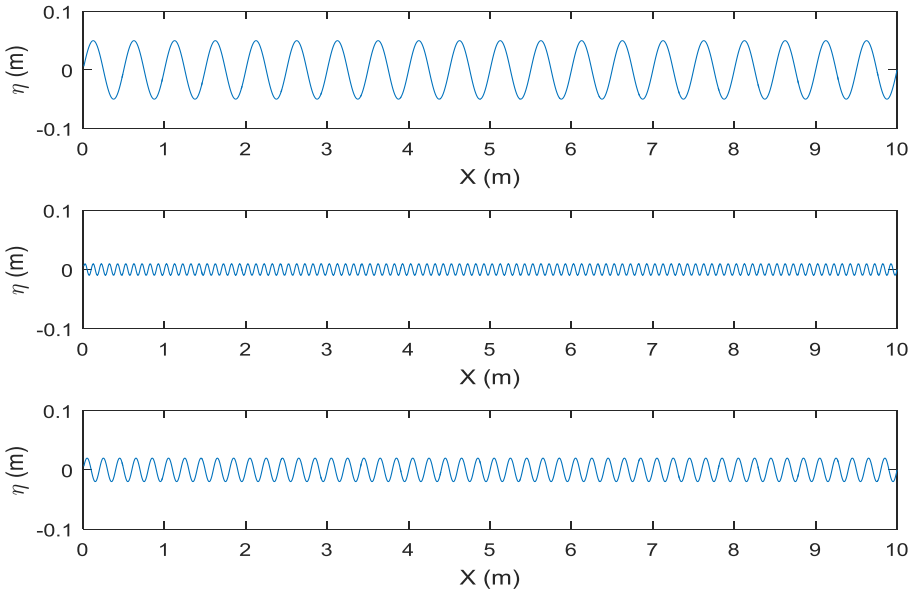

b)

Figure 3.3: A surface composed of several waves (a) can be separated in to the individual monochromatic elements (b).

3.2 Beam Interaction with Water Surface

Considering that a typical ALB beam footprint on the water surface is between 0.25 m and 4 m diameter (Quadros, 2013), the wavelength of surface waves can be large or small compared to beam footprint diameter. Waves with wavelengths greater than the beam footprint diameter alter the surface such that the whole laser beam interacts with a relatively constant slope. A surface

slope that deviates from the flat-water case changes the laser beam's incidence angle on the water surface and causes the underwater slant path of the whole laser beam to change accordingly (Figure 3.4). The depth error caused by a constant-slope contribution may be corrected for by running more rigorous processing of the surface return, such as referencing each surface detection to orthometric height and using a 2D low-pass filter on the surface data (Guenther, 1985; Guenther, 1990). A wind-driven water surface will cause the laser beam to refract non-uniformly due to the range of surface slopes that the beam encounters. The shifting the slant path (i.e., shifting the geographic location of the ALB footprint on the bottom) and the distorting the footprint's shape on the bottom (i.e., contribution within the footprint to the depth measurement) will result in an additional uncertainty to the ALB measurements.

Short-wavelength wind waves ($L < 0.1$ m) create multiple wave crests within a single laser beam footprint. The rough water surface is necessary to collect optic backscatter for a surface return, but the water surface also distorts the refracted light field of the laser beam as it transmits into water column (Steinvall, 1994). Short wavelength ripples are highly random and may steer the ray-path geometry underwater and distort the beam footprint. Because it is nearly impossible to measure short-wavelength wind waves *in situ*, a wave refraction uncertainty should be added to the ALB TPU reporting. Uncertainty evaluation of these capillary and gravity-capillary wave conditions can be estimated using numerical modeling. Ray-path simulations for different water surface conditions can be generated using common numerical modeling techniques (such as, Monte Carlo). Using parameters that dictate the ALB ray-path geometry, (i.e., ALB hardware specifications, standard survey operations, and elevation models of typical water surfaces), the laser beam path below the water surface can be modeled and analyzed. The method of water surface simulation is outlined in the next section.

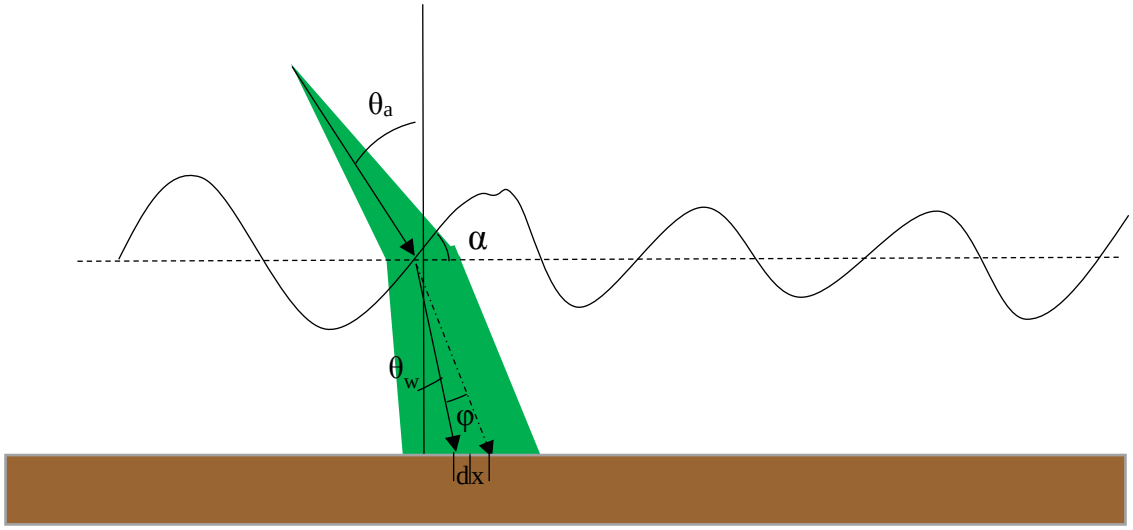

Figure 3.4: Altered slant path of laser beam due to variation in water surface slope causes a vertical and horizontal error in the measurement. Most ALB systems have no correction for this error.

3.3 Elevation Models for Water Surfaces

Preisendorfer and Mobley (1985) developed a procedure to simulate solar light fields underwater using the linear wave theory in a 3D space. Similar to the 2D space example (Figure 3.3), the water surface in 3D space can be described using monochromatic waves with distinct wavelengths, amplitudes and headings (as waves undergo some spreading they may not all propagate along a parallel path). An example is provided in Figure 3.5. A common tool to decompose a complex water surface is Fourier transforms that can describe the surface using directional-wave spectrums (Mobley, 1994*)*. The directional-wave spectrum contains information on monochromatic wave energy contained over frequency and direction of propagation.

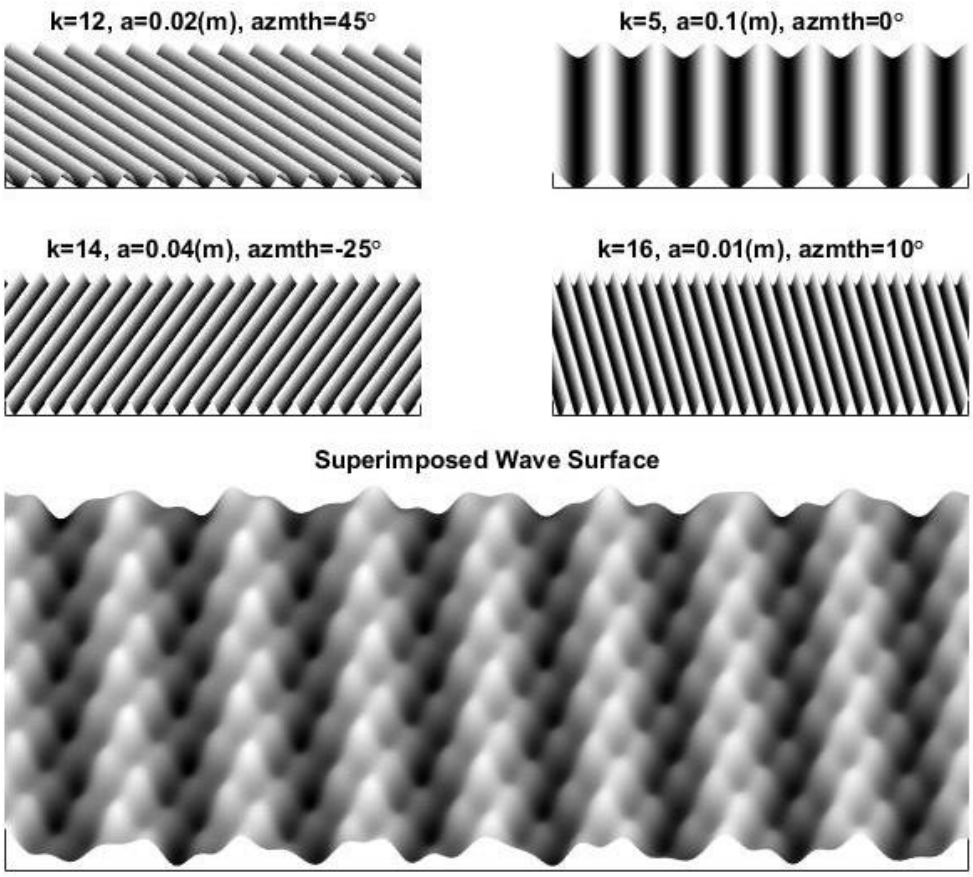

Figure 3.5: Four monochromatic waves of different size and propagating in different directions superimpose to form a complex water surface.

In order to numerically model a realistic water surface, this study follows the methodology provided by Mobley (2014) that begins with a 1D wave spectrum that may be converted to a water surface by:

1) Generating a 1D wave energy spectrum,
2) Applying a wave spreading function,
3) Adding random Hermitian amplitudes for uniqueness,
4) Calculating the inverse Fourier transform of the spectrum.

The first step in Mobley's (2014) approach is to develop the relationship between the wind over water and the resulting 1D wave energy spectrum (Demirbilek and Linwood, 2002). The wave

spectrum expresses the wave energy (related to the amplitude and period of the wave) of each wave frequency present on the water surface. Different sea states will have unique energy distributions along the wave spectrum according to environmental conditions (i.e., wind and depth). A light wind (below Beaufort 3) with a fetch less than 30 m will only produce small capillary waves while a large storm event (winds over 15 m/s, fetch greater than 10 km) will produce gravity waves with amplitude on the order of meters and wave periods less than 1 second. According to Preisendorfer and Mobley (1985), by relating these spectral-wave distributions to wind conditions such as wind speed, fetch, and wind duration then realistic water surface models may be constructed for radiometric transfer analysis.

In the second step, Apel's (1994) wave energy spectrum was selected. This wave function is a modified version of the JONSWAP spectrum developed by Hasselmann, et al. (1973) that includes an improved prediction of capillary and gravity-capillary waves that are of interest to this study. The Apel wave spectrum was developed for sea states rising from short fetch winds (<1 km) in somewhat shallow waters (<100m), which are similar to typical ALB surveys that are conducted near shorelines with limited fetch. ALB surveys are typically conducted in waters shallower than 60 m, a depth that for wave modeling is considered shallow. The Apel (1994) wave spectrum S(f) is based on observations of developing wind waves and does not assume fully-developed sea states by considering limited fetch cases. An example of the Apel's spectra with very short fetches is presented in Figure 3.6. More details on the Apel (1994) spectrum may be found in Appendix A.

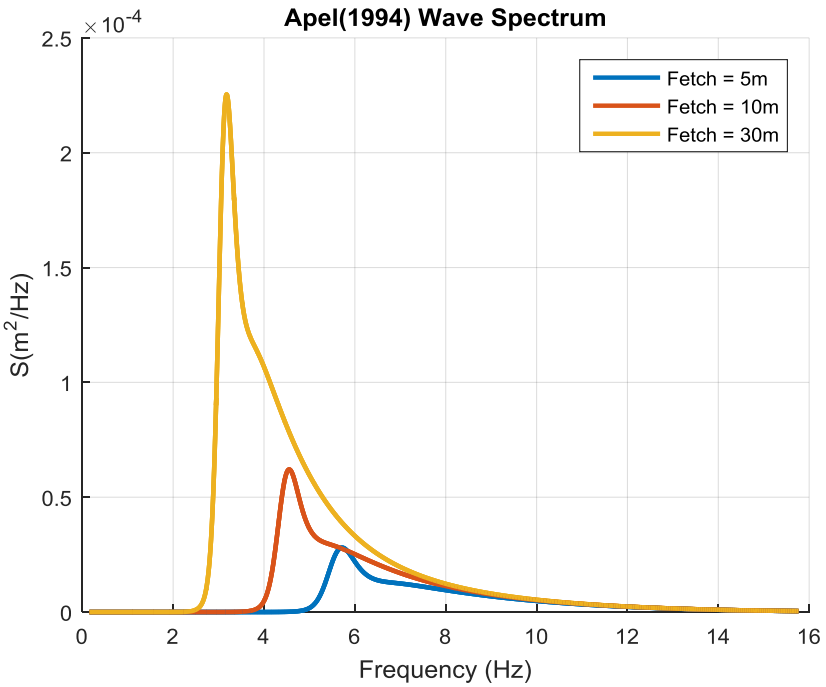

Figure 3.6: Example Apel wave spectra with very short fetches to simulate experimental conditions. U10=5m/s.

Apel's wave spectrum along with a wave spreading model will be used to generate a 2D wave spectrum necessary to implement the Mobley (2014) water surface modeling technique. The wave spreading model aims to estimate spread of possible wave propagation directions rather than falsely assuming that all waves will propagate in the same direction as the wind. The water surface model used in this study is a cosine-2S wave spreading function that described the directional spreading function $D(f,\theta)$ in terms of frequency f, and angle ψ from the mean wind direction ψ_0 (Coastal Engineering Manual, 2001):

$$D(f,\theta) = \frac{(2^{2s-1})}{\pi}\left(\frac{\gamma^2(s+1)}{\gamma(2s+1)}\right)\cos^{2s}\frac{\psi-\psi_0}{2} \quad , \tag{3.3}$$

where γ is the gamma function, and s is the spreading parameter. The cosine spreading function is provided in Figure 3.7. It is important to note that there is less wave spreading at larger *s* values

that are related to lower frequency waves (i.e., gravity waves). In this study, high frequency waves related to capillary and gravity-capillary have a spreading *s* value of 1 or 2 (Mitsuyasu, 1975).

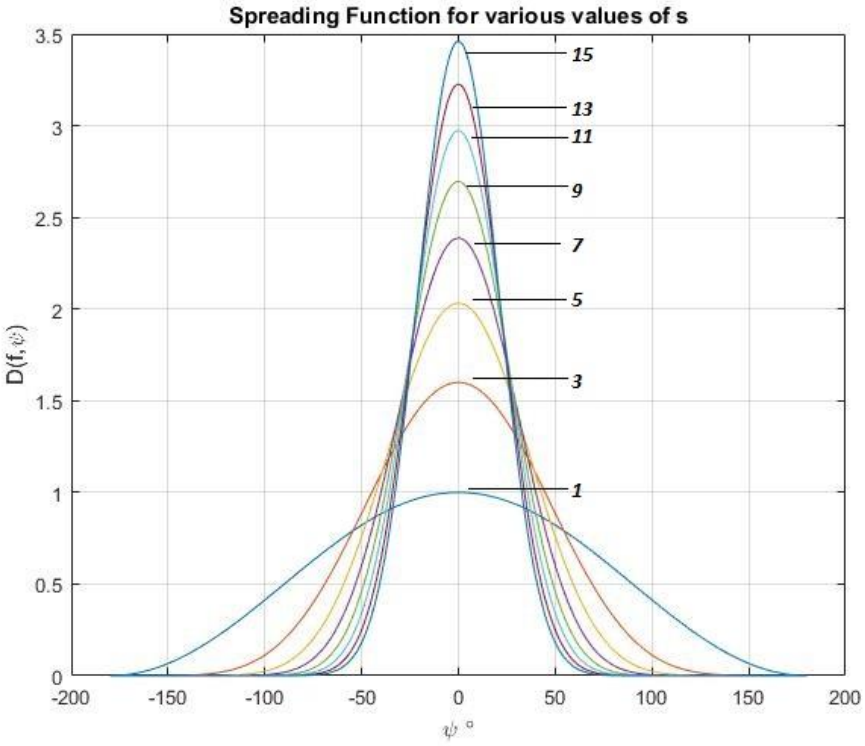

Figure 3.7: Wave spreading function based on the cosine squared model. Larger values of s correspond to longer gravity waves.

The full 2D direction wave spectrum, $E(f,\psi)$, may be calculated by taking the product of the cosine spreading function and Apel's wave spectrum:

$$E(f,\psi) = S(f) * D(f,\psi). \tag{3.4}$$

A directional wave spectrum was calculated for a fetch of 5 m and wind speed of 5 m/s. This resulted in the 2D directional spectrum seen in Figure 3.8.

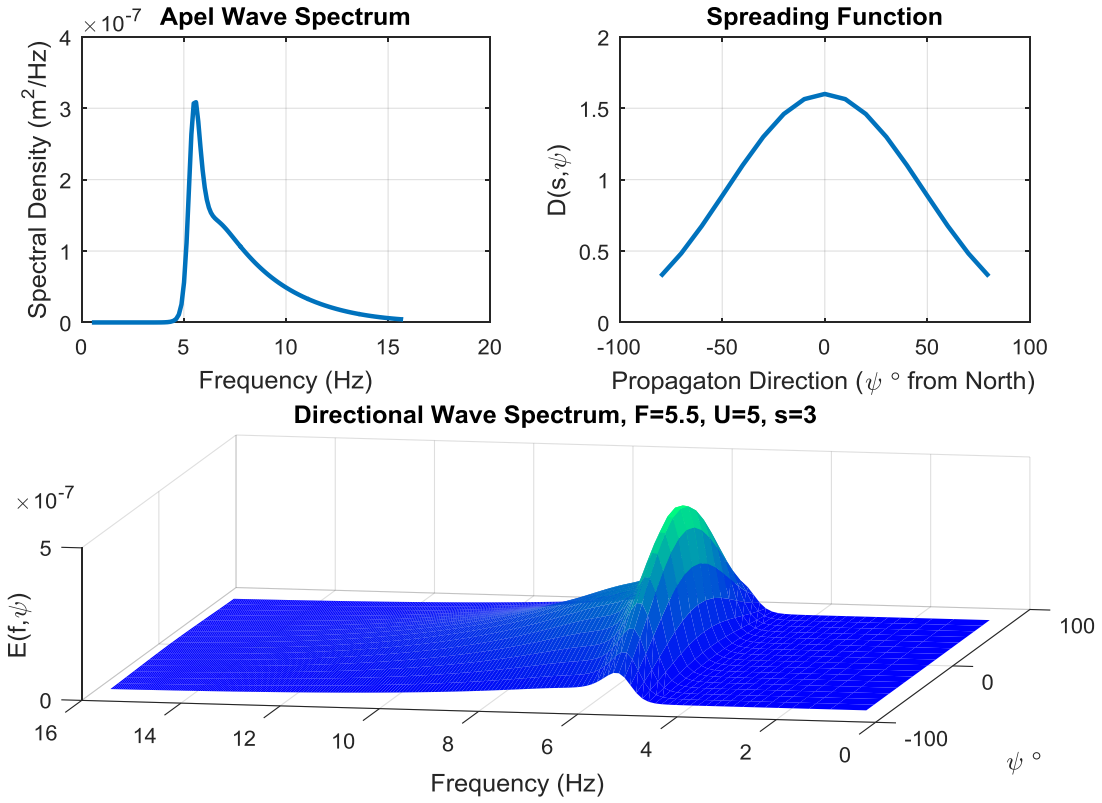

Figure 3.8: Wave spectrum, spreading function, and directional spectrum for an Apel wave spectrum model with U=5m/s, fetch =5m.

The last two steps are generating a 2D two-sided directional spectrum and calculating the random Hermitian amplitudes (Mobley, 2014). Normally distributed random Hermitian amplitudes allow each realization of the water surface to be unique while preserving wave energy distribution when performing Monte Carlo simulations. For detailed explanation of these calculations see Mobley (2014). Figure 3.9 provides an example of the two-sided spectrum with the real and imaginary Hermitian amplitudes used to create the 0.5m by 0.5m area of water surface elevation. The numerical water surface generated retains the same 2D wave energy distribution shown in the observed wind-spectrum models (section 5.1).

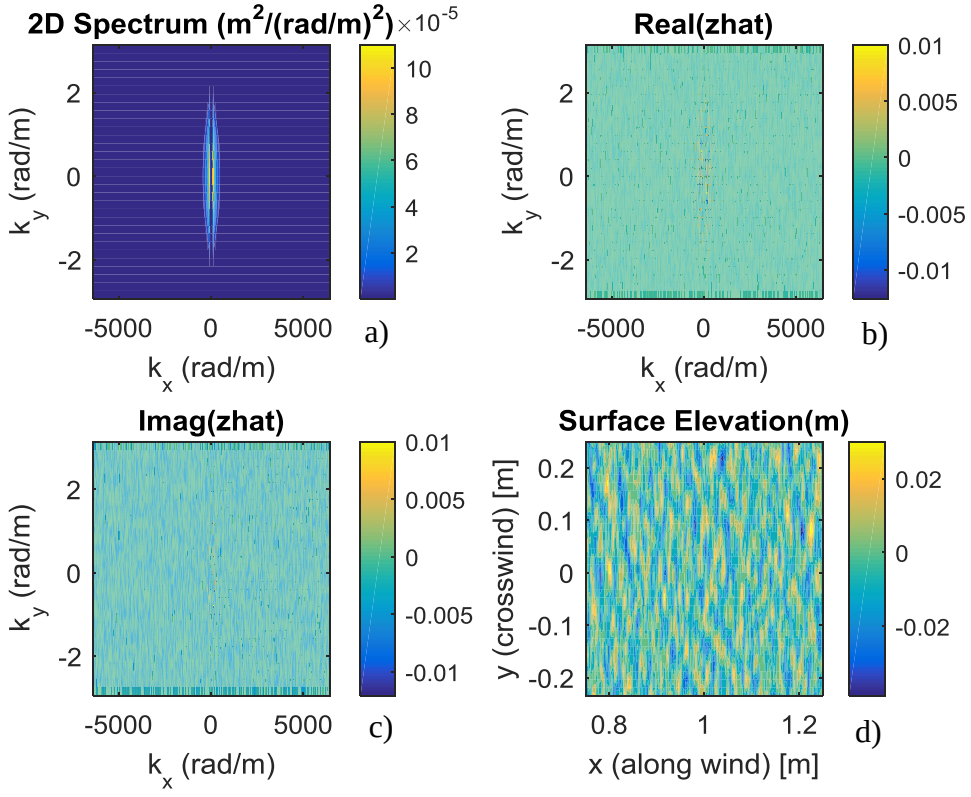

Figure 3.9: a) The two sided wave spectrum. b) The real Hermitian amplitudes. c) The imaginary Hermitian amplitudes. d) The water surface realization for a small patch of water (0.5 m x 0.5 m).

The computer generated water surfaces such as the one in Figure 3.9 d) allow different environmental and ALB system parameters to be assessed. Using Monte Carlo ray trace simulations, statistical information was gathered to study how factors including wind speed, wind direction, beam incidence angle, and beam diameter changed the deviation of the mean beam refraction angle through the model surfaces. The simulations were used to estimate initial parameters to be examined in depth using empirical methods (see chapter 5).

4. METHODOLOGY

The goal of the experimental apparatus was to examine water-surface wavelets contribution on lidar refraction angle uncertainty and accuracy of ALB measurements. Experimental datasets were generated by measuring a 532 nm laser beam footprint that had refracted through wind-generated waves. Published computer models (i.e., Tulldahl and Steinvall, 2004; Karlsson, 2011; Wang and Philpot, 2007) were used in the study for comparison to the empirical measurements collected. Water surface conditions in the experiments and the simulations considered were made to resemble relatively calm sea states that would be present in a typical ALB survey (winds below 10 m/s, lack of large swell). Assuming that the wind speed and sea-state conditions can be measured during the survey time (Stephen White – NOAA/NOS/NGS/RSD, 2016), the wave refraction uncertainty associated with the ALB measurement can be quantified with respect to environmental conditions.

Empirical data for the study were collected in a well-controlled laboratory condition at UNH Chase Ocean Engineering facilities. A 120-ft long (36.5 m) wave tank combined with a large industrial fan was used to generate water surface conditions corresponding to the desired sea state. An underwater optical detector array along with a high speed camera were used to perform laser beam diagnostics. The detector array used 36 photodiodes spaced in a square grid of 0.25x0.25 m. This array provided information on the laser beam footprint's shape and its refracted angle below the water surface (i.e. down-welling path). A high speed camera located behind a diffusor plate was used to image the laser beam footprint for the upwelling path of the laser beam. Using the experimental setup, the effects of water surface waves (wavelength range from 0.01 to 0.1 m) on a laser beam with 0.2 m beam diameter at the water surface were measured over a set of off-nadir angles. The laser beam was imaged just after refracting through

the air-water interface, 0.25 m below the water surface. Changes of the laser beam footprint were compared to those of a flat water surface (still water conditions) in order to validate the study results and asses current ALB range calculation used in commercial software. The refraction angle deviations and changes in beam footprint diameter were also analyzed.

4.1 Ray Tracing Models

Because of the logistical constraints, a limited amount of ALB survey configurations can be conducted in empirical experiments. As a result, numerical modeling was used to identify key parameters for empirical analysis and infer their contribution to the TPU of the ALB measurements. After a realistic water surface elevation model was constructed over the spatial domain (section 3.3), the path of 10,000 individual light rays was traced through the water surface using the ray-path geometry defined in the chapter 2. Each ray represents a photon emitted from the ALB laser, where a large number of rays make up the whole laser beam. The refraction of each ray is calculated at the water surface and its sub-surface path of the beam is then be recorded at the location.

A water surface was generated according to Mobley's (2014) model. Three-dimensional points sampled at constant distances and were connected using Delaunay triangulation in order to create a water surface. This Digital Elevation Model (DEM) was used to construct the water surface from the computer model, where each triangle (i.e., facet of the surface) is a small individual plane that has a constant normal vector within its boundaries. Figure 4.1 provides an example of triangulation of the water surface by Delaunay triangulation technique.

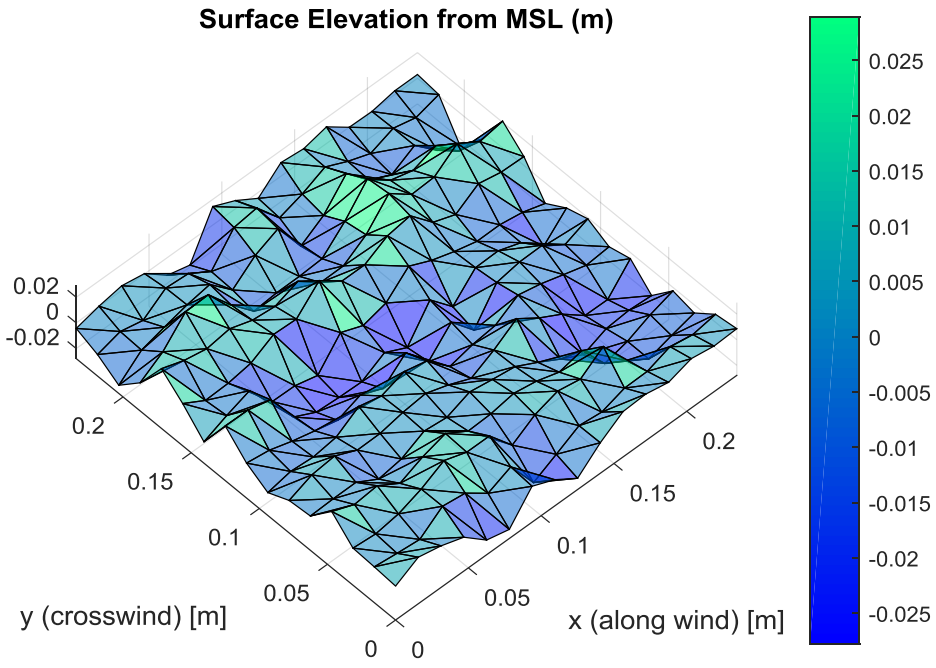

Figure 4.1: A magnified surface triangulated using Delaunay triangulation. The Apel spectrum for a fetch of 7.5m and wind speed of 5kts was used to find the surface elevation points.

Next, the laser beam was simulated using 10,000 rays normally distributed across the beam front according to the ALB beam divergance. The normal distribution simulates a Gaussian beam cross section with more light intensity at the center of the beam (i.e., higher density of rays). In this study, simulations assumed a beam divergence of 60 mrad was used. Figure 4.2 provides an example of the laser beam and its footprint (located 30 m above the water surface) incident on a wind rippled water surface model.

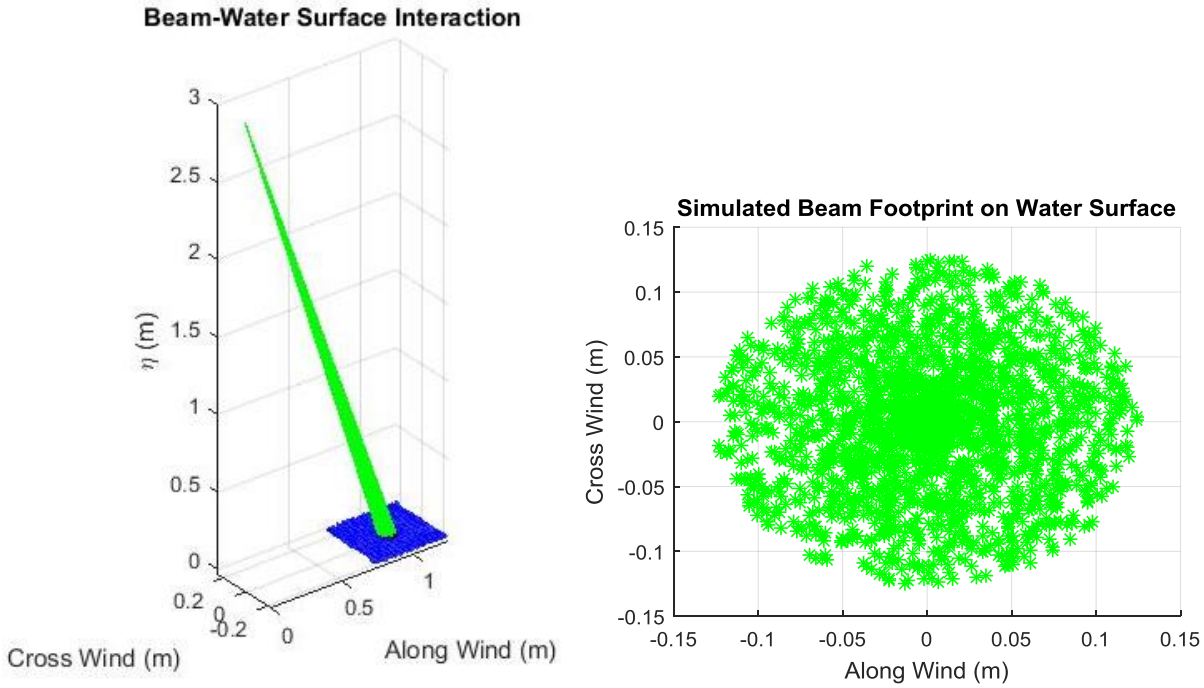

Figure 4.2: a) The simulation of 10,000 rays incident on the water surface model. In this case the beam is at a 20° incidence angle to the horizontal. b) the beam footprint on the water surface with Gaussian ray distribution

Using built-in MATLAB functions, the triangle that each ray intersects can be determined. The refraction of each ray is determined using the vector form of Snell's Law as follows,

$$s_2 = \left(N_{surf} \times \left(-N_{surf} \times s_1\right)\right) - N_{surf}\sqrt{1 - \left(\frac{\eta_a}{\eta_w}\right) \cdot \left(N_{surf} \times s_1\right)^2}\,, \tag{4.1}$$

where s_1 is the unit vector of the of incident ray, N_{surf} is the unit vector of the surface normal for the intersected triangle, and s_2 is the unit vector of the ray after undergoing refraction. The ray can then be traced below the surface using the s_2 unit vector (Figure 4.3).

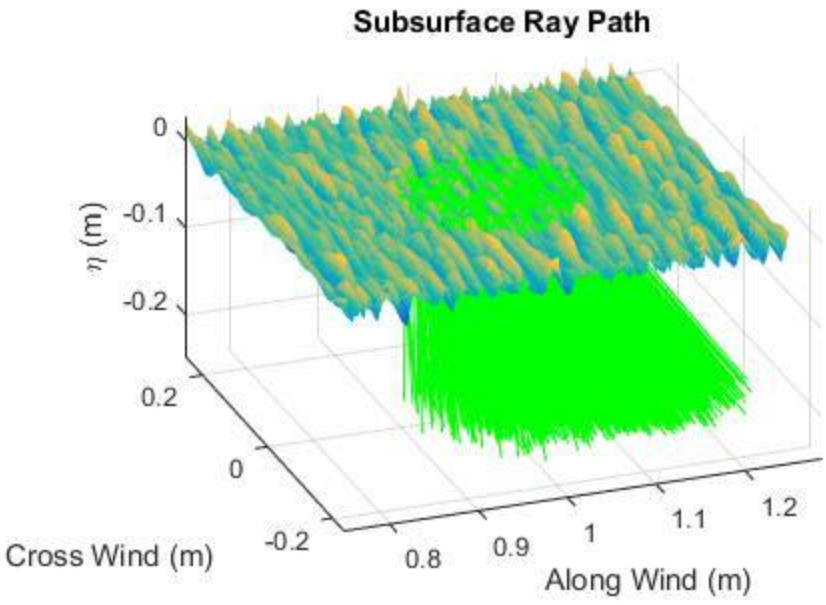

Figure 4.3: Rays refracting through the numeric surface, each ray was mapped to a depth of 0.25cm

Fresnel's equations were also considered in this computer model to accurately estimate the portion of light transmitted through the surface. Fresnel equations (section 2.2) describe the percent light transmitted and reflected based on incidence angle. In this model, the probability of a ray passing through the surface is determined using Equation 2.5. Based on reflection coefficient, a corresponding percentage of rays were reflected from the water surface, while the rest were transmitted into the water column. Each ray that passes through the surface contains a unique intersection point with the surface and a unit vector describing its sub-surface path. The ray information allows the ray path to be propagated below the surface. Light rays also undergo scattering and absorption as described in Chapter 2. In order to ignore the effects of the water column and focus on the water surface the light rays in this model were propagated to a depth of

0.25 m assuming an optically-clear water (no scattering). For each water surface realization, a sub-surface laser beam footprint can be modeled (Figure 4.4).

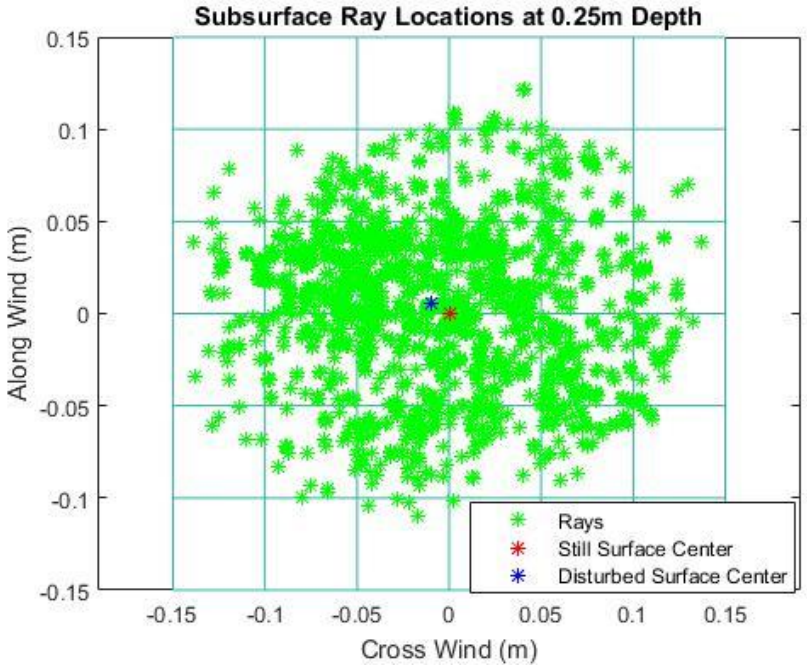

Figure 4.4: Sub surface beam footprint as predicted by the model. 1000 rays with a 0.1m beam diameter (FWHM) at water surface, $\theta i = 20°$.

During the study, 500 Monte Carlo ray trace realizations (unique water surfaces) were conducted each time a new parameter was considered. Parameters including wind speed, fetch, incidence angle, and beam diameter were considered. In each realization, the rays of each laser beam were transmitted through realistic randomly generated water surfaces. For each ray trace performed, the beam center of concentration (i.e. beam centroid) and beam footprint ellipsoid were calculated and recorded. The sub-surface location of the center of concentration of each footprint was calculated and compared to the center of concentration for a beam passing through a perfectly smooth (flat) water surface. Any difference between the results from the simulated water surface and the flat water surface indicates refraction deviation caused by capillary surface

waves. Figure 4.5 shows an example of the locations on the horizontal plane of the center of each beam (blue star) compared to the still water beam center (origin).

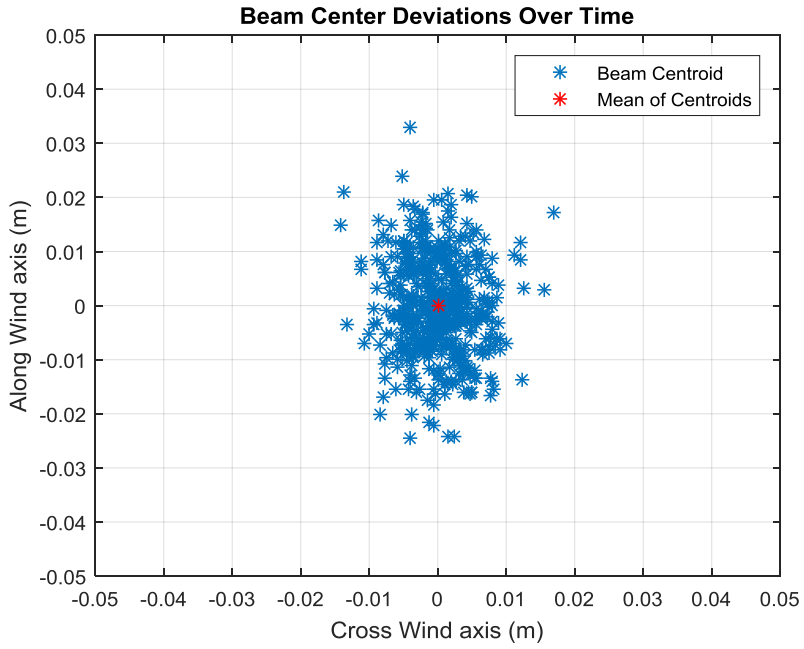

Figure 4.5: Model results for U=5.25 m/s, θ=15°. The blue stars represent the center of concentration of each unique beam that was analyzed, the red star is the mean of these results. The origin of the plot represents the still water center of concentration.

Each horizontal shift in the center of concentration was converted to an angular offset from the still water location in the along wind axis and the cross wind axis using the slant path of the beam. Finally, the angular standard deviation in the along and cross wind directions were calculated to estimate the refraction error caused by the waves. The standard deviation values are then used to compare the error associated with environmental conditions and beam characteristics.

4.2 Empirical Laser Beam Diagnostics

Typically, commercial ALB systems transmit a laser beam with a pulse duration of 1 to 5 ns with a small beam divergence that allows the beam-front to be approximated as a plane with Gaussian radial energy distribution from the center of the beam (USACE, 2017). An underwater optical detector array was designed and utilized in the study in order to analyze the radial distribution of laser beam energy (i.e., beam footprint) and measure changes in beam path below the surface, by sensing when the peak of the Gaussian curve deviates from the original beam center. The optical detector array provides spatial measurements of refracted laser beam footprints from still and rough water surfaces such that the effects of a rough water surface may be compared to an undisturbed case. The detector array itself is a planar detector array (Figure 4.6) consisting of 36 ThorLabs PD1A silicone photodiodes (Appendix B) arranged in a square planar grid (Eren et al, 2016). The photodiodes are spaced uniformly at a distance of 0.05 m from each other in a 6 X 6 grid. Each photodiode is mounted in a clear acrylic waterproof housing, allowing them to operate underwater. The photodiodes were connected to SubMiniture version A (SMA) coaxial cables with a 5 volt reverse bias applied. The SMA cables extend to a length of 5 m in order to allow the system to be submerged at different depths in the tank. The output from the photodiodes was digitized by analog-to-digital converters and was recorded using MATLAB at a 20Hz sampling rate.

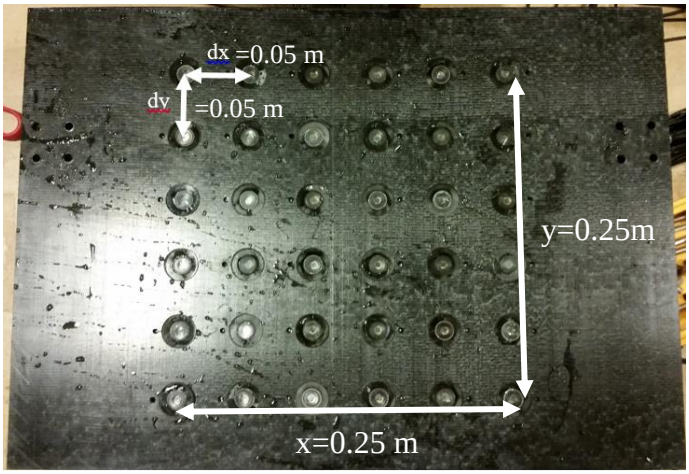

Figure 4.6: Optical detector array with acrylic waterproof housings.

This design of the optical detector array was developed such that there is minimal distortion of the laser beam signal. Unlike the most commercial camera systems, there is no gain applied to the analog output of the photodiodes. This allows a simple linear conversion from the bit output to a laser intensity value. In order to avoid additional geometric corrections, no optical lens were used to focus the laser beam. The construction of the optical detector array was completed in house at the Center for Coast and Ocean Mapping using cost-effective components, such as 80-20 aluminum and Delrin. The total cost of the optical detector array along with its support structure was near $3000. An outline of the components, assembly, and calibration of the array may be found in Appendix B.

To measure the laser beam footprint in the water column after it refracted through the air-water interface, the detector array was oriented to face vertically upwards. The array was positioned at a depth of 0.25 m below the water surface to avoid interacting the waves (deep water condition, equation 3.2), as well as to minimize the laser beam scattering and absorption. At this depth, the water surface contributions to the laser beam can be separated from scattering and absorption effects on the beam footprint to a certain degree. A laser beam with a 0.2 m diameter footprint on

the water surface was projected at the array from a height of ~3m above the water surface. This setup allowed the laser footprint to be imaged in a variety of laboratory simulated sea states (Figure 4.7). A combination of a wave paddle and a fan was used at different times to generate waves of different height and wavelength.

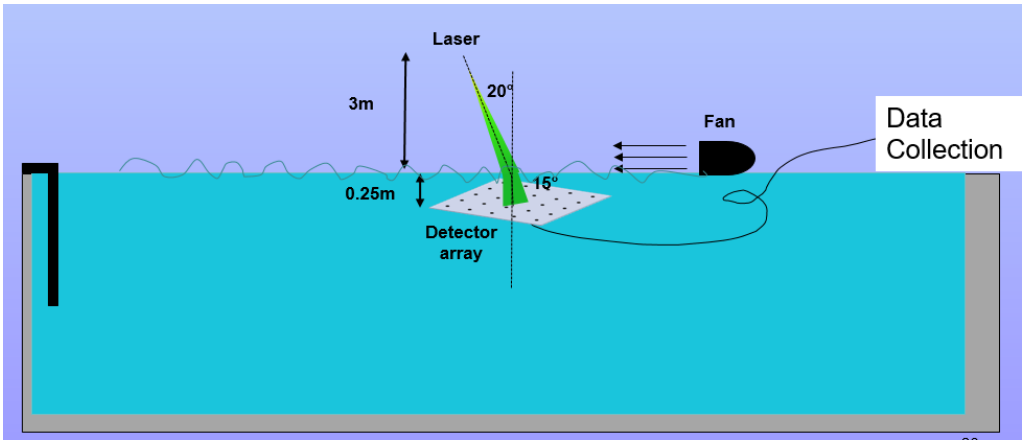

Figure 4.7: Experimental setup in the Chase Ocean Engineering Wave and Tow Tank, used for angle of incidence estimation.

Previous studies only used computers models, whereas this study makes use of the detector array to physically measure the spatial distribution of the laser beam energy. In the experiments, the effects of surface waves on the shape of the footprint could be compared to the footprint refracted through a flat water surface. Through calibration, the detector array was also found to be sensitive to shifts in the incident angle of the laser beam on the array down to 0.1° increments. The use of the detector array allowed the refracted beam path to be measured and compared to a still water case. The data collected from the underwater detector array was analyzed as an image with 36 pixels where the value of each pixel corresponds to laser beam intensity at that point (Figure 4.8).

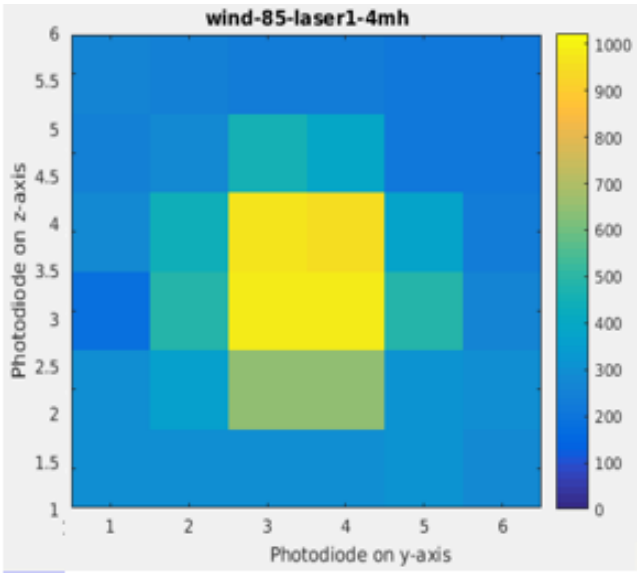

Figure 4.8: Example of raw pixel bit value related to the intensity of the laser beam. This image show the footprint of the 20cm diameter laser beam just below a still surface.

Image processing techniques such as centroid calculations and image moment invariants were used to extract information from each frame. These techniques help to derive beam calculations in sub-pixel accuracy and provide additional spatial information. Image moments provide information on the spatial weighting of pixel intensities in the image. The image moments are calculated as follows:

$$M_{pq} = \frac{1}{S}\sum_{i,j}(y_i - y_0)^p \left(x_j - x_0\right)^q I_{i,j}, \tag{4.2}$$

$$\text{Where} \qquad S = \sum_{i,j} I_{i,j} \tag{4.3}$$

For p and q= 1,2,3, and i and j=1-6 (number of pixels on each axis) are the pixel indices. $I_{i,j}$ is the intensity at each pixel and S is the summation of the intensities of all the pixels. y_0 and x_0 are the index locations of the pixel of maximum intensity and y_i and x_j represent the index for each pixel. Each image has 9 image moments that were calculated and used to form a 3X3 image moment matrix for analysis.

The image processing calculations are detailed further in this section and in Appendix D. The two most important physical properties that can be extracted using image processing techniques are the refraction angle of the beam (effects the slant path through the water column) and changes to the Gaussian beam distribution such as skewing of the beam.

4.3 Experimental Setup and Incident Angle Calibration

The experimental setup included a large industrial fan that was mounted 0.3 m above the water surface and generated wind speeds near 4 m/s (Figure 4.9 a.) that produced small random capillary gravity-capillary waves. As mentioned earlier in the previous section, the detector array was placed close to the water surface in order to exclude contributions from scattering and absorption of light in the water column. The depth of 0.25 m below the water surface was calculated based on the deep-water wave conditions (equation 3.2) using the expected maximum wavelength of 0.1 m. A 5 mW continuous wave laser pointer with a plano-concave 75 mm focal length lens was mounted vertically to the tow carriage at a height of 3 m. As a result, the diameter of the beam on the surface of the water was 0.2 m. Laser beam footprint data was collected at distances of 3.5 m to 8.5 m downwind from the fan in 1 m increments to examine different water surface conditions. The in air incidence angle of the laser was varied from 0°-20° in 5° increments. These laser beam footprints could then be compared to still water surface beam footprints in order to quantify the effects of the surface waves.

The water surface elevation (point measurement) was measured over time using an Ocean Sensor Systems Wave Staff OSSI-010-002. The wave staff data was used to calculate the wave

spectrum at the different fetches or distances from the fan. At each distance, a 5-minute wave sample was gathered for wave analysis.

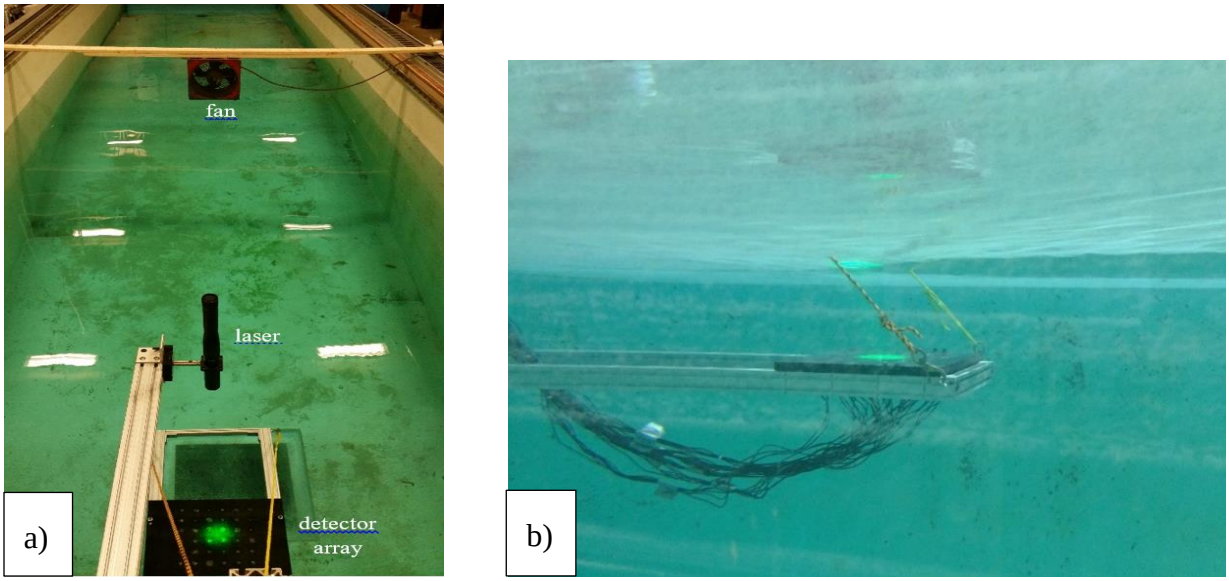

Figure 4.9: Disturbed water surface experiments. a) The fan generates surface waves that interact with the laser beam that is projected on the array. b) A subsurface view of a turbulent laser beam on the array.

It is important to note that the detector array was calibrated in order to measure the refracted angle of the laser beam below the water surface. In this calibration, a correlation between the images collected by the detector array and the laser's angle of incidence in the experimental configuration was found using inverse moment invariant algorithms. Once a trend was defined, an equation that shows the relationship between the angle of incidence and the image moment value could be derived. This calibration equation can then be used to infer the laser beam incidence angle for a wind-driven water surface. For the incidence angle calibration, an experimental setup depicted in Figure 4.10 was conducted at UNH's Chase Ocean Engineering Wave and Tow Tank. Data was collected over a flat still water surface at in air incidence angles ranging from 0-30° in 1^0 increments. For each angle, the geometry of the laser in the horizontal direction was adjusted in order to allow the center of the beam to strike the center of the array.

These shifts were less than 0.1 m and did not noticeably change the laser beam footprint diameter. For each configuration 400 frames (i.e. 20 seconds of data at 20 Hz) were collected at each setup.

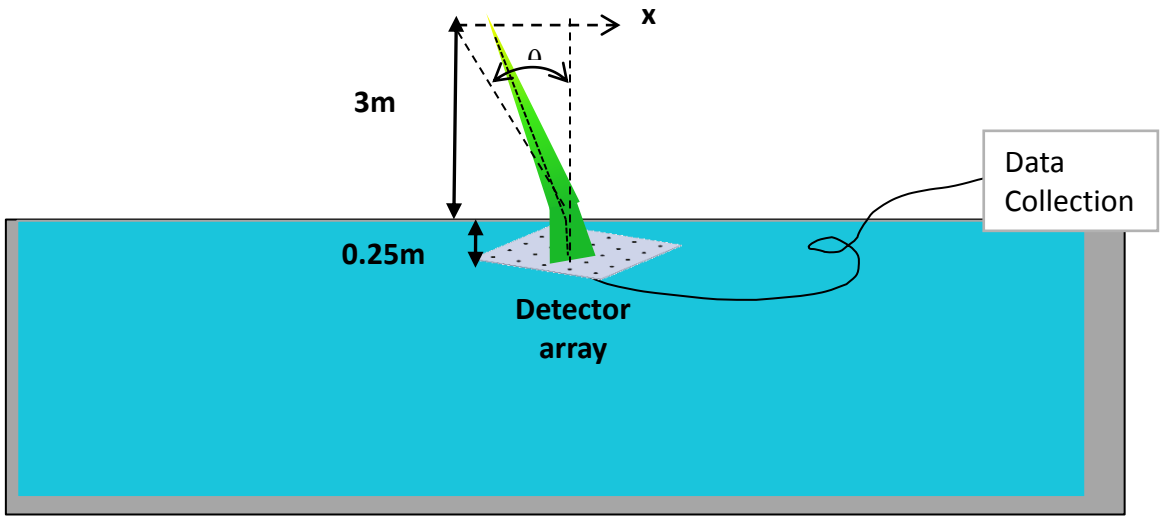

Figure 4.10: Incidence angle calibration setup. The laser was moved horizontally along x with changing angle θ to provide the correct angle of incidence on the water surface. The refraction angle was then calculated for use with array calibration.

For each calibration point, the time averaged moment matrix values (calculations are provided in Appendix D) were calculated. The nine moment matrix values were compared against incident angle in an effort to find a correlation between the physical angular shift and the moments. The calibration results showed that the M_{13} value correlates well with the laser beam angle of incidence (Figure 4.11). A linear least squares trend line was applied to the M_{13} data (Figure 4.12) and can be used to calculate the angle of incidence from any image provided by the detector array.

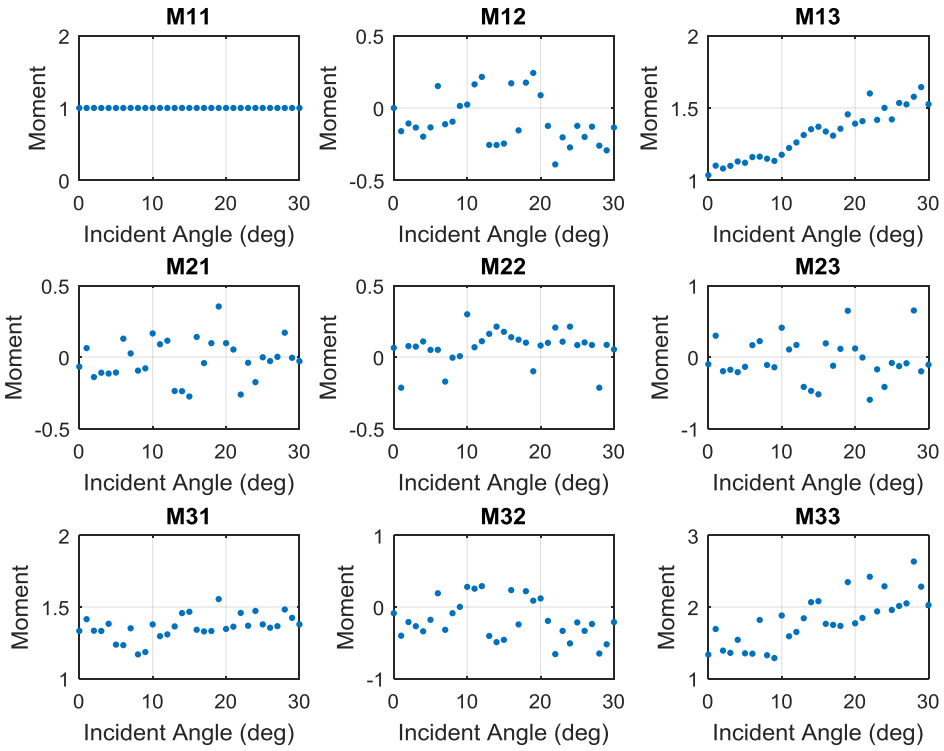

Figure 4.11: Image moment values versus the incident angle. M13 shows a strong correlation.

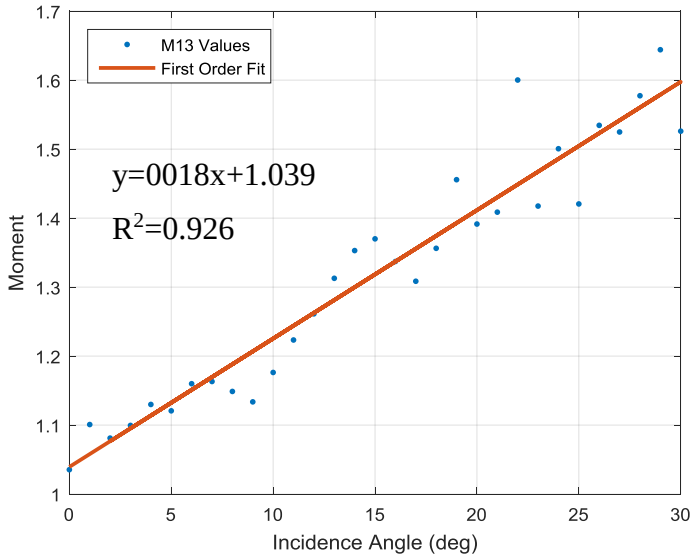

Figure 4.12: The calibration curve for the M13 vs. incidence angle. This correlation provides the in air estimation of incidence angle for any unknown footprint.

5. RESULTS

5.1 Wind Wave Measurements

The wind velocity output of the larger fan mounted over the tank was recorded as a function of distance from the fan's exhaust using a handheld Digital Tools Mini Anemometer (Figure 5.1). It was observed that the fan's wind velocity output decreases proportional to the distance from the fan, *r* (i.e., $U \propto r^{-1}$), indicating spherical spreading of the fans exhaust. As such, surface waves produced in the wave tank will depend on the distance from the fan (fetch) as well as the approximate wind speed at that distance.

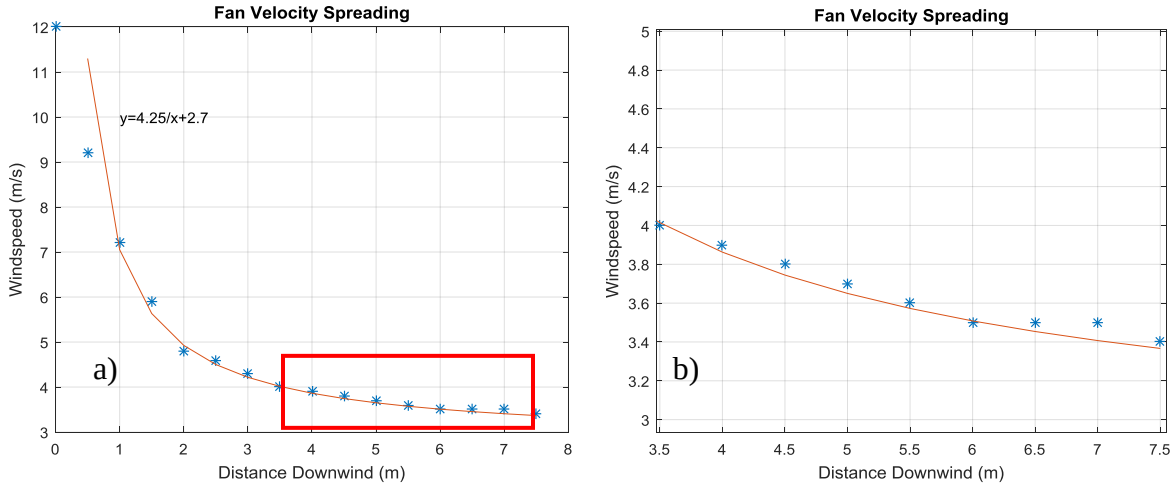

Figure 5.1: a) The velocity output of the l fan is seen to have spherical spreading (∝ r -2) with distance downwind. b) Over the range of distances studied, the fan output changes by less than 1m/s.

A capacitive wave staff (Ocean Sensor Systems OSSI-010-002) measured the water surface height at a 30Hz sampling rate with millimeter water height accuracy. Figure 5.2 provides a sample of the water surface elevation during the fan operating. The observed waves contained amplitudes on the order of several millimeters with periods less than 1 second.

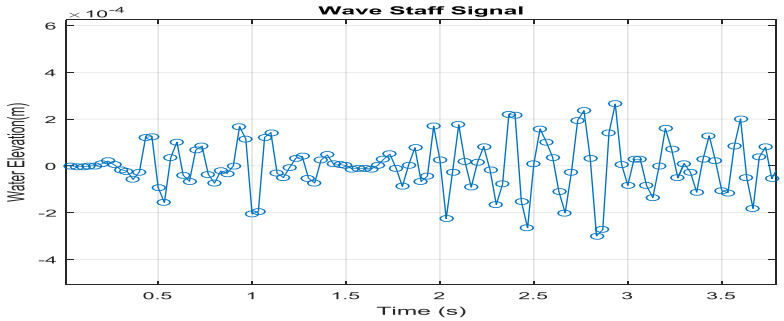

Figure 5.2: Water surface elevation at 3.5m from fan.

In order to classify the spectral content of waves present at each location in the tank, the wave elevation data was collected at downwind distances from the fan ranging from 3.5 m to 8.5 m at 1 m increments. The measurement duration of the wave height data was 5 minutes at each distance in order to capture a significant number of wave crests (more than 100) for statistical analysis. The wave spectrum was calculated and compared to the Apel (1994) spectrum using a similar fetch and wind speed observed in the empirical experiments (Figure 5.3). The peak frequency tends to decrease as distance from the fan increases, indicating the waves grow longer with fetch for both the tank data and the model.

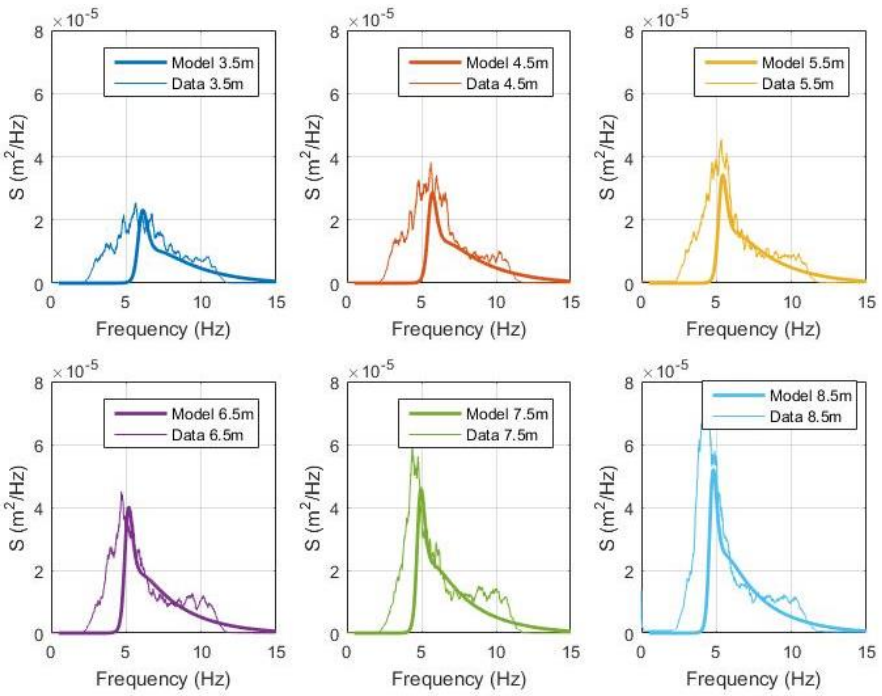

Figure 5.3: The wave spectrum and Apel model spectrum for each distance from the fan. Wind speed measured with the anemometer was used for the spectrum model.

The frequency content in the 6-10 Hz range appears to remain relatively constant over the range of distances (Figure 5.4), indicating that capillary waves with very small amplitude and high frequency content are present in all cases. The small shoulder seen in the 9-10 Hz region of the wave staff data may be due to noise in the signal as approaches the lower limit of the sensors measurement range. The changes in wave

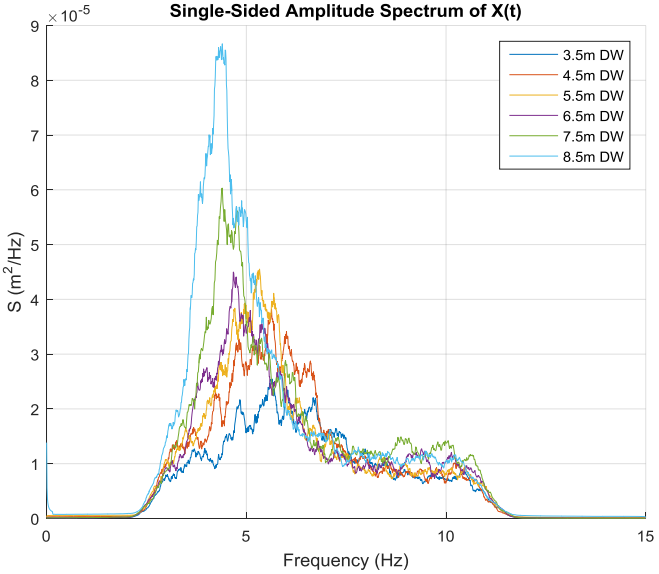

spectrum can also be visualized as it changes over downwind distance. In addition, the dominant wave peak decreases in frequency and grows in amplitude as the distance further away from the fan. Table 5.1 provides the peak frequency and significant wave heights for each dataset. The peak frequency decreases with distance while the significant wave height first increases then levels off at 0.009 m.

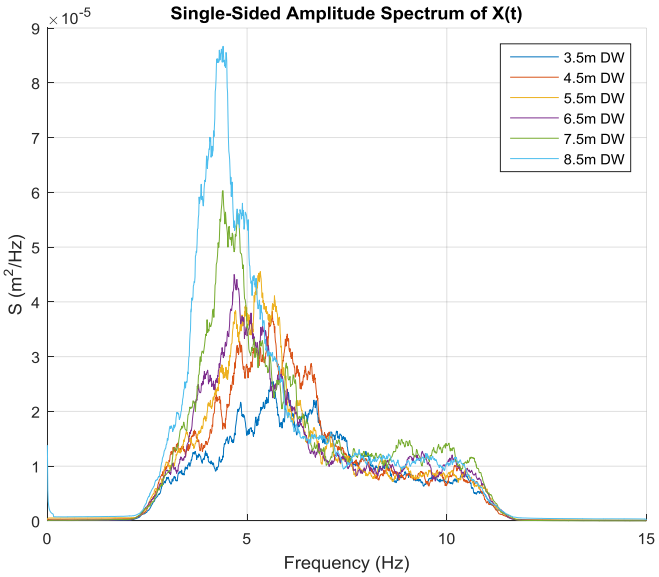

Figure 5.4: Wave spectrum at each distance downwind. The frequency contend in the 6-10 Hz range is similar in each case.

Distance Downwind (m)	**3.5**	**4.5**	**5.5**	**6.5**	**7.5**	**8.5**
Peak Frequency (Hz)	5.6	5.5	5.3	4.6	4.4	4.3
Peak Wavelength (m)	0.050	0.051	0.055	0.074	0.080	0.085
Significant Wave Height (m)	0.008	0.010	0.011	0.009	0.009	0.009

Table 5.1: Spectrum peak and significant wave height for wind ripples present in lab experiments.

In order to relate the wave conditions in the laboratory settings to a real-world gravity-capillary wave conditions, a model of a fully-developed Apel (1994) wave spectrum was fitted to the observed wave staff data. According to Zhang (1995), small waves in the capillary and gravity-

capillary regime are fully developed by a fetch of 30m. Accordingly, an Apel wave spectrum with a fetch of 30 m was fitted to the laboratory spectrum by adjusting the wind speed until a best fit was found. Each experimental wave tank spectrum represents a realistic developed sea state in the gravity-capillary regime for the given wind speed (Figure 5.5). It is assumed that measuring beam footprints at the downwind locations from the fan is a good approximation of real world survey results for the related wind speed.

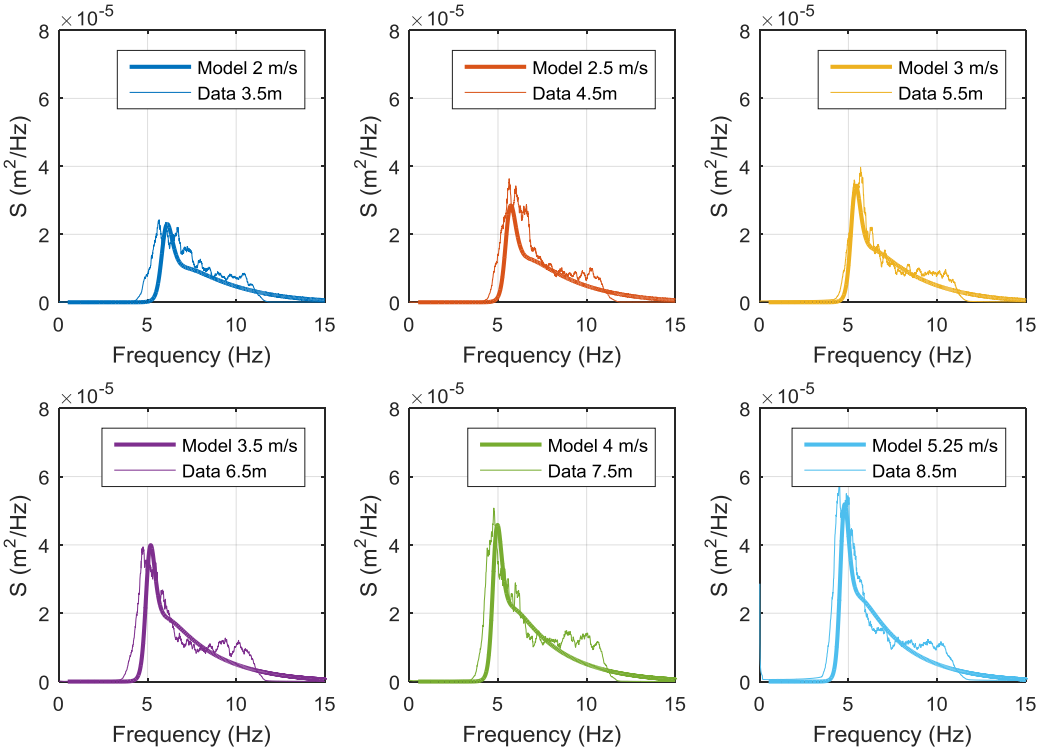

Figure 5.5: Experimental spectrum matched to fully developed gravity-capillary Apel 1994 (fetch of 30m) wave spectrum.

The goodness of fit for each model curve was used to find the wind speed value that best matches the data. Based on an assumption of linear correlation between the data collected using the wave staff and the calculated models, a R^2 correlation value was calculated (Table 5.2). The model wind speed was adjusted until R^2 value was maximized for each case. As a result, wave spectrum at

each downwind distance approximate real world survey conditions using ambient wind speed, U_{10} (typically, measured 10 meters above the water surface). Table 5.2 provides the relationship between the downwind location in the Wave Tank and survey conditions. These results will be used to define simulation parameters as well as to relate uncertainty values measured in laboratory settings to uncertainty values observed in field data collection.

Distance from Fan (m)	**3.5**	**4.5**	**5.5**	**6.5**	**7.5**	**8.5**
Survey Wind Speed U10 (m/s)	2	2.5	3	3.5	4	5.25
R^2	0.64	0.74	0.76	0.73	0.82	0.87

Table 5.2: Fan generated tank conditions and the estimated real world survey wind conditions.

5.2 Ray Tracing Results

The Monte Carlo ray-tracing simulation outlined in section 4.1, was conducted for laser beam incidence angles ranging from 0°-20° in 5° increments. The wind velocities in the simulations ranged from 2-5 m/s in 0.5 m/s steps. Beam centroids were calculated and converted to refraction angle deviations from the still water assumption. For significant statistical analysis, over the 500 iterations performed. The results of the ray-tracing simulation indicate that in the along-wind direction (axis parallel to direction of wind) the beam refraction angle deviation increases nearly linearly with wind speed (Figure 5.6). The along-wind refraction angle deviation also appears to increase with incidence angle for all wind speed cases. The refraction angle deviation in the cross-wind direction (axis perpendicular to wind direction) has much less correlation with wind speed, although there is a decrease as the beam incidence angle increases.

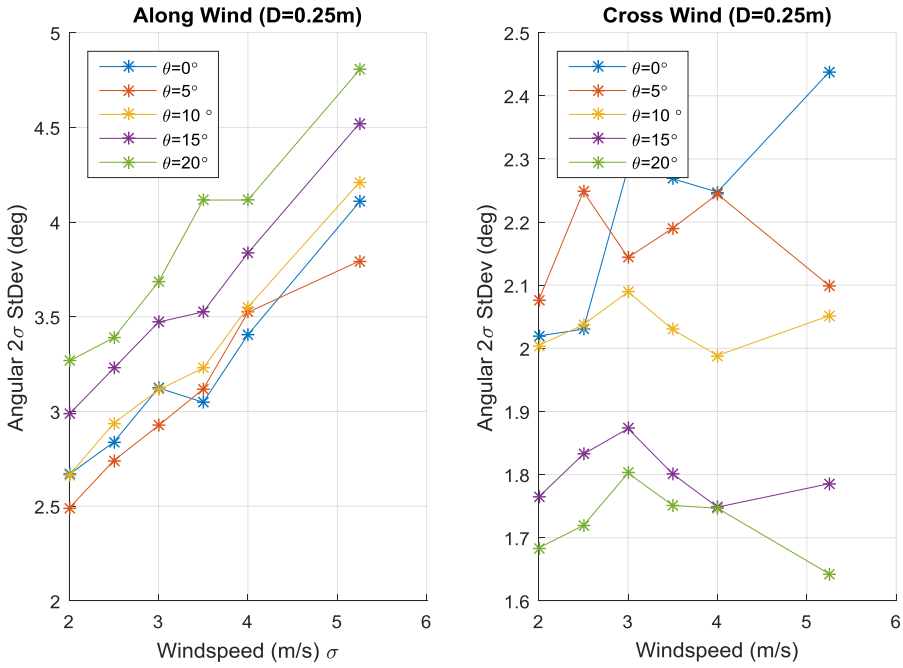

Figure 5.6: The standard deviation values in the along wind direction from each simulation comparing incidence angle and wind speed. The beam diameter for all simulations was D= 0.25m.

The incidence angle results were averaged in order to examine the effects of wind speed on the wave refraction uncertainty. The simulation results showed that both the along wind and cross wind refraction angle deviation is related to wind speed (Figure 5.7). A linear fit was performed on the along wind deviation values to determine a slope of 0.46° per m/s. The cross wind refraction angle deviation increases at a much slower rate due to wind speed. The slope for cross wind fit line was found to be 0.02° per m/s. These results indicate that for typical survey conditions the refraction angle may deviate from the still water assumption by 2°and 3°- 4.5° in the cross wind direction and in the along wind direction, respectively.

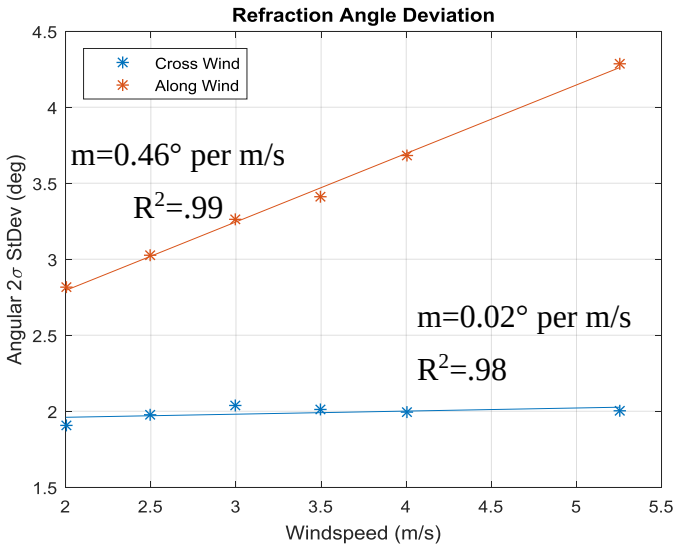

Figure 5.7: Refraction angle deviation averaged over incidence angle (D=0.25m).

Then the effects of the incidence angle on the wave refraction uncertainty were evaluated. The results in Figure 5.7 indicate a relationship between the incidence angle and the refraction angle deviation in the along and cross wind directions. This relationship was further investigated by running simulations with a constant wind speed of 2.5 m/s while changing the incidence angle from 0° to 20° in 5° increments (Figure 5.8). The results show that the along-wind deviation of the refracted angle calculations increases as the beam's incidence angle increases, while the cross-wind deviation of the refracted angle calculations decreases.

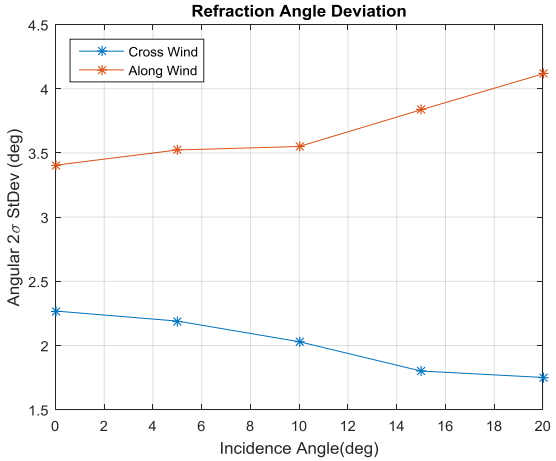

Figure 5.8: For U=2.5 m/s and D=0.25m, the relationship between beam refraction error and still water incidence angle.

These results indicate that ALB systems with circular or elliptical scanning patters (θ_a between 15°-20°) will have different wave refraction error than systems with rectilinear scanning that has more near nadir pulses.

Finally, simulations were conducted using different beam footprint diameters on the water surface ranging from 0.25 m to 4 m. It has been shown by Karlsson (2011) that the wave refraction error decreased for larger diameter beams interacting with larger gravity waves. The simulation results in this study showed similar observations over a water surface containing small capillary and capillary-gravity waves.

Figure 5.9 provides the refraction angle deviations versus wind speed for a number of beam diameters. Larger diameter beams clearly show less refraction angle deviation due to small surface ripples.

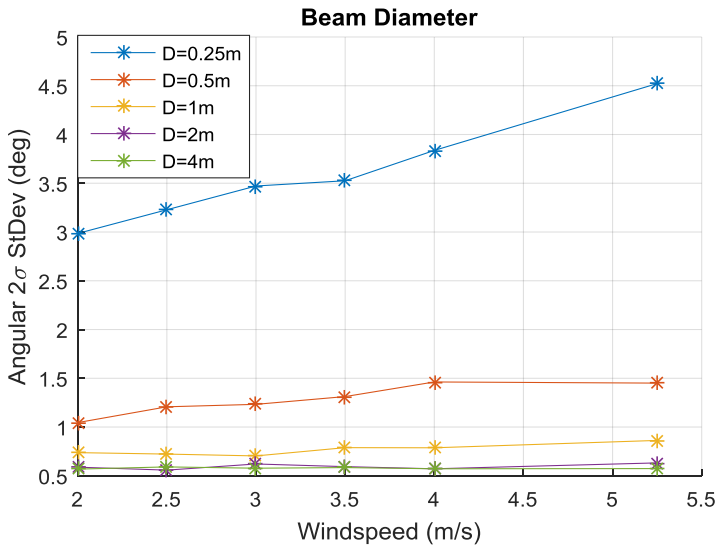

Figure 5.9: θ=15° for all simulations. The larger diameter beams are effected less by the surface ripples than beams with diameters less than 1m.

Additional simulations were performed for a range of incidence angles (0°-20°) and wind speeds (2-5.25 m/s) and with varied beam diameters. The results were averaged for incidence angle and wind speed to examine the effect of beam diameter (Figure 5.10). Refraction angle deviations for both the along-wind and cross-wind show an exponential decay for larger beam diameters. While smaller beams allow higher resolution spatial observations, there is a higher probability of refraction angle deviation from the still water assumption that will shift the center of beam concentration with an error in the reported position of the bottom measurement.

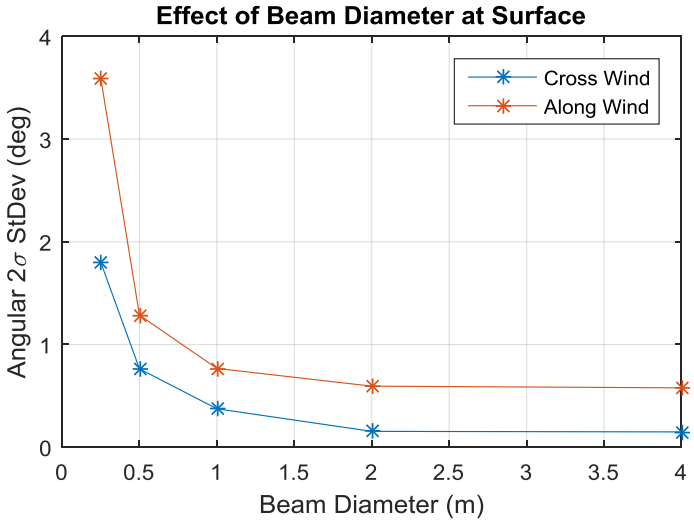

Figure 5.10: The surface error decays exponentially with laser beam diameter.

A variety of beam diameters are used by commercial ALB systems use in order to achieve different survey requirements including depth penetration, data density, and object detection. Larger beam footprints above 1m in diameter show less refraction angle deviation due to small surface waves. Larger beams may have an averaging effect were the total number of wave crests is great enough that the majority of laser energy is still refracted along the direction predicted by the still water assumption.

5.3 Detector Array Results

Following the experimental procedures outlined in section 4.3, the detector array collected images of the laser beam footprint for a variety of water surface conditions (wind speeds, beam incidence angles). The photodiodes logged light intensity in a 10-bit dynamic range (0-1023). Although it is possible to convert the photodiode bit values to a power measurement in Watts using a calibration curve found in Appendix C (responsivity), the image moment calculations were conducted using the bit values. Figure 5.11 provides an example a beam footprint at nadir incidence angle at smooth level water surface conditions. The footprint is near circular with an intensity distribution that follows the Gaussian approximation. This nadir angle footprint case is also used as the control measurement to different experimental settings investigated in the study. By comparing different footprint results to the control measurement it is possible to examine the effects of the waves.

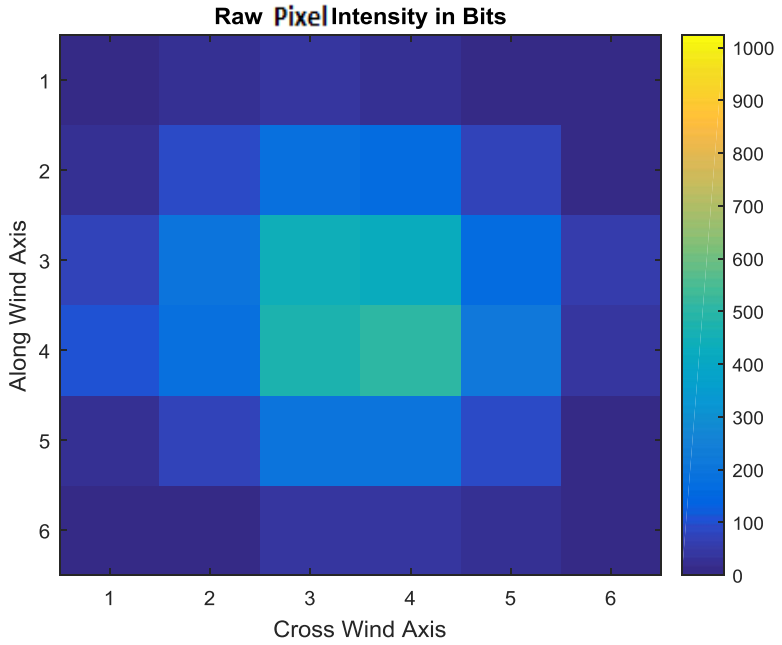

Figure 5.11: θ=0°, still water surface. Near Gaussian intensity distribution. Pixels are labeled on X and Y axis.

Figure 5.12 provides a still water footprint of the laser beam at an incidence angle of 20°. The geometric stretch of the beam is visible when compared to Figure 5.11. The full width half max (FWHM) of the nadir beam is approximately 0.2 m while the 20° beam is about 0.205 m in the axis parallel the off nadir angle.

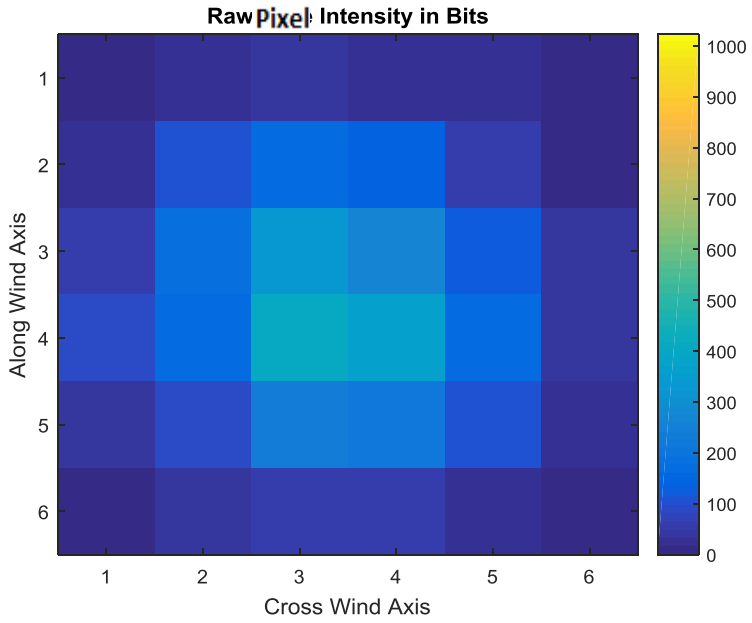

Figure 5.12: θ=20°, still water surface. At higher incidence angle a more elliptic beam shape. Pixels are labeled on X and Y axis.

When the wind-driven surface ripples were introduced to the experimental settings, the shape of the laser footprint was significantly altered. In the still water case, it was possible to use simple circle or ellipse shapes to represent a constant intensity along the footprint. Once the ripples were introduced, the beam footprint became much less uniform. In Figure 5.13, it possible to see cases where the frames observe a near elliptical footprint (frame *b* and *d*) and cases when the footprint shape becomes irregular in its distribution and the beam cannot be approximated using a Gaussian energy distribution (frames *a* and *c*).

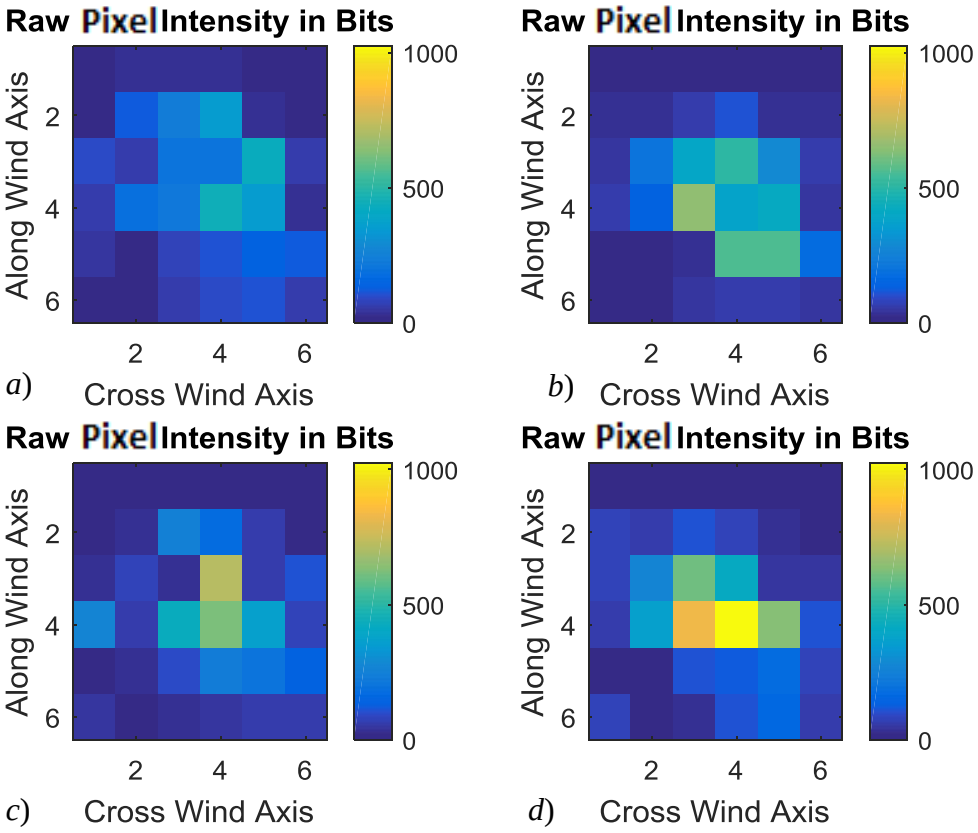

Figure 5.13: θ=0°, U=2m/s. A sample of detector array intensity readings in a disturbed surface case.

Water surface ripples also cause fluctuations in the peak intensity within the beam footprint. It was possible to also identify in the study results a focusing or defocusing effect caused by the small waves on the beam footprint depending on the surface geometry. Figure 5.14 provides examples of this lens focusing effect the surface may have on the beam. Frames *a* and *c* show a footprint with lower intensity (defocusing) while frames *b* and *d* have near maximum intensity values (focusing).

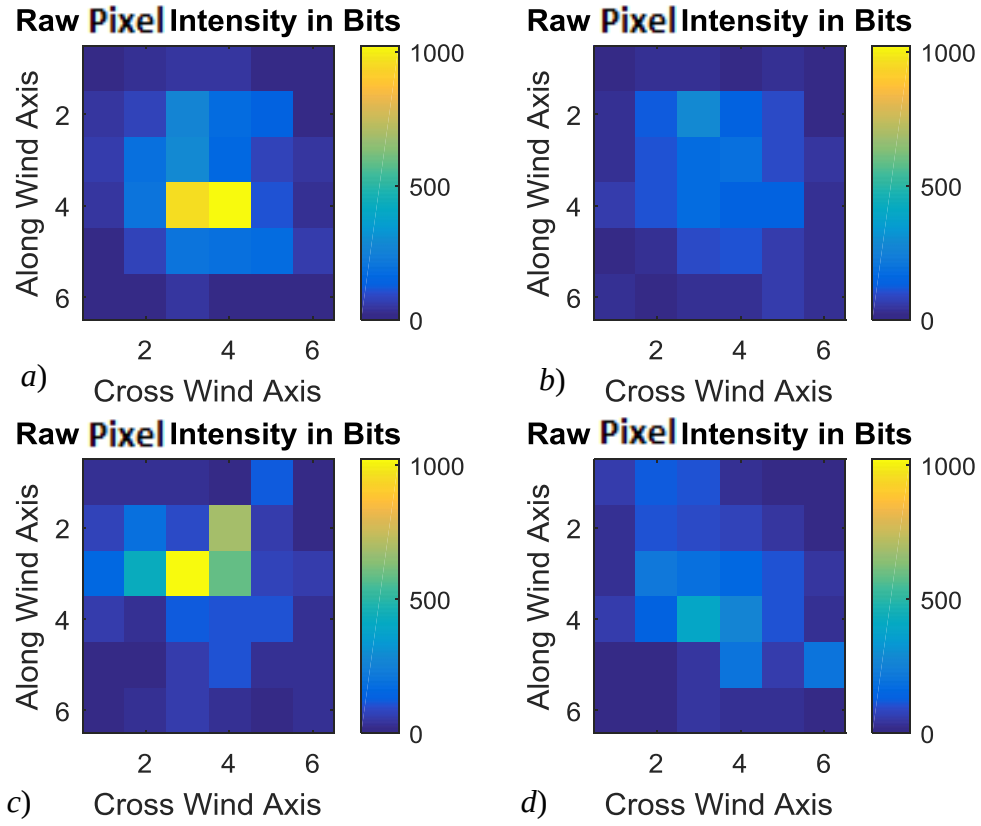

Figure 5.14: θ=20°, U=4m/s. A sample of detector array intensity readings in a disturbed surface case.

In subsequent sections, these 6X6 images will be analyzed to back out information about the contribution from turbulent water surface conditions on the laser beam as it enters the water. In particular, any refraction angle deviations from the still water case caused by wind ripples will be investigated in order to measure the uncertainty of ALB range measurements in varied wind-water conditions.

5.4 Sub Surface Refraction Angle Deviation

The optical detector was used to measure the refraction angle deviation from the still water case using the image moment invariant algorithms and a calibration curve calculated according to Section 4.2. The M_{13} moment invariant values were calculated for each of the 400 frames in the datasets. The moment values where then related to the estimated refraction angle using the calibration curves (Section 4.3). For every experimental frame that was sampled at 20 Hz, the effective beam refraction angle was calculated and plotted over time. Occasionally, outliers of the M_{13} moment values was significantly outside of the range of the calibration curve, i.e., moment values more than 0.25 from the trend line value. These outlier values were discarded due to the fact that the moment-angle relations may not be linear outside of the region that was calibrated. The datasets collected with a still water incidence angle of 0° and 5° were also discarded due to their close proximity to the edges of the calibration curve that produced unrealistic incidence angle estimations beyond 60°.

Figure 5.15 provides examples of the fluctuating refraction angle calculated from the calibration curves. The mean of the angles is typically quite close to the incidence angle predicted by the still water assumption. The standard deviation values fluctuate around 4° from the still water assumption for the data sets. These large standard deviation values suggest that there significant wave refraction error due to the presence of capillary and gravity-capillary ranges. The mean of the refraction angles is very close to the still water assumption, indicating that there is not constant offset due to the surface waves.

This dataset (Figure 5.15) provides the refraction angle estimations as a function of time. The beam appears to undergo a significant amout of deviation up to 5° from the still water incidence angle.

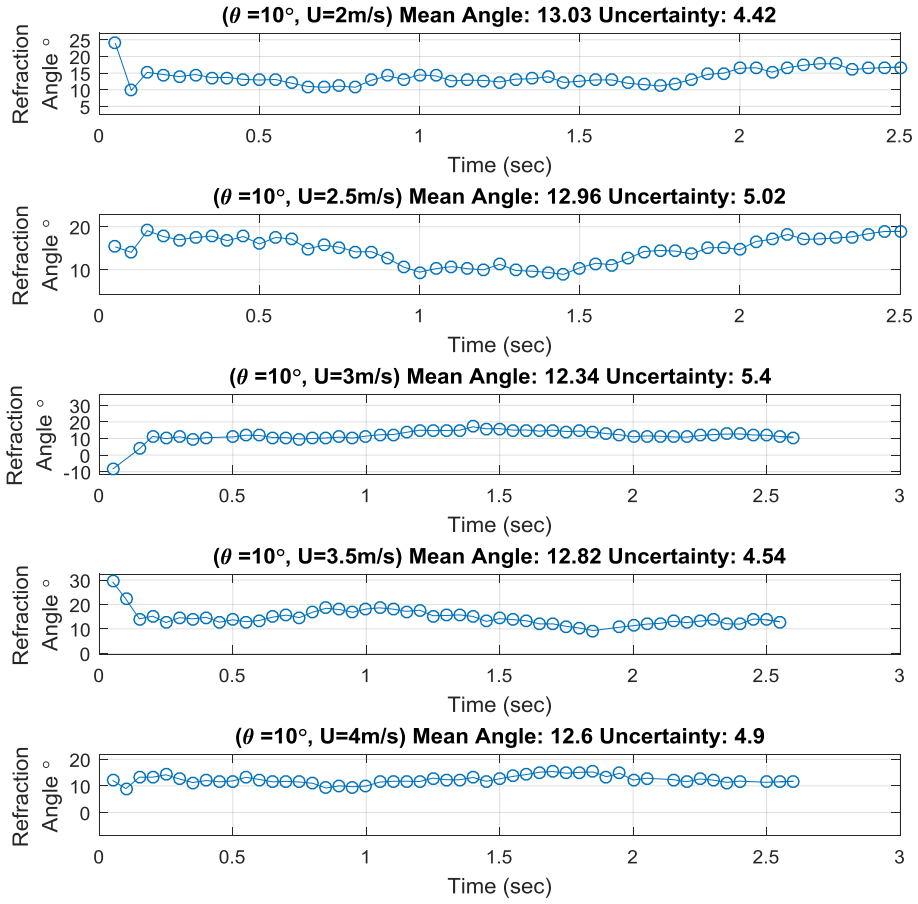

Figure 5.15: Short samples of sub surface estimated incidence angle curves at a 10° still water incidence.

The 2σ standard deviation of the refraction angle deviations were calculated for each case (U=2-5.25 m/s, θ=0-20^0) and the results are presented in Table 5.3. The standard deviation is the uncertainty of the beam path after it has undergone refraction through the wind driven water surface.

Incidence angle ° → Wind speed (m/s) ↓	10	15	20
2	4.42°	4.7°	4.62°
2.5	5.0°	5.28°	5.08°
3	5.4°	4.78°	4.6°
3.5	4.54°	4.46°	4.88°
4	4.9°	4.94°	4.86°
5.25	4.9°	5.0°	4.97°

Table 5.3: 2σ Refraction angle deviations (°) from the image moment calculations.

The results from the image moment calibration rely on the accuracy of the calibration curve and only report the refraction angle deviations in the along-wind direction. Two data sets from the experimental results were too close to the edge of the calibration curve and were not used in the final analysis. However, it important to note that the image results only provides a one dimensional refraction angle deviation rather than giving an offset in the along-wind and cross-wind directions. For these reasons, additional image processing techniques were implemented to gather high resolution results of the refraction angle deviation and are detailed in the next section.

5.5 Beam Footprint Analysis

In order to further analyze the effect of the surface ripples on wave refraction uncertianty, the beam footprint images were investigated using image processing techniques that include centroid analysis, intensity contouring, and Gaussian modeling. For each distinct water surface case generated in the wave tank, 400 frames were recorded using the optical detector array. The frames were individually studied to look at the beam width as well as the shifts of the center of concentration of the beam footprint (wave refraction error).

First a centroid analysis was performed to study the refraction angle uncertianty due to the wind waves. The centroid of each frame was calculated using the image moments and compared to the still water beam center (see Appendix D for a discription of the centroid method). Figure 5.16 presents the results of the centroid analysis for a smooth undusturbed surface and different disturbed water cases at different distances from the fan. These results are for the nadir case with a 0° incidence angle of the laser on the water. Most notibly there is an order of magnitude increase in the standard deviation of the 400 beam centers from the still water case to the wind driven cases. The beam center was seen to fluxuate slightly more in the along wind direction than in the across wind direction. This is likely due to the amount ofwave spreading that generates slope deviations both in the along and across wind directions. The standard deviation of the beam center for the wind driven cases is around ±0.02m with a total range of nearly ±0.04m in both the along and cross wind directions.

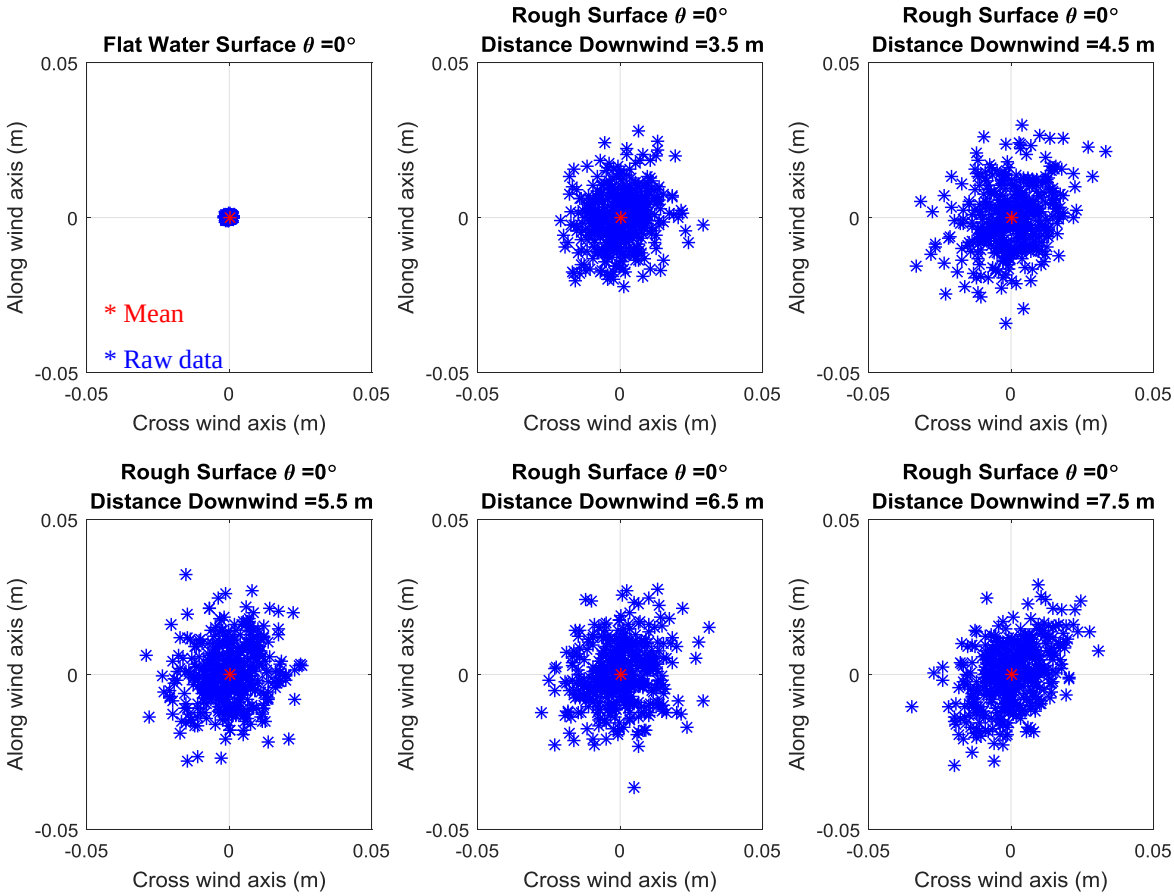

Figure 5.16: The centroid results at distances of 3.5 to 7.5 m from the fan at an incidence angle of 0°.

The results for other incidence angle including at 15° (Figure 5.17), (as well as 10°, and 20° in Appendix E) appear similar to the nadir results. A shift of the center of concentration of the beam from the still water location indicates the energy contained in the laser beam was refracted at a different angle than would be predicted by the still water assumption. Since the depth of the array is known (0.25 m), the horizontal shift can be reported as angular offset in the along wind and cross wind directions using simple trigonometric calculations.

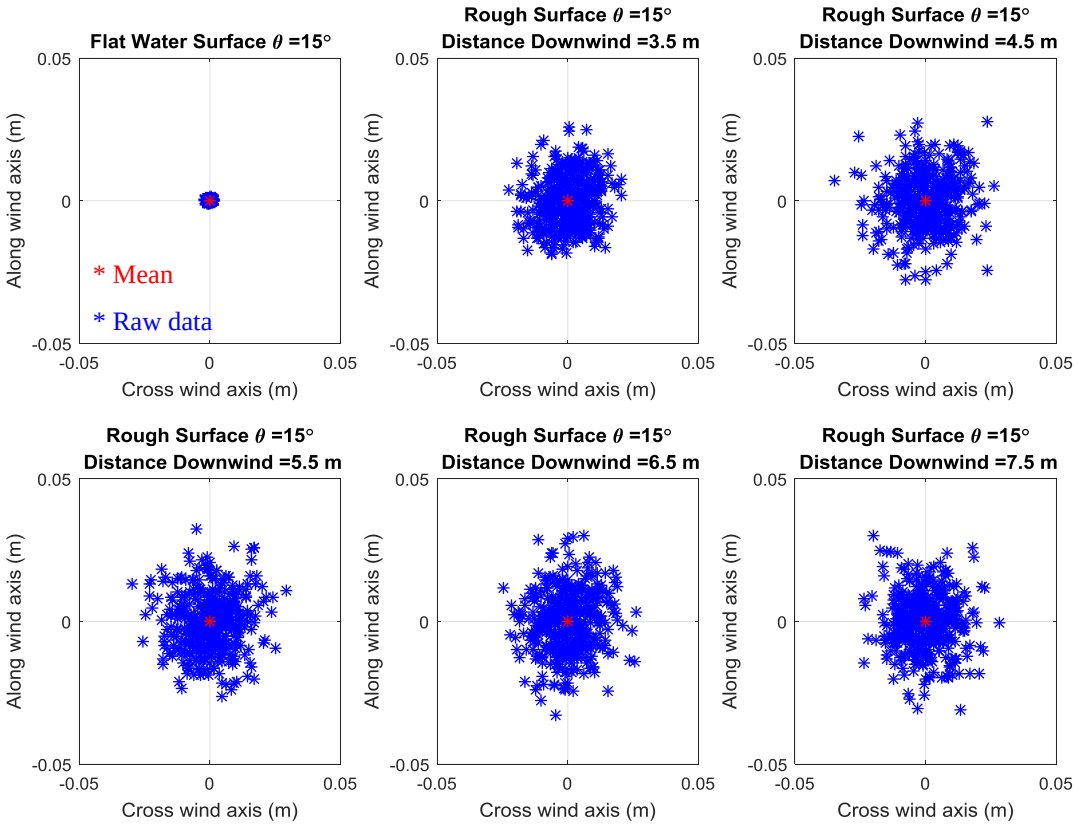

Figure 5.17: The centroid results at distances of 3.5 to 7.5 m from the fan at an incidence angle of 15°.

While the surface ripples clearly introduce a greater deviation in the sub surface beam center it is also of interest if the various simulated wind speeds and incidence angles produced have an effect on the standard deviation of the beam centers. For each of the datasets the standard deviation of the beam center in along wind and cross wind direction was converted to a refraction angle. First the effects of the simulated survey condition wind speed were considered (Figure 5.18). It can be seen that the along wind refraction angle standard deviation grows with wind speed. This indicates that the laser beam slant path deviates more from the still water assumption, as the capillary waves begin to develop into small gravity waves with longer wavelengths. The greater deviation of the refraction angle induces larger uncertainty into the ALB measurement by shifting the location of the beam footprint on the seafloor.

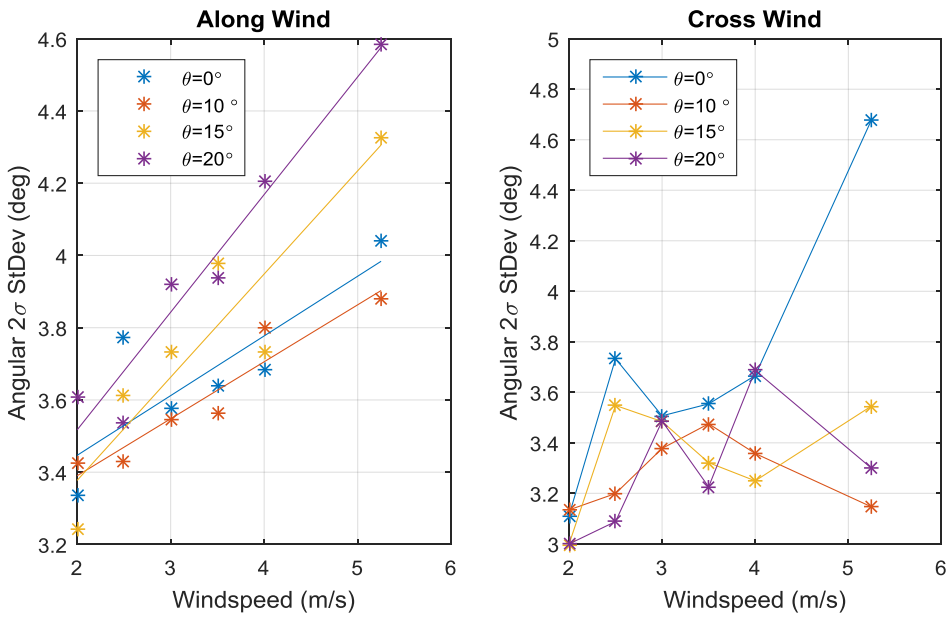

Figure 5.18: Along wind standard deviation of beam center as a function of distance.

For each dataset at specific incidence angle a trend line was fit to examine the growth of the refraction angle deviation with wind speed. Table 5.4 provides the details of the linear fit lines. The results indicate that as the incidence angle of the laser beam on the water increases the rate of refraction angle uncertainty due to wind speed increases. The results indicate that beams that strike the water at higher incidence angle are more will likely have more refraction angle uncertainty than those that strike the water closer to nadir. This will effect ALB systems using circular scanning patterns (larger θ_a values) to a greater degree than those that scan closer to nadir.

Incidence Angle	0°	10°	15°	20°
Slope (° per m/s)	0.16	0.158	0.28	0.32
R^2	0.677	0.910	0.836	0.946

Table 5.4: Trend line values for the beam refraction angle deviation results.

When the results from the previous plots are averaged over incidence angle a clear relationship between survey wind speed and refraction angle uncertianty can be found. Figure 5.19 shows that both the along wind and cross wind standard deviations of the refracton angle increase with survey condition wind speed. There is more uncertainty of the refraction angle in the allong wind direction. For the wind speeds considred in this experiment the relationship between windspeed and refraction angle deviation are well aproximated with a linear fit (both lines have hight goodness of fit values).

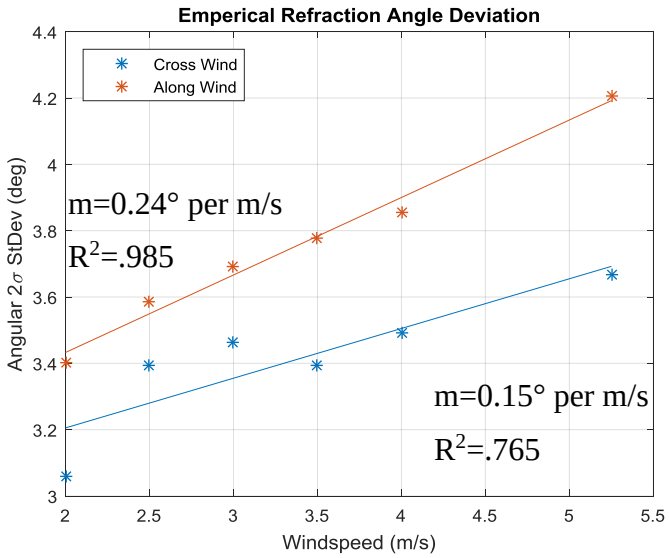

Figure 5.19: The refraction angle deviation is seen to clearly increase with wind speed in both along and cross wind directions.

The slopes of the two trend lines indicate the rate at which the refraction angle uncertainty is increasing with respect to wind speed. The results indicate that the along wind uncertainty increases at a higher rate than that of the cross wind error (0.24° per m/s vs. 0.15° per m/s). This indicates that the direction of the wind as well as wind speed are important parameters to measure during an ALB survey in order to estimate error due to wind driven waves.

The results shown in Figure 5.19 indicate there is less angular deviation in the along wind direction and more deviation in the cross wind direction when compared to the model results in section 5.2. This discrepancy may be due to a different amount of wave spreading that effects the distribution of wave slopes in each direction. The approximated spreading value used in the simulations may have assumed less spreading than was produced in the laboratory. A full wave spreading analysis was not performed to validate this assumption.

The effect of incidence angle on the refraction angle uncertainty was also considered. Figure 5.20 indicates that higher in air incidence angles cause larger refraction angle deviations in the along wind direction and less error in the cross wind direction. The emperical data suggests similar trends with respect to incidence angle as the computer simulaitions discussed in section 5.2. At higher incidence angles the along wind wave refraction uncertianty increases while the cross wind uncertainty decreases with values ranging from 3-4^0 from the still water assumption. For these results the 5° incidence angle data was not properly alligned on the array to perform the centroid analysis and was disregarded.

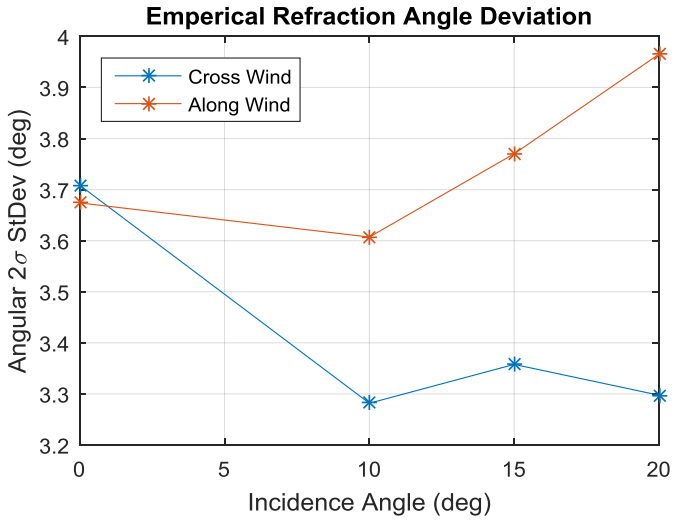

Figure 5.20: The along wind refraction angle deviation increases with incidence angle while the cross wind error decreases.

Finally, Gaussian curves and contour lines were used on the laser beam footprint images in order to examine the changes in beam diameter from the still water assumption. The FWHM diameter was used to calculate the beam expansion in both the along and cross wind directions compared to still water. For the still water cases the beam diameter at the array was calculated be 0.2 m (in both along wind and cross wind axes) for all in air incidence angles (Figure 5.21).

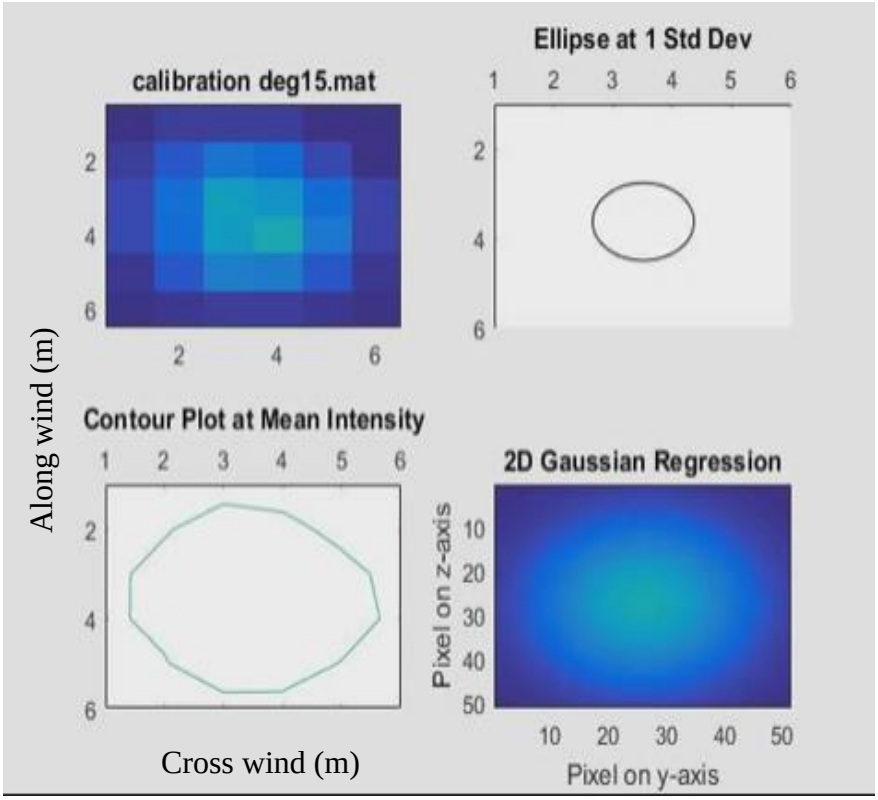

Figure 5.21: Beam footprint analysis for still water case with in air incidence angle of 15°.

The same calculations were performed for images of wave refracted beam footprints. Most of these beams do not approximate a Gaussian energy distribution and the contour line at half of the maximum intensity was to calculate beam diameter (Figure 5.22). Almost all of the footprints were found to show beam defocusing (i.e. increase in beam diameter relative to the still water case). The

mean diameter in the along wind direction was found to be 0.223 m while the mean cross wind diameter was 0.210 m.

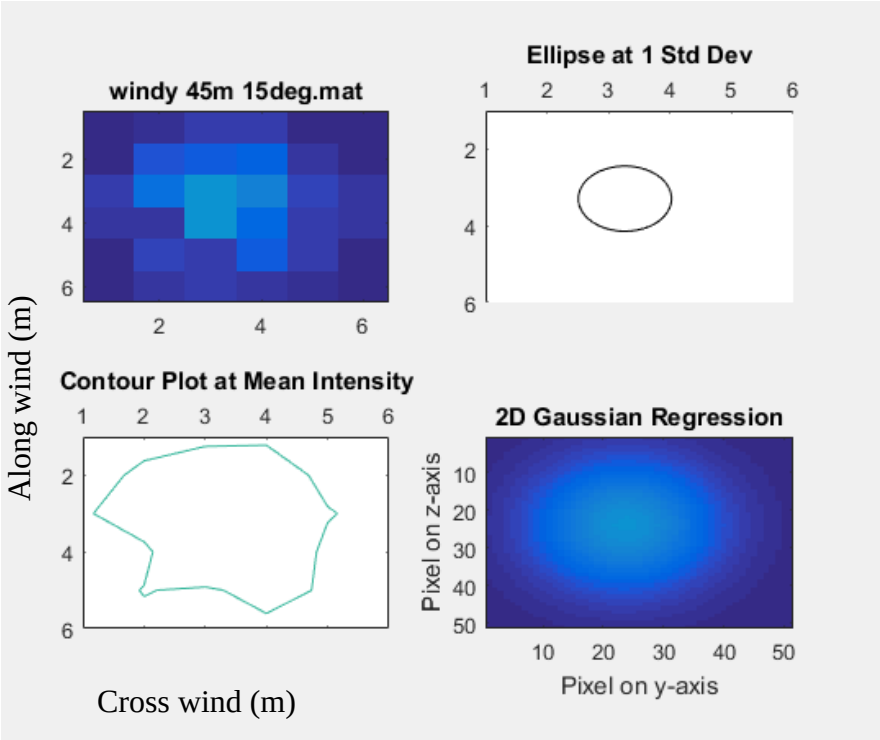

Figure 5.22: Beam footprint analysis for a wave refracted footprint. The contour line is irregular and there is an increase in beam diameter from the still water case.

The results indicate that surface waves generally have a defocusing effect on the laser beam of ~5% in the cross wind direction and ~10% in the along wind direction. This will limit the total depth the ALB system can measure and also changes the expected area illuminated by the beam footprint.

5.6 Uncertainty Model

The results from this study provided empirical data of the 2-sigma standard deviation of the refraction angles in relation to wind speeds and beam geometry on the surface (e.g. in air incidence angle and beam diameter). The 2-sigma refraction angle deviation (95% confidence interval) from the empirical results was used to create look up tables of wave refraction uncertainty that can be used for TPU reporting. Wind wave relationships were investigated in order to model water surface conditions similar to those seen in real world surveys. To make the results of this study applicable in ALB surveys and uncertainty reporting, a refraction angle uncertainty look up table has been produced. This table organizes the refraction angle uncertainty results such that given wind speed and incidence angle of the beam on the water, the uncertainty of the beam path may be interpolated.

It is not currently reasonable to measure and correct for the effects of capillary and gravity-capillary waves using the surface return. Instead the uncertainty due to these small wavelets that are difficult to measure are presented related to basic survey parameters a survey pilot could collect including wind speed and direction as well as system parameters such as beam diameter and still water incidence angle. Table 5.5 and Table 5.6 present the statistical 2-sigma standard deviation values produced from the results. The values reported are for a beam diameter of 0.2m that was used in the experiments. Since the model results of this study agree with Karlsson (2011) that larger beam diameters present less refraction angle uncertainty, an equation was produced to correct for beams of different diameters. The uncertainties tabulated here may be scaled by the correction factor (*CF*) calculated using the following equation to correct for different beam diameters (*D*):

$$for\ 0.2 \leq D \leq 4.5 \qquad CF = 0.0984 * D^{-2.046} + 0.32 \tag{5.1}$$

The equation is derived from the fit line produced in Figure 5.10.

Wind Speed → Incidence Angle ↓	2 m/s	2.5 m/s	3 m/s	3.5 m/s	4 m/s	5 m/s
0°	3.38°	3.46°	3.56°	3.62°	3.72°	3.88°
5°	3.4°	3.48°	3.58°	3.66°	3.74°	3.92°
10°	3.42°	3.5°	3.6°	3.68°	3.78°	3.96°
15°	3.64°	3.78°	3.94°	4.08°	4.24°	4.54°
20°	3.72°	3.88°	4.08°	4.24°	4.4°	4.72°

Table 5.5: Refraction angle uncertainty in along wind axis.

Wind Speed → Incidence Angle ↓	2 m/s	2.5 m/s	3 m/s	3.5 m/s	4 m/s	5 m/s
0°	3.22°	3.28°	3.36°	3.44°	3.52°	3.66°
5°	3.2°	3.28°	3.36°	3.44°	3.52°	3.66°
10°	3.2°	3.28°	3.36°	3.44°	3.52°	3.66°
15°	3.2°	3.28°	3.36°	3.44°	3.52°	3.66°
20°	3.2°	3.28°	3.36°	3.44°	3.52°	3.68°

Table 5.6: Refraction angle uncertainty in cross wind axis.

6. DISCUSSION

6.1 Uncertainty Model

The uncertainty model presented in section 5.6 is derived using the still water incidence angle, wind parameters, and beam diameter at the surface. The wave refraction uncertainty results are 3°-5° from the still water assumption. The wave refraction uncertainty for short wavelengths may be used to improve ALB TPU calculations for better data processing and evaluation. Comprehensive TPU reporting may also improve the IHO classification of ALB data (IHO, 2008) for incorporation into nautical charts.

Compared to other sources of uncertainty for ALB range measurements, it is clear that the wave refraction error is a significant portion of the error budget, especially when considering that the measurement error grows with depth (Table 6.1). Sources of uncertainty to consider include: components of the ALB and the aerial unit, the atmosphere, the water surface, water column, and seafloor. Generally, the aerial uncertainty is due small errors in the boresight calibration of the ALB (lever arms, and offsets) σ_{ALB}, and the accuracy of the positioning unit σ_{GPS} (May & Toth, 2007). The effects of the atmosphere σ_{atm}, are assumed to be several orders of magnitude smaller than other sources and are ignored. Scattering in the water column $\sigma_{scattering}$ has a much greater effect on the extinction depth of the system rather than the uncertainty of the laser path in the water column, and the horizontal and vertical uncertainty is assumed to be minimal for this mode. However, the geometric stretch of the laser beam (section 2.2) on the water surface and at the seafloor introduces uncertainty due to the off nadir angle of the beam and the slope of the seafloor $\sigma_{stretch}$. Vertical uncertainty due to geometric stretch may range up to 1 m depending on beam angle and seafloor slope (Bouhdaoui, 2014). Finally, the uncertainty due to the seafloor $\sigma_{seafloor}$,

including sediment composition such as roughness may add additional error, but the effects have not been well quantified.

ALB Sources of Uncertainty		
Measurement Component	Vertical Uncertainty	Horizontal Uncertainty
Aerial		
σ_{ALB}	2cm	20cm
σ_{GPS}	2cm	5cm
Atmospheric		
σ_{atm}	~0cm	~0cm
Water Surface		
$\sigma_{windwaves}$	1-2% of depth	5-10% of depth
Water Column		
$\sigma_{scattering}$	Assumed to be 0 cm	Assumed to be 0cm
$\sigma_{stretch}$	0.05-1m	~0cm
Seafloor		
$\sigma_{seafloor}$	Dependent on detection algorithm, slope, and composition	

Table 6.1: Uncertainty values for ALB systems reported as 2σ standard deviations.

Previous studies have shown that surface waves of wavelength less than 0.1 m will be fully developed with fetches over 30 m (Zhang, 1995), where wind speed is the dominant parameter effecting the generation of these waves. In the vast majority of ALB surveys, weather conditions will include wind blowing over a fetch of 30 m or greater. Therefore, it is most relevant to consider wind speed as the primary environmental parameter that should be measured to estimate the error due to small wind ripples. Additionally, the results of this study indicate that wind direction has an impact on the wave refraction error. Results of the study show that there is more uncertainty of the refraction angle in the direction parallel to the wind (along-wind) than in the orthogonal direction (cross-wind).

6.2 Future Work

While this study provided a method to evaluate uncertainty caused by small wavelets on the water surface, further efforts are needed in order to produce a more robust ALB water surface uncertainty model that includes the effects of the aircraft, atmosphere, water column and seafloor. With additional time and resources new data sets could be collected to expand upon the findings presented here. Ray trace models and empirical validation of the other environmental factors would allow for comprehensive TPU reporting of ALB depth measurements.

One limitation of this study was the small number of photodiodes used in the detector array. Eren et al. (2016) explained that utilizing a greater number of detectors in the optical detector array allows for greater resolution of data and more accurate images analysis results. Performing similar experiments to the ones performed here with an array containing more optical elements (10X10 or 20X20 array elements) would allow for more precise analysis of the beam footprint. Beam shape distributions or even beam splitting due to surface waves could be characterized.

Additional calibration of the detector array will increase the amount of data that could be extracted from the beam footprint images. Currently, the refraction angle was calibrated only along one axis of the array. Calibrations similar to the one conducted in this study could be performed on additional parameters including cross-wind refraction angles, along-wind and cross-wind horizontal shifts of the beam, and beam-shape calibrations. The beam footprint characteristics could be directly measured using the image moment invariant technique.

The relationship between beam spot diameter on the surface and uncertainty should also be empirically quantified. Utilizing detector arrays of larger size would allow beam footprints of varying size to be imaged. Empirical data showing that the wave refraction error is lower for larger

beam footprints would further confirm the computer models. Similarly, the assumption that larger beams have an averaging effect on the refraction error from small waves should also be confirmed.

As this study only assessed the effects of short surface ripples (L<0.1m), more empirical data could collected with waves in the gravity regime. Waves of this size will introduce additional refraction error in to the ALB measurements. Considering sea state conditions with few wave crests present in the laser beam footprint could lead to new correction methods or additional uncertainty reporting.

7. CONCLUSIONS

In this study, the contribution of the water surface on ALB measurement uncertainty was assessed and quantified. A procedure for calculating the ALB uncertainty due to wave surface conditions was developed (i.e., measurement and reporting methods). The procedure included: 1) a numerical model using Monte Carlo ray-trace simulations, and 2) an empirical validation approach using an optical detector array for observing the refracted laser beam underwater. The goal of this study was to quantify the contribution of the water surface conditions on the ALB range measurements. The primary objectives of this study were: producing a device to measure a laser beam footprint below the water surface, measuring the effects of wind driven capillary and gravity-capillary waves on ALB uncertainty through empirical and analytical analysis, and calculating the ALB range uncertainty caused by surface wave refraction.

Three-dimensional water surface realizations were numerically modeled after realistic water surfaces (using Mobley's (2004) approach and Apel's (1994) wave spectrum function). Ray tracing was performed through the simulated water surfaces using a Monte-Carlo approach in order to calculate the path of the laser beam footprint below the water surface. Using the still water location of the beam footprint as a control, the wave refraction error was statistically quantified. The computer simulations identified key parameters that altered the wave refraction error and were confirmed in a laboratory environment.

The results of the computer analysis were then validated empirically by imaging a laser beam footprint that had refracted through real, wind-generated water surface conditions. An underwater optical detector array was designed and built to image the laser beam footprint after refraction

through the water surface. The empirical experiments were conducted under well-controlled conditions in the University of New Hampshire's Wave and Tow Tank facilities. Sea states produced in the wave tank accurately represent real-world water surface conditions for small waves in the capillary and gravity-capillary wave regime. Various sea states and laser geometric parameters (such as beam diameter at the surface, and in air incidence angle) were explored over a range of values that would be seen in a real world ALB survey. Beam footprints refracted through the wind-driven water surface were observed using an optical detector array underwater. Images of the refracted laser beam were compared to a control beam footprint observed in still water conditions. The wave refraction error was quantified with respect to key environmental and system parameters including: the off nadir angle of the beam, the beam diameter at the water surface, and the wind speed and direction.

The wave refraction error was then tabulated with respect to the key environmental and system parameters. This data provides an uncertainty 'look-up' table that can be used to improve TPU reporting for ALB surveys. Provided the survey technician records wind speed and direction, along with incidence angle and beam diameter provided by the ALB unit, the wave refraction error due to wind ripples may be reported in real time for each pulse.

The findings of this study support previous analytical studies (Tulldahl and Steinvall, 2004; Karlsson, 2011) that considered the error caused by the still water approximation. The study also provides a method to conduct laser beam footprint diagnostics that could be used to experimentally examine other ALB environmental errors including, the effects of water column scattering and absorption, and seafloor characteristics.

REFERENCES

Airy, G. (1894). *Tides and Waves.* London: J.J. Griffin.

Anis Bouhdaoui, J.-S. B. (2014). Modeling the Water Bottom Geometry Effect on Peak Time Shifting in LiDAR Bathymetric Waveforms. *IEEE Geoscience and Remote Sensing Letters*, 1285-1289.

Apel, J. (1994). An improved model of the ocean surface wave vector spectrum and its effects on radar backscatter. *Journal of Geophysical Research*, 16269-16291.

Bretschneider, C. (1964). Generation of Waves by Wind State of the Art. *Office of Naval Research*.

Britannica, E. o. (2009). Beaufort Scale. In *Encyclopedia Britannica.* Encyclopedia Britannica.

Bunkin, A., & Voliak, K. (2001). *Laser Remote Sensing.* John Wiley and Sons.

Coastal Engineering Manual. (2017). USACE.

Collin, A., Long, B., & Archambault, P. (2011). Benthic classifications using bathymetric LIDAR. *Journal of Coastal Research*, 86-98.

Cox, C., & Monk, W. (1956). Measurment of the Roughness of the Sea Surface Deduced from Photographs of Sun's Glitter. *Journal of the Optical Society of America*.

Cox, J. (1998). *Fundamentals of Linear Electronics: Integrated and Discrete.* Albany : Delmar.

Dean, R., & Dalrymple, R. (1984). *Water Wave Mechanics for Engineers and Scientists.* Englewood Cliffs, NJ: Prentice-Hall.

Demirbilek, Z., & Linwood, C. (2002). *Coastal Engineering Manual.* Washington D.C.: U.S. Army Corps of Engineers.

Elfouhaily, T., Chapron, B., Katsaros, K., & Vandemark, D. (1997). A unified direction spectrum for long and short wind driven waves. *Journal of Geophysical Research*, 148-227.

Eren, F., Pe'eri, S., Rzhanov, Y., Thein, M.-W., & Celikkol, B. (2016). Optical Detector Array Design for Navigational Feedback Between Unmanned Underwater Vehicals (UUVs). *IEEE Journal of Oceanic Engineering*.

Exton, R., Houghton, W., Esaias, W., Harriss, R., Farmer, F., & White, H. (1983a). Laboratory analysis of techniques for remote sensing of estuarine parameters using laser excitation. *Applied Optics*, 54-64.

Guenther, G. (1985). *Airborne Laser Hydrography : System Design and Performance Factors.* Rockville, MD: NOAA Professional Paper Series.

Guenther, G., LaRocque, P., & LillyCrop, W. (1994). Multiple Surface Channels in SHOALS Airborne Lidar. *SPIE: Ocean Optics*, 422-430.

Hasselmann, K., Barnett, Bouws, Carlson, Cartwright, Enke, . . . Walden. (1973). Measurments of Wind-Wave Growth and Swell Decay During the Join North Sea Wave Project (JONSWAP). *Ergnzungsheft zur Deutschen Hydrographischen Zeitsschrift Reihe*, 95.

IHO Standards for Hydrographic Surveys- Special Publication No. 44. (2008). International Hydrographic Bureau.

Karlsson, T. (2011). *Uncertianties Introduced by the Ocean Surface when Conducting Airborne Lidar Bathymetry Surveys.* Durham, NH: Univeristy of New Hampshire.

Ke-cheng, Y., Yi, L., Xiao, Z., & Zai-guang, L. (2002). Reflection and refraction of gaussian laser beam on wavey surface in airborne ocean lidar. *Wuhan University Journal of Natural Science*, 207-211.

Krogstad, H. (2000). *Linear Wave Theory (Part B).* Trondheim, Norway: Norwegian University of Science and Technology.

Kumar, V., Pathak, K., Pednekar, P., Raju, N., & Gowthaman, R. (2006). Coastal Processes Along the Indian Coastline. *Current Science*, 25.

Lighthill, M. (1978). *Waves in Fluids.* Cambridge, MA: Cambridge University Press.

May, N., & Toth, C. (2007). Point positioning accuracy of airborne lidar systems: a rigorous analysis. *International Archives of Photogrammetry, Remote Sensing and Spatial Information Sciences*, 107-111.

Measures, R. (1984). *Laser remote sensing: fundamentals and applications* . Malabar, FL: Krieger Publishing Company .

Mitsuyasu, H., Tasia, F., Suhara, T., Mizuno, S., Ohkusu, M., Honda, T., & Rikishi, K. (1974). Observations of the directional spectrum of ocean waves using a cloverleaf bour. *Journal of Physical Oceanography*, 750-760.

Mobley, C. D. (1994). *Light and Water: Radiative Transfer in Natural Waters.* San Diego, CA: San Diego Academic Press.

Mobley, C. D. (2014). *Modeling sea surfaces.* Seattle, WA: Sequoia Sceintific Inc.

Moskowitz, L. I., & Pierson, W. J. (1962). *Wave Spectra Estimated from Wave Records Obtained by the OWS Weather Explorer and the OWS Weather Reporter.*

Pe'eri, S., Mcleod, A., Lavoie, P., Ackerman, S., Gardner, J., & Parrish, C. (2013). Field calibration and validation of remote-sensing surveys. *International Journal of Remote Sensing*, 6423-6436.

Penny, M., Abbot, R., Phillips, B., Billard, B., Rees, D., Faulkner, D., . . . Richards, J. (1986). Airborne Laser Hydrography in Australia . *Applied Optics 25(13)*, 2046-2058.

Preisendorfer, R. W., & Mobley, C. D. (1985). *Unpolarized Irradiance Reflectances and Glitter Patterns of Random Capillary Waves on Lakes and Seas by Monte Carlo Simulation.* Seattle, WA: Pacific Maritime Envrionmental Lab.

Preisendorfer, R. W., & Mobley, C. D. (1986). Albedos and Glitter Patterns of a Wind-Roughened Sea Surface. *Journal of Physical Oceanography* .

Preisendorfer, R. W., & Mobley, C. D. (1988). *A Numerical Model for the Computation of Radiance Distributions in Natural Water with Wind-roughened Surfaces.* Seattle, WA: Pacific Maritime Environmental Lab.

Quadros. (2013). Unlocking the characteristics of bathymetric lidar sensors. *Lidar Magazine*.

Quadros, N. (2013). *Unlocking the characteristics of bathymetric lidar sensors* . LIDAR Magazine.

Rzhanov, Y., Eren, F., Pe'eri, S., & Thein, M.-W. (2014). An Image Processing Approach for Determining of Relative Pose of Unmanned Underwater Vehicles. *Oceans'14 MTS/IEEE*. Tiapei Tiwan.

Steinvall, O., Koppari, K., & Karlsson, U. (1994). *Airborne Laser Depth Sounding: System Aspects and Performance.*

Thomas, R., & Guenther, G. (1984). *Prediction and correction of propagation-induced depth measurment biases plus signal attenuation and beam spreading for airborne laser hydrography.* Rockville, MD: NOAA Technical Report.

Tulldahl, M., & Steinvall, O. (2004). Simulation of Water Surface Wave Influence on Small Target Detection with Airborne Laser Depth Sounding. *Applied Optics*.

Wang, C., & Philpot, W. D. (2007). Using Airborne Bathymetric Lidar to Detect Bottom Type Variation in Shallow Waters. *Remote Sensing of Environment, 106*, 123-135.

APPENDIX

A. Wave Spectrum Models

JONSWAP Spectrum (Used for Apel calculations)

The JONSWAP spectrum may be calculated as follows:

$$S(f) = \frac{\alpha g^2}{\omega^5} \exp\left[-\frac{5}{4}\left(\frac{f_p}{f/2\pi}\right)^4\right]\gamma^{\sigma} \qquad \text{(A.1).}$$

With the constants found using the relations based on wind speed and fetch:

$$f_p = 2 * \pi * 2.84\, g^{0.7} F^{-0.3} U_{10}^{-0.4} \qquad \text{(A.2),}$$

$$\alpha = 0.076\left(\frac{U_{10}^2}{F*g}\right)^{0.22} \qquad \text{(A.3),}$$

$$\gamma = 3.3, \;\; \sigma = \begin{cases} 0.07 & f \le f_p \\ 0.09 & f > f_p \end{cases} \qquad \text{(A.4).}$$

Apel spectrum (1994)

The basic Apel equation is as follows:

$$S(f) = A f^{-3} L_{pm} J_p s R_{res} V_{dis} I_d \qquad \text{(A.5).}$$

Where *f* is the frequency, *s* is the spreading parameter (typically 2-3 for short fetch). The values A, L_{pm}, J_p, R_{res}, V_{dis}, and I_d can be identified in the *Apel (1994)* paper.

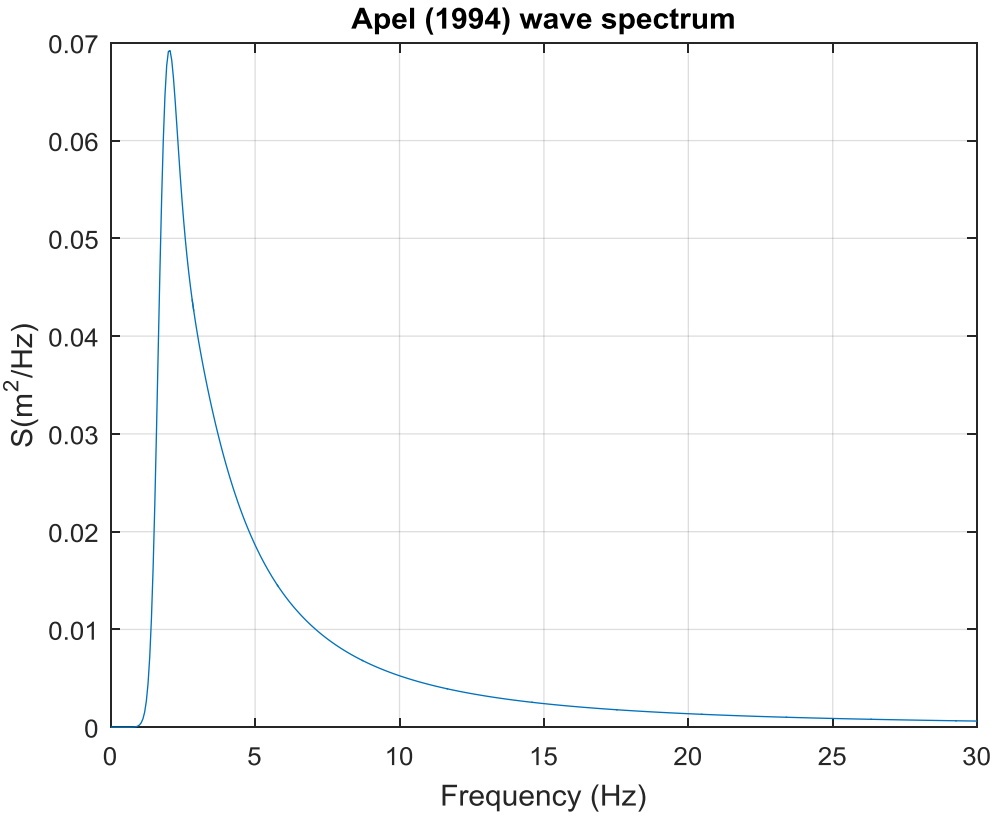

Figure A.1: Example Apel spectrum for fetch =30 m and U=5 m/s.

B. Optical Detector Array

A description of the components and construction of the optical detector array.

Photodiodes

Photodiodes consist of a semiconductor that converts incoming photons into electrical current. The amount of current generated is proportional to the intensity of the incident light, and can be measured by monitoring the voltage drop over a load placed on the photodiode. The diodes sensitivity to light is known as the responsivity (A/W) and allows the power of the light to be measured. There are many kinds of photodiodes including simple PIN photodiodes, avalanche photodiodes, photomultiplier tubes, and Geiger mode detectors.

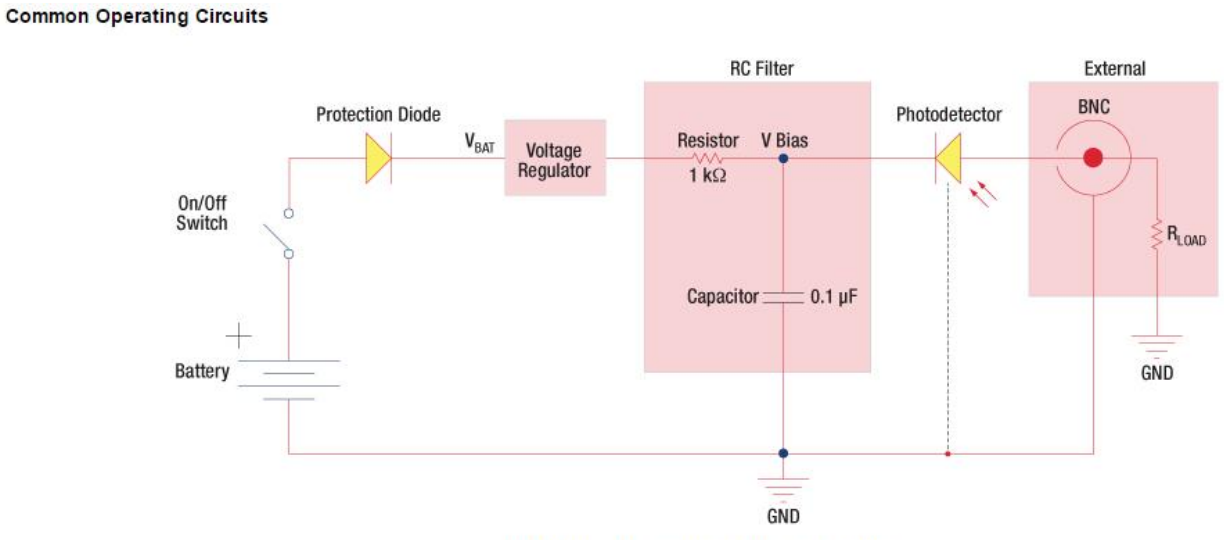

Figure B.1: The reverse bias circuit to be used with photodiodes as provided by ThorLabs.

PIN photodiodes essentially act as light sensitive resistors that have an inverse relationship between light and resistance. Photodiodes are produced with varying materials depending on the electromagnetic spectrum that is to be measured. Silicone (200-1100nm), germanium (800-

1600nm) and indium gallium arsenide (900-1700nm) are common types of diodes. Photodiodes are designed to be operated in reverse bias (Figure B.1: the anode of the diode is supplied with a positive voltage) to increase response time (Cox 1998).

Avalanche photodiodes (APD's) are commonly used in commercially ALB systems and they apply a very large reverse bias of 50 to 300 volts to a PIN photodiode. This large bias produces an internal gain of the signal and allows the APD to detect much lower levels of light than a typical PIN detector. Due to the high gain internal noise is also amplified and signal filtering is necessary to achieve useful results.

Similar to APD's, new Geiger mode detectors have recently been developed. According to *Dautet et. al* these photodiodes are reverse biased to values higher than the breakdown voltage producing gains of 10^5 or 10^6 when triggered. In this mode even a single photon can cause the avalanche voltage response leading to the ability to perform single photon counting. Noise and amplified bulk dark current are very problematic when working with Geiger mode detectors making them difficult to use. Although these detectors are only used on experimental systems (e.g., HRQLS), the large amount of background noise disqualifies them from being used in operational systems.

Photon multiplier tubes (PMT) are another type of photodetector used in commercial ALB systems. PMT implement current amplification to improve signal output. PMT's utilize a semiconductor placed in a vacuum tube to generate electrons from incident light. Then a method of electron multiplying with the use of dynodes is implemented to increase the output current by up to 108 times according to Hamamatsu (2007). PMT's are very effective for low light applications with relatively low levels of signal noise. Due to the vacuum vessel a PMT is much larger than most PIN based detectors.

For the application of laser beam diagnostics in the water column an extremely sensitive photodiode is not required, as much of the light will not be scattered or attenuated on its path to the sensor. The photodiodes must also be sturdy enough to use underwater or in a waterproof housing. For these reasons a PIN type photodiode was chosen due to a low price point and simple durable construction. The ThorLabs PD1A silicone photodiode (Figure B.2) was selected for use in the laser diagnostics array. It's low cost (~$70), sensitivity, and its peak responsivity in the visible light spectrum (ideal for a 532nm laser application) were the leading factors for using these detectors in this study.

Figure B.2: ThorLabs PD1A Photodiode (www.thorlabs.com)

Waterproof Housing

To allow the sensor array to operate underwater, waterproof housings were constructed from clear acrylic plastic (Figure B.3) at the Joint Hydrographic Center's machine shop. A hole was taped into a cylinder of acrylic plastic and a small window was glued to the front of the cylinder. Watertight cord grips were then mounted to the rear to allow the SMA adaptor cables to pass out of the housing. Finally a Delrin collar was fixed to the acrylic housing to allow the element to be mounted to the grid.

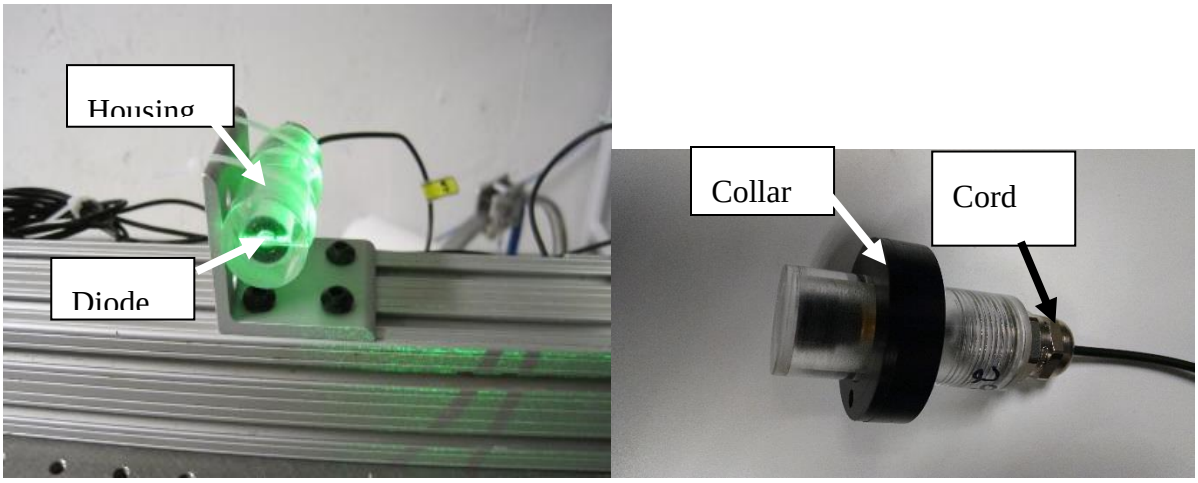

Figure B.3: Waterproof housing for photodiode

Mounting Grid

A Delrin plate (24”X18”) was used to configure all of the photodiode elements in the desired configuration (Figure B.4: Mounting Grid). The array was designed with a square 25 cm X25 cm grid incorporating a total of 36 photodiodes. Each diode is spaced 5 cm along the x and y axis. A screw tapped through each collar on the waterproof housing secures the photodiodes and housings to the Delrin plate. One of the advantages using this frame design is its modularity to change the detector array from 2X2 elements up to 6x6 elements or alternative configurations.

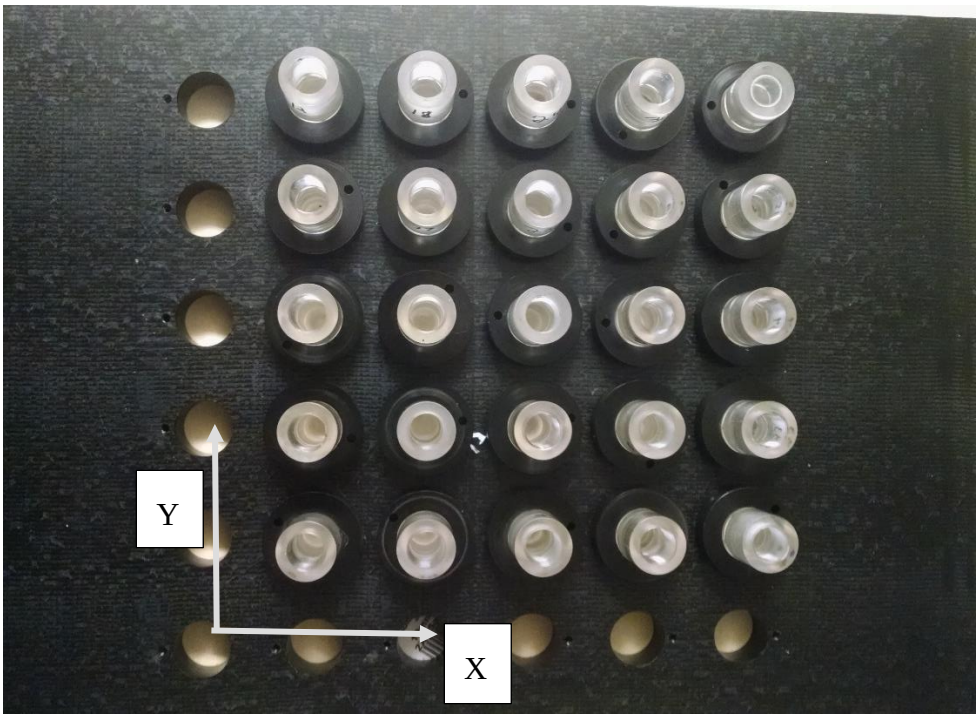

Figure B.4: Mounting Grid

The Delrin plate was secured to an 80X20 structure (Figure B.5) that allows the array to be suspended in the UNH Chase Ocean Engineering wave and tow tank

Figure B.5: Array mounted to frame

C. Photodiode Calibration

Responsivity

To measure the current produced by a photodiode, a resistor is typically placed in the circuit and the voltage across the resistor is measured. This voltage value can only be used to compare relative intensity unless the responsivity of the photodiode is calculated. In this case the responsivity is the relationship between the incoming light power (Watts) and the voltage measured by the system (Volts) and is expressed as Volts per Watt (V/W). This can be simply measuring the voltage output for a number of known light power inputs. A 1 MΩ resistor was incorporated in the reverse bias circuit in order to measure voltage. Based on Kirchoff's laws V=IR and a responsivity provide by the manufacturer of 0.3 A/W, an output of 0.3MV/W is expected to be produced.

First, a Ophir PD300 laser power measurement sensor was used to measure and characterize the variable output of a ND:YAG tunable Minilite 532 nm pulsed laser. The power output of the tunable laser can be varied and each of the laser's power settings was characterized using measurements containing more than 60 pulses. The average power as a function of the dial setting is presented in Figure C..

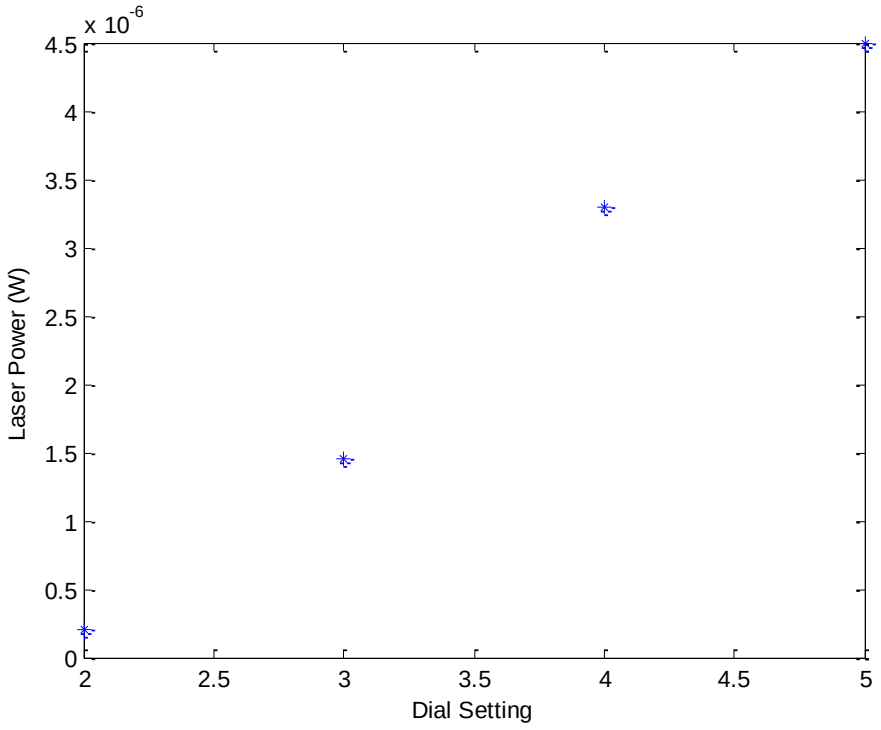

Figure C.1: ND:YAG laser power vs. dial setting

The photodiode was then used to measure the laser at the same dial settings and the voltage output was recorded using a Tectronix Oscilloscope. The output voltage of photodiode measured using a 5 V reverse bias circuit and a 1 MΩ resistor (Figure C.2). The responsivity was found to be 0.27 MV/W. The experimentally calculated diode response fits closely to the expected value of 0.3 MV/W with an error of 10%.

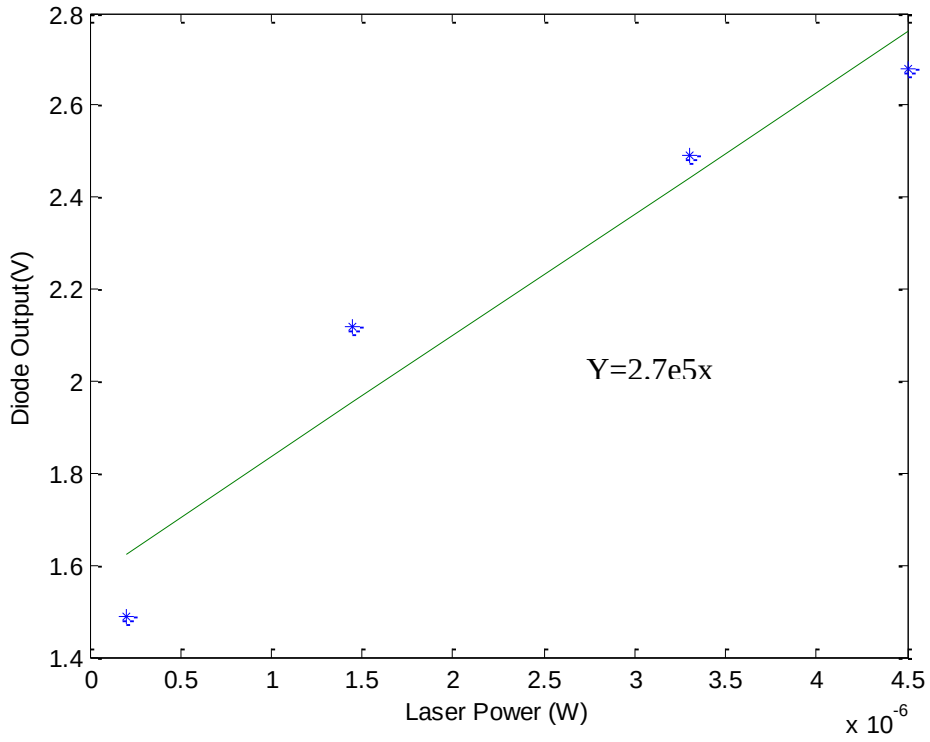

Figure C.2: Photodiode output vs. laser power

Temperature Sensitivity

The responsivity curve for this silicone diode is valid only for a specific temperature, 20 ˚C. For standard room temperature and pressure conditions (i.e., 20 ˚C, 101.3kPa), the photodiode's responsivity was found to be 0.27 A/W. As the temperature of the photodiode varies, the responsivity will change (i.e., Quantum Efficiency). The main reason is because of the optical properties of silicone change with temperature and pressure for any specific wavelength (λ). Typically, blue and green wavelengths responsivity decreases with increasing temperature, while red and yellow wavelengths are the opposite.

This change in responsivity is proportional to the change in percentage of the ability of the photodiode to convert the total incident light into current, also known as quantum efficiency. The following equation gives the relationship for quantum efficiency

$$\%QE = \frac{\#\ photons\ converted}{\#total\ photons} \qquad \text{(C.1)}$$

For the PD1A photodiode the quantum efficiency is stated to be 75%. The quantum efficiency can also be calculated from the responsivity at a specific wavelength as shown:

$$\%QE = \frac{1.24\times10^5\times\Re_\lambda}{\lambda} \Rightarrow \Delta\Re_\lambda = \frac{\lambda*\Delta QE}{1.24\times10^5} \qquad \text{(C.2)}$$

For a typical silicon diode as used in the Thorlabs PD1A the temperature dependence of the quantum efficiency (i.e., change per degree Celsius) is a function of the wavelength. Figure C.3 shows this relationship, where the quantum efficiency is assumed to be 75% at room temperature. From this plot it can be found that for laser light at 532 nm the quantum efficiency would change by 0.08% per degree. Using equation C.2, the corresponding change in responsivity per degree Celsius is 0.0256(A/W). Using equation 1 with a resistance of 50 Ω and value of 4 mW for the laser power (the power of the laser pointer to be used), the theoretical change in voltage output per degree Celsius is -5 mV.

The goal of the experiment is to measure the change in voltage output of the PD1A photo detector from temperatures ranging from 20 ˚C (Standard Ocean Water in Portsmouth Harbor) to 70 ˚C. This temperature range is large enough to develop a functional curve of the dependence of voltage output to temperature. The range of ocean water is typically between 15 ˚C to 30 ˚C. The temperature dependence of the photodetector can be then used to establish a voltage correction equation that can be used to calculate the actual incoming power.

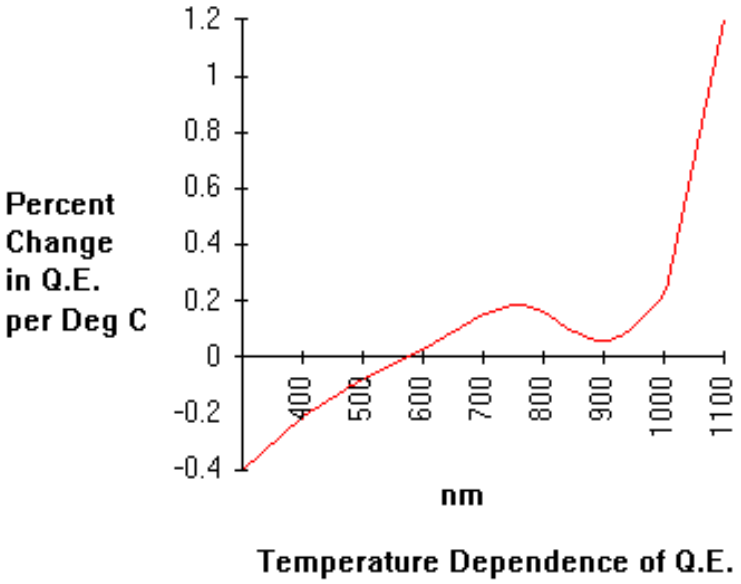

Figure C.3: Temperature effect on QE vs Wavelength (3. Quantum Efficiency)

Thermal Time Constant

The thermal time constant was experimentally calculated in order to determine how long the photodiode and housing required to reach a specific temperature,. A k-type thermocouple was used to measure the temperature of the silicone diode. The system was allowed to come to steady state before then being dropped into 70 degree water. The voltage output of the thermocouple was recorded over time and was then converted to temperature. The thermal time constant was calculated to be 39 seconds, as shown in Figure C.4.

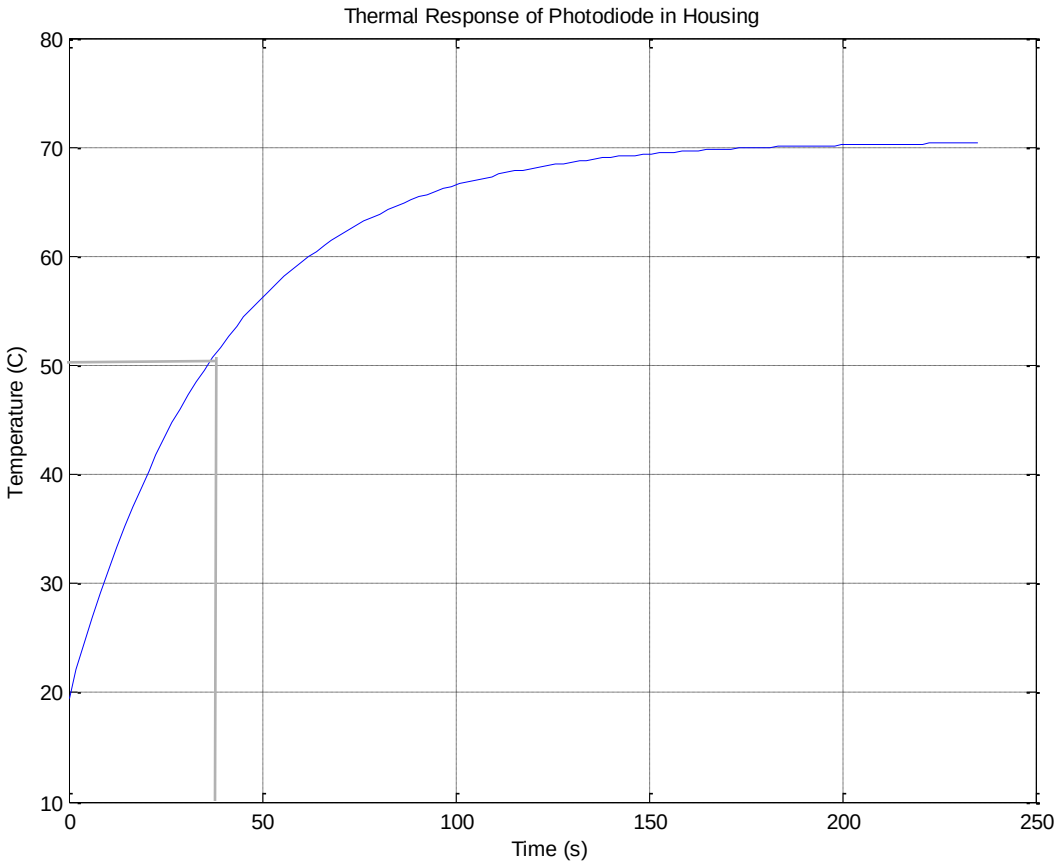

Figure C.4: Thermal Time Constant for Housing.

Time Constant	Time to Reach Steady State(4*T)	Mass of system	Sensitivity of Thermocouple
39 seconds	156 seconds	184 grams	10 mv/deg C

Thermal Temperature Dependence

Data was collected from the photodiode at range of temperatures from 20 to 70 ˚C. For each measurement, the system was allowed to come to equilibrium determined by the thermal time constant. A constant 532 nm laser power was incident on the photodiode. Figure C.5 shows the data with the best-fit line, it was noted that at the 70 ˚C measurement there was a build-up of steam in the water bath that significantly affected the amount of light reaching the photodiode. For this reason, this data point was ignored when calculating the best fit line. It was found that the spectral sensitivity to temperature was -2 mV/˚C. The equation for the fit line is a follows in mV.

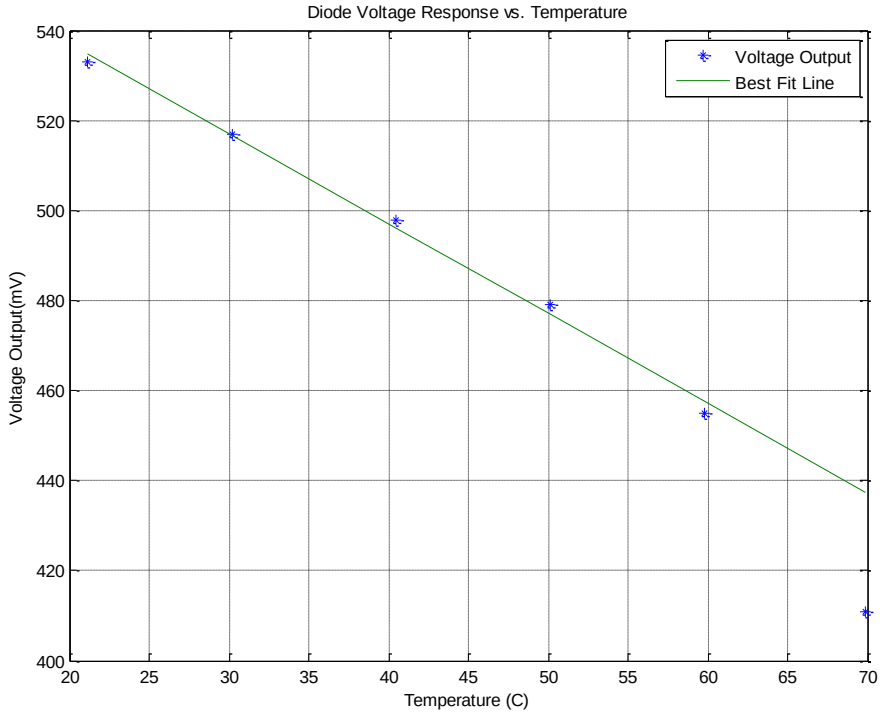

Figure C.5: Thermal Dependence

$$Vo(T) = -2 * T + 576 \qquad \text{(C.3)}$$

	Voltage dependence (mV/°C)	Responsivity Dependence (A/(W*°C))	% Error
Analytical	-5	.02	60%
Measured	-2	.01	

Using this data and the fit line, data at any temperature can be corrected back to standard room temperature and pressure. The equation used to make this correction is as follows:

$$V_{corrected}\,(T) = Vo(T) + (Vo(20) - Vo(T)) \qquad \text{(C.4)},$$

Where, Voltage (mV) and Temperature (Celsius).

With this equation the voltage output is corrected for temperature, and using the calculated sensitivity of 0.27A/W the incident power on the photodiode can be calculated.

The actual incoming power from a 532 nm laser on a PD1A photodiode can be calculated at standard room temperature and pressure using a sensitivity of 13.5 V/W, as well as a dynamic range of temperatures from 20 ˚C to 70 ˚C by correcting output voltage of the PD1A photodiode using Equation C.4. The study experiments show that an increase in incoming power at 532 nm the voltage output of the diode will increase proportionally at 16 V/W. The actual sensitivity measured was 13.5 V/W. The error between analytical and measured is reasonable because each individual PD1A photodiode will have a slightly different sensitivity. If the waterproof housing is allowed to sit in the water bath for 3 minutes, the outside temperature of the water is the same as the temperature of the photodiode. It was found that analytically the temperature dependence of a silicon photodiode is -5 mV/ °C The actual measured temperature dependence of the PD1A

photodiode was -2 mV/ °C. The error between analytical and measured is reasonable because the analytical data was taken from a silicon photodiode curve, independent of the PD1A. From the temperature dependence values a voltage correction equation was developed to correct in real time to be able to quantify the actual incoming laser power.

Field of View

In this study, the geometric overlap between neighboring photodetector were taken into account in order to limit any erroneous measurements related to the field of view of the photodiodes used, such that optical cross-talk between sensors. In an array of photodiodes, there is some critical distance at which area of coverage of neighboring photodiodes will begin to overlap (Figure C.6).

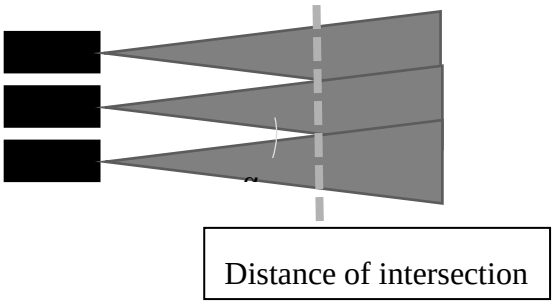

Figure C.6: Example of FOV crosstalk.

The field of view α, is effected by the size of the silicone diode patch (d), as well as the geometry of the housing it is mounted in. To calculate the field of view of the ThorLabs PD1A photodiode, the following experiment was conducted on the CCOM optical lab bench. An Apinex 532nm laser pointer was mounted 1m away (on the along x axis) from the photodiode. The laser pointer was then translated along the Y axis in 5 cm increments and its aim adjusted to point directly at the

diode. At the distance when the visual contact between the laser beam and the photodiode was broken the maximum field of view was calculated. It was assumed that visual contact was broken when the voltage output from the diode dropped significantly

Distance (y-axis m)	0	0.05	0.1	0.15	0.2	0.25	0.3	0.35	0.4
Voltage Output (mV)	150	150	150	150	150	150	150	90	35

Table C.2: Field of View Results

Table C.2 provides the results from the experiment. The angle between the diode can be found with the arctangent of the y value divided by the x value. The visual contact dropped after 0.3 m indicating that $\alpha/2$ is 16°. It was found that the field of view of a PD1A diode is 32°. Each photodiode is spaced 0.05 m apart in the two directions. To avoid optical crosstalk between sensors the photodiode array should be mounted 8 cm below the water surface.

D. Image Processing Techniques

Image Moment Invariants

Images moment invariant is an image processing technique that reveal information about symmetry and geometrics of the footprint image produced by the detector array. The moments of images (i.e., relationship between the neighboring image pixels) can be used to calibrate the array for measurements, such as center of concentration, angle of incidence, or beam diameter. The

moment calculation uses the second derivative of intensity of neighboring pixels to provide sub pixel accuracy within the image. A 3x3 moment matrix of the 9 total image moments was constructed using the following equation:

$$M_{p,q} = \frac{1}{S}\sum_{i,j}(x_i - x_0)^p\left(y_j - y_0\right)^q I_{i,j} \qquad S = \sum_{i,j} I_{i,j} \quad , \qquad \text{(D.1)}$$

Where $M_{p,q}$ (p and q are integers from 1 to 3) is the moment invariant along the 3x3 matrix, x_0 and y_0 are the centroid components, and I is the pixel intensity, and i and j are the number of pixels in the x and y directions of the image (6 in both cases). From equation D.1, the moment matrix of an image can be constructed, then ratios of the given matrix elements can be calculated to find correlation to changing image parameters (Rzhanov, 2014). For each frame collected the image moment matrix was calculated. The individual moment values were compared to changing physical parameters in an attempt to find correlation. Additionally ratios of the different moment values were compared with the physical parameters to see if stronger correlations exist.

M_{11}	M_{12}	M_{13}
M_{21}	M_{22}	M_{23}
M_{31}	M_{32}	M_{33}

Centroid Analysis

The centroid analysis is an image processing method that finds the relative center location of point measurement concentration, this calculation is similar to center of mass calculations. This technique is used to see how the center of concentration of the beam may shift horizontally due to ripples on the water surface focusing the beam. The center of concentration was found along both the rows and columns of the array to find the center of the 2D image. The image moment values

(see Appendix D.1) are used in the calculation of the centroid of the image using the following equation:

$$\{\bar{x}, \bar{y}\} = \left\{\frac{M_{12}}{M_{11}}, \frac{M_{21}}{M_{11}}\right\}. \quad \text{(D.2)}$$

E. Additional Centroid Analysis Datasets

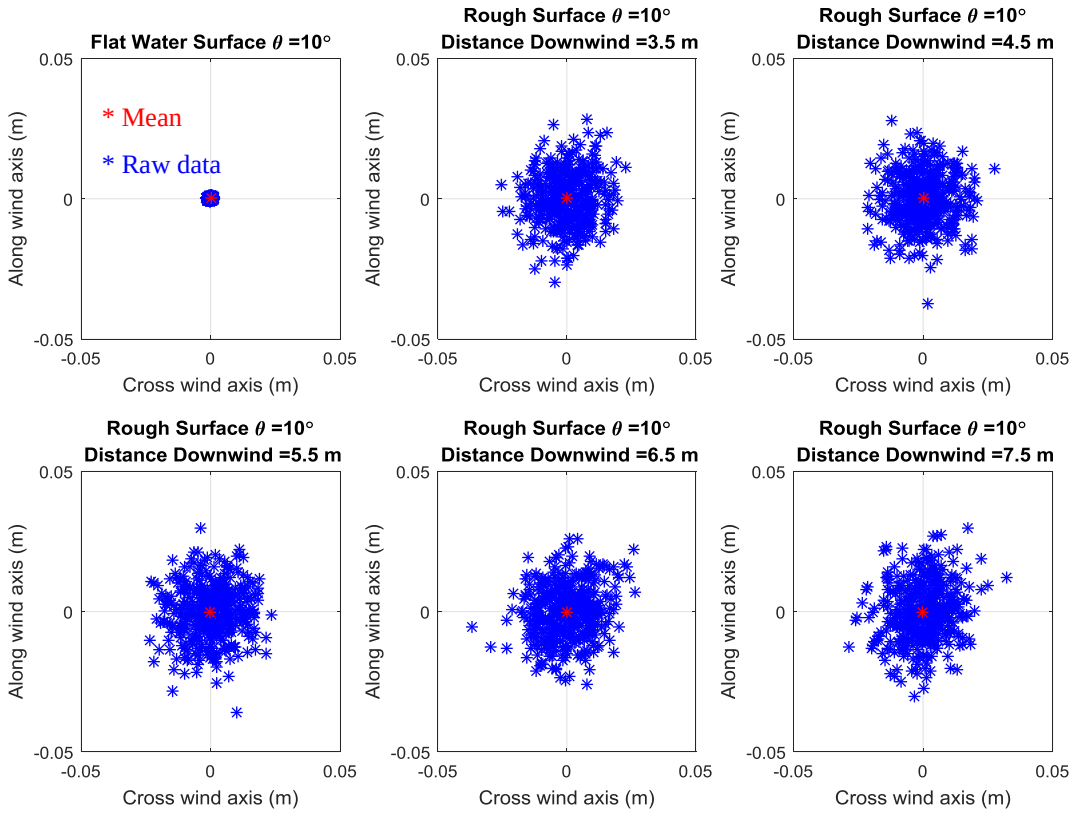

Figure E.1: The centroid results at distances of 3.5 to 7.5 m from the fan at an incidence angle of 10°.

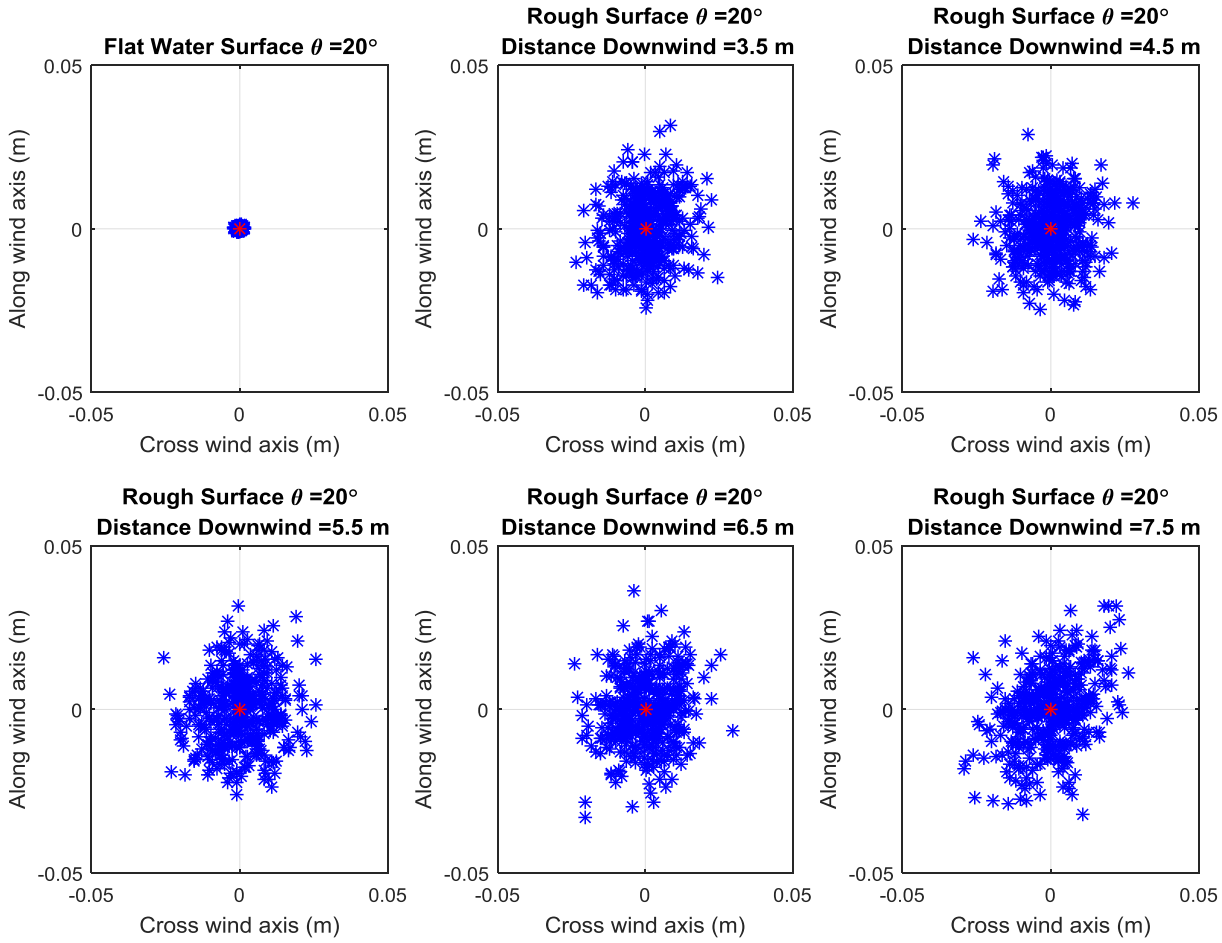

Figure E.2: The centroid results at distances of 3.5 to 7.5 m from the fan at an incidence angle of 20°.